Western University
Scholarship@Western

Digitized Theses | Digitized Special Collections

2009

# Fluxes of Sporadic Meteoroids from Optical Measurements

David G. Braid

Follow this and additional works at: https://ir.lib.uwo.ca/digitizedtheses

Recommended Citation
Braid, David G., "Fluxes of Sporadic Meteoroids from Optical Measurements" (2009). *Digitized Theses*. 4049.
https://ir.lib.uwo.ca/digitizedtheses/4049

This Thesis is brought to you for free and open access by the Digitized Special Collections at Scholarship@Western. It has been accepted for inclusion in Digitized Theses by an authorized administrator of Scholarship@Western. For more information, please contact wlswadmin@uwo.ca.

# Fluxes of Sporadic Meteoroids from Optical Measurements

(Thesis Format: Monograph)

By

David G. Braid

Graduate Program in Physics

A thesis submitted in partial fulfillment
of the requirements for the degree of
Master of Science

The School of Graduate and Postdoctoral Studies
The University of Western Ontario
London, Ontario, Canada

© David G. Braid 2009

## Abstract

The purpose of this study was to develop a process to measure the mass distribution index, the speed distribution, and the flux of the sporadic meteor sources using an electro-optical system. Data was recorded on two nights, April 27 and May 6, 2006, and the system was tested by measuring the flux of the eta Aquariid meteor shower. Eta Aquariid fluxes yielded ZHRs of 14.3 ± 4.5 meteors $hr^{-1}$ and 65 ± 10 meteors $hr^{-1}$ on the measured nights in agreement with literature values (Rendtel, 1997). The mass index of sporadic meteors was $s$ = 2.14 ± 0.12 and the speed distributions were found to be in agreement with radar measurements by Campbell-Brown (2008). The estimated total annual flux from all sporadic sources was: 0.226 ± 0.018 meteors $km^{-2}hr^{-1}$ and 0.151 ± 0.023 meteors $km^{-2}hr^{-1}$ brighter than magnitude 4.72 ± 0.19 for April 27 and May 6 respectively.



**Keywords:** meteor, meteoroid, meteor flux, zhr, zenithal hourly rate, sporadic meteors, sporadic sources

## Acknowledgements

I would like to extend my deepest gratitude to Dr. Margaret Campbell-Brown and Dr Paul Wiegert for all their guidance, advice, and support throughout the research. Their patience, flexibility, and expertise helped to make the project goals attainable. I would also like to thank my advisory committee and my examining committee for all their suggestions and refinements to the final document.

Thanks are also due to my colleagues Jean-Baptiste Kikwaya and Shannon Nudds for their help with data collection and reduction, and Dr. Peter Brown, Robert Weryk, and Dr. Wayne Edwards for all their insights and clarifications.

The financial support provided by the University of Western Ontario is greatly appreciated.

Finally I would like to thank my friends and family for their continued support throughout my time at the University of Western Ontario. Special thanks to Robyn Lotter and David Chochol for their time and diligence in revising and clarifying my thesis, and to my parents Mary Jane and Gordon Braid.

# Contents

# List of tables

# List of figures

## List of Appendices

## List of Abbreviations

AMOR ..... advanced meteor orbit radar

AH ..... antihelion

CCD ..... charge coupled device

CMOR ..... Canadian meteor orbit radar

H ..... helion

HPLA ..... high power low aperture

HRMP ..... Harvard meteor radar project

NA ..... north apex

NT ..... north toroidal

PNG ..... portable network graphics

SA ..... south apex

ST ..... south toroidal

TIFF ..... tagged image file format

ZHR ..... zenithal hourly rate

# 1. Introduction

## 1.1 Meteor Definitions

The meteor phenomenon, commonly called a "shooting star", is something observed by most people at some point in their lives. The names of the body at each stage of collision with the Earth are often confused. Meteoroids, meteors, and meteorites are terms representing the three major stages of the meteor phenomenon.

A meteoroid is an object travelling in space which is larger than a dust grain, but smaller than an asteroid. Meteoroids may collide with the Earth's atmosphere within a restricted velocity ranging from 11.2 km $s^{-1}$, which corresponds to a meteoroid with zero geocentric velocity, to 72.8 km $s^{-1}$, corresponding to the heliocentric escape velocity at 1 AU plus the Earth's mean heliocentric velocity (Ceplecha & Borovička & Elford & Revelle & Hawkes, 1998) for a head-on collision. As a meteoroid passes through the atmosphere it releases ions, free electrons, and light.

The term "meteor" refers to the meteoroid, column of ionization, and light as it passes through the atmosphere. Meteors themselves are also referred to as "fireballs" or "bolides" if they are very bright events, or traditionally for bolides, if they are events which appear to detonate in the atmosphere. Some meteors survive their passage through the atmosphere and reach the Earth.

If the meteoroid is not completely vaporised in the atmosphere, it will land on the Earth's surface and is called a meteorite. Meteorites tend to be composed of strong, stony or iron material; and range in size from rocks large enough to crater the Earth down to dust-sized particles called micrometeorites.

Micrometeorites are an exception to the ablation process. They are the result of very small meteoroids, in the size range of dust grains, which have large surface areas relative to their masses. They become meteorites because their kinetic energy is radiated away at low temperatures and the meteoroid does not vaporise (McKinley, 1961). Compared to meteorites, micrometeorites have a very long fall duration; minutes for a meteorite fall compared to days or even weeks for a micrometeorite to land.

## 1.2 Why Sporadic Meteors are Relevant

With the continuing exploration of the solar system, it becomes increasingly important to understand the distribution of small bodies in interplanetary space, and the potential hazards they may present to spacecraft. Collisions of spacecraft with these small bodies can have serious repercussions such as spacecraft failure, and in the case of crewed missions, loss of life. The distributions of meteoroid sizes, orbits, and compositions give us a representation of the solar system in its present state and its past evolution (McCord & Morris & Persing & Tagliaferri & Jacobs, 1995). By studying meteors observed in the Earth's atmosphere, we can sample and assess this population and gain insight into the numeric flux, mass and speed distributions, and orbits of these bodies.

Both mass and velocity distributions are of interest because the damage that can be inflicted by a collision with a meteoroid is proportional to the kinetic energy of the meteoroid. Unlike low-velocity collisions, the meteoroid and part of the target are vaporized. The damage to spacecraft occurs when the plasma cloud of the vaporized

meteoroid discharges in the electronics. The energy of the plasma is proportional to the kinetic energy of the meteoroid and since the damage is caused by the plasma rather than deformation from the impact, kinetic energy is the determining factor in the damage from meteoroid collisions. Because the kinetic energy is $\frac{mv^2}{2}$, the velocity of the meteoroid is more significant than the mass. Because the ionization or luminosity is proportional to the kinetic energy, an important quantity to consider is the limiting mass of the observing system. The limiting mass is the smallest mass for which all meteors of equal or greater mass will be seen by the system. Similarly, the limiting magnitude is the faintest meteor magnitude for which a system will detect all meteors of equal or greater brightness. These quantities are very important in flux studies, because the distribution meteoroid masses follow a power law, and the number of observed meteors will directly depend on sensitivity.

The flux of interest is the number of meteors per area per time. In most cases this is reported in number of meteors per $km^2$ per hr. To determine this flux we must calculate both the number of meteors detected and the collecting area – the area covered by the observing system. The number of meteors itself is a simple matter of counting the number of meteors observed by a system, while the calculation of collecting area is much more difficult. Brown et al. (2002a) calculated the collecting area of a video system by projecting the field of view onto the meteor zone, typically centred at a height of 100 km. Their calculation does not include the sensitivity profile of the cameras and curvature of the Earth, and made the assumption that meteors are confined to a limited distribution of ranges; however, for elevations less

than 30° they estimated that this produced a collecting area accurate to better than 5%.

As indicated by the mention of the sensitivity profile, there are observing biases that must be considered for an accurate flux calculation. These observing biases will vary depending on the detector. Uncorrected observing biases result in a poorly represented sample of the population being studied. The identification and estimation of these biases is necessary to extrapolate the measured sample to take into account the entire population of meteors, or the entire mass of a meteoroid.

Previous studies have considered a variety of biases. Brown and Jones (1995) calculated relative sporadic source activity with radar and considered the biases from collecting area, antenna gain, collecting efficiency, and initial trail radius. It is important to note that the biases were too uncertain to attempt an error analysis. Visual studies of the Perseid meteor shower have also been conducted, taking into account observer perception – which takes into account difference in brightness from the limiting magnitude, and the angular distance from the centre of the observer's field of view, radiant altitude, and effective collecting area (Brown & Rendtel, 1996). Unfortunately, it is difficult to determine a uniform correction for all visual observers because of the differences in the individual perceptions. McCrosky and Posen (1968) introduced corrections to the trajectory data for photographic meteors observed by the Prairie Network. The data were first corrected for astronomical refraction (apparent star positions are incorrect due to refraction of their light in the atmosphere); and from a preliminary trajectory solution, corrections are derived for partial refraction (correction for the difference between astronomical refraction and the refraction of a

meteor penetrating deep into the atmosphere), refractive parallax (correction to the true direction to the meteor), and gravity (correction for deviations from a linear trajectory due to gravity). In terms of photometry, they corrected the magnitude of star trails for vignetting, extinction, colour, and shutter cycle, and they corrected the meteor magnitude for extinction, vignetting, trailing rate, and range. Of particular interest to this study, electro-optical observations of the Leonid shower were made in 1998 (Campbell & Brown & LeBlanc & Hawkes & Jones, 2000) and 1999 (Brown et al, 2002a) with bias corrections for height, range, partial trail, and collection area.

The Leonid meteor shower is an example of a confined stream of meteoroids; however, other meteoroids exist and in general meteoroid populations are classified as either:

1. Streams, which are groupings of meteoroids sharing a common orbit; or
2. Sporadic, which are too dispersed to be called streams.

Ground-based detectors only observe those that enter the Earth's atmosphere; the corresponding meteor terms, shower and sporadic, are often used. At the time of writing, no study of sporadic flux has been undertaken using video data; however, the mass flux of meteors, shower and sporadic, has been estimated by Ceplecha (2001) from a combination of several studies as $1.3 \times 10^8$ kg/yr, and with the exception of times at which major showers exist, the majority of the flux is sporadic in nature (about three quarters of all visually observable meteors are sporadic) (Ceplecha et al, 1998).

## 1.3 Origins of Meteors

The origins of meteoroids are of interest in order to gain insight into the properties of the parent bodies, and to understand the dynamics of the solar system. Meteoroids are produced by ejection from comet nuclei and collisional processes in the asteroid belt.

Shower meteors come from meteoroids which are confined to well defined streams which encounter the Earth's orbit at a particular solar longitude each year. The names of the showers are derived from the constellation from which they appear to originate. When considering the orbits of these streams, sometimes a comet or asteroid can be found with a similar orbit and identified as the source of the meteoroids. Meteoroid streams may be deposited by comets which are composed of meteoritic material and hydrides. As the hydride ices sublimate, the momentum of the outward flowing gasses pushes meteoric material away from the comet nucleus against the gravitational force until the ejected particles are beyond the radius of the comet (Whipple, 1951). The ejection velocities are small compared to the velocity of the parent and the meteoroids retain an orbit very close to the comet, and are travelling along nearly parallel paths. The parallel paths result in the meteoroids appearing to come from one point in the sky called the radiant.

Over time the stream is dispersed until the parent body is no longer identifiable. Gravitational perturbations, the Poynting-Robertson effect, and the Yarkovsky effect are responsible for the dispersion of the stream (Wiegert & Vaubaillon & Campbell-Brown, 2009). The Poynting-Robertson effect describes the change of a body's orbit by decreasing eccentricity and the semi-major axis of the

orbit by non-uniform momentum transfer by emitted photons (Campbell-Brown, 2005); eventually particles spiral into the sun. The Yarkovsky effect describes a combination of rotational and orbital changes which vary based on the shape of individual meteoroids. Because meteoroids have non-spherical shapes, they emit and reflect photons in non-uniform distributions, these distributions result in unbalanced momentum transfers which can cause meteoroid rotation and an increase or decrease in the eccentricity of the meteoroid orbit. Dispersed stream meteoroids join with the sporadic meteoroid population.

Meteoroids with no associated stream are referred to as sporadic. Unlike meteor showers, sporadic meteors have no specific solar longitude at which they hit the Earth and are therefore detectable year round. Sporadic meteors comprise most of the meteor population, and dominate the distribution at smaller meteoroid sizes (Campbell-Brown & Brown, 2005). Several sources with broad radiant distributions have been identified: antihelion (AH), helion (H), north toroidal (NT), south toroidal (ST), north apex (NA), and south apex (SA). Jones and Brown (1993) summarize their positions in sun-centred ecliptic coordinates (0° ecliptic longitude is defined as the position of the sun and ecliptic latitude is defined as the angular distance from the Earth's orbital plane) and radii in Table 1.1. Note that the south apex source has too little available data to provide a well defined radius; however, Chau et al (2007) have shown symmetry between the NA and SA sporadic sources and so the radius is assumed to be the same for both sources.

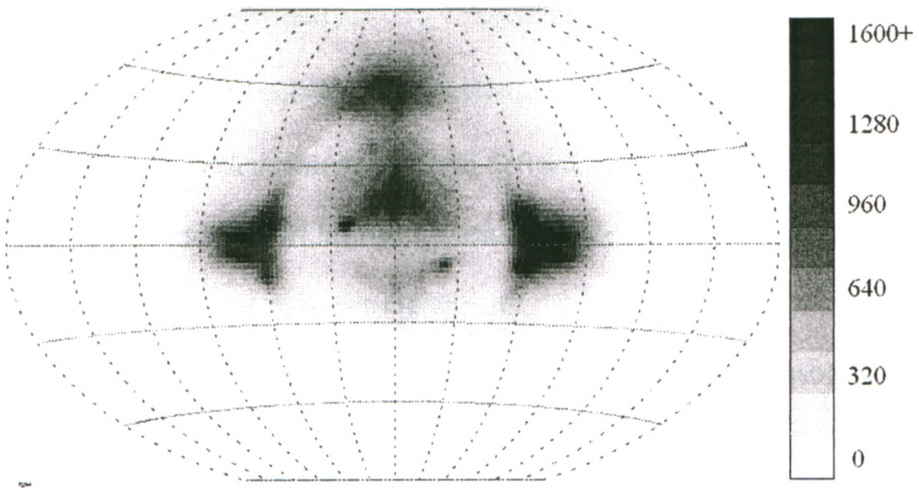


**Figure 1.1: Sporadic sources as plotted by CMOR. Number of orbits per two degree bin is plotted in ecliptic latitude and longitude, with the apex of the Earth's way (direction of the Earth's motion around the sun) at the centre of the plot and the sun 90 degrees to the left. Strong dots and structure seen in sporadic sources are the result of meteor showers (Campbell-Brown, 2008).**

| Source | AH | H | NT | ST | NA | SA |
|---|---|---|---|---|---|---|
| Position (lon, lat) (°) | 198, 0 | 342, 0 | 271, 58 | 274, -60 | 271, 19 | 273, -11 |
| Radii (°) | 18 | 16 | 19 | 16 | 21 | 21 |

**Table 1.1: Sporadic Sources in ecliptic coordinates (Jones & Brown, 1993)**

The AH and H sources are the most prominent and are the source of roughly two thirds of the sporadic flux at microgram masses. Two separate models have been used to determine the relative activities of the sources:

1. Empirical model, in which activities were calculated for the sporadic sources with positions and radii defined by observational data; and
2. Symmetric model, in which positions and radii for the sporadic sources were symmetric about the apex of the Earth's way. The radii of the sporadic sources were taken as the mean radius of the associated pairs (AH-H, NA-SA, NT-ST) (Brown & Jones, 1995).

The orbits of these meteoroids are almost identical to those of short period comets, and the AH source was measured to be slightly more active than the H source by Brown and Jones (1995) using the empirical model. From the symmetric model the AH source comprises 33 ± 5 % of the total flux, and the H source comprises 36 ± 9 %; whereas with the empirical model AH represents 30 ± 5 % and H represents 29 ± 7 %.

Meteoroid lifetimes, for meteoroid sizes greater than 1 mm, are limited by several factors of varying significance. Collisions are the dominant limitation for meteoroid lifetimes. Collisions break the meteoroids into smaller fragments and through momentum transfer, change their orbits. The next most significant limitation is the Poynting-Robertson effect. Lastly the Yarkovsky effect produces a small shape-dependent change of the orbit.

## 1.4 Meteor Process

Both shower and sporadic meteors are detected by their transit through the atmosphere. Early in this transit the meteoroid encounters a very thin atmosphere

where there are few atmospheric molecules for collisions to occur. If the meteoroid is small it will have significant deceleration in this region (Ceplecha et al, 1998). As the meteoroid continues deeper into the increasingly dense atmosphere, collisions with atmospheric molecules heat the meteoroid and it begins ablating. Ablation refers to the loss of mass from the body through the release of solid, liquid, or gas, and at low temperatures is comprised of fragmentation (loss of solid mass). Meteor ablation depends on the velocity of the meteoroid. It is important to note that for meteors with high velocities the energy required to completely ablate the meteor body is orders of magnitude smaller than the initial kinetic energy of the meteoroid (Zinn & Judd & ReVelle, 2003).

As it passes through the atmosphere, the collisions with atmospheric molecules dissipate the kinetic energy of the meteoroid in the form of heat, light and ionization, though dissipation as heat is the dominant form (McKinley, 1961). Deeper in the atmosphere a diffuse shock wave forms and the meteoroid is shielded from further impacts by a layer of vaporized atoms (Ceplecha et al, 1998). The kinetic energies are high enough that the vaporised atoms are excited and ionized. Most of the visible light from meteors is the result of radiation produced by the de-excitation of atoms in the hot vapour. The power involved in the production of both light and ionization is proportional to the kinetic energy lost by the ablated atoms. As the density of the atmosphere increases, ionization and radiation will increase to a maximum which depends on the size of the body; and then decrease as the body continues to ablate (McKinley, 1961).

Early meteor theory assumed that the meteoroid travelled as a solid body; however, this assumption failed to describe faint meteor light curves and decelerations. McKinley (1961) proposed the concept of fragmentation, based on the assumption that "the average meteoroid has a fragile structure which breaks up easily into a cluster of small fragments on impact with the upper atmosphere." Currently fragmentation is understood to be a continual and/or instantaneous (also called "gross fragmentation") process common for all but large iron bodies. Fragmentation occurs when the stagnation pressures (the pressure of the atmosphere on the meteoroid) exceed the tensile and compressive strengths of the body (Ceplecha et al, 1998). Pressure is not sufficient to explain the fragmentation of small bodies, and a model has been developed to consider thermal disruption – the melting of bonding material in the dust ball model of meteoroids (Campell-Brown & Koschny, 2004). Ceplecha et al (1998) have developed a model to describe the meteor through a limited number of gross fragmentation points, which has been verified with observations from the Prairie Fireball Network.

## 1.5 Meteor Detection

To differentiate between shower and sporadic meteors we must observe their trajectories to determine their orbits before they collided with the Earth. Upon determining the orbits we are able to separate the observed flux of meteors through the Earth's atmosphere into known showers and sporadic meteors. An ideal measurement of a meteor would encompass all of the following sets of data (Ceplecha et al, 1998):

i) Orbital data; the path of the meteoroid through the solar system

ii) Geometrical data; position of the trajectory in the atmosphere

iii) Dynamical data; height and distance along the trajectory as a function of time, velocity, and deceleration

iv) Photometric data; integrated light intensity in the complete pass-band as a function of time

v) Spectral data; intensity radiated in individual spectral lines and molecular bands as a function of time and,

vi) Ionizational data; density of ions and free electrons as a function of time

Several different methods exist to measure segments of the ideal data set, each with its own advantages and disadvantages. Radar systems, infrasonic measurements, visual observers, photographic observations, video systems, and spectral systems are all used to observe meteors.

### 1.5.1 Radar Systems

Radar systems detect meteors by emitting radio waves and observing the signal scattered by the ionized trail of the meteor. All radars measure echo range, the distance from the station to the meteor, and echo phase, a measurement of the relative range which can be used to find the angular velocity. Some radars are also able to measure speed, meteor radiant, and ionization. Because radar systems observe ionization they are not limited by daylight hours or by weather conditions as optical

systems are. Orbits calculated by transverse scatter (also called 'body echo') radar are often more uncertain than those calculated by optical means. HPLA (high power large aperture) radars using radial scatter (also called 'head echo') produce orbits more precise than photographic methods (Campbell-Brown, 2005). Transverse scatter radar systems are limited by other biases such as the initial trail radius effect, which causes destructive interference when the width of the trail is roughly the same as the wavelength of the radar and reduces the detection efficiency for meteors ablating high in the atmosphere (Greenhow, 1963). HPLAs are currently hindered by uncertain bias corrections, no current calculation of collecting area, lack of a mass scale for most systems, and the high cost of operation. Because of the biases associated with radar systems, fluxes measured with other detectors are needed for calibration and verification.

### 1.5.2 Optical Systems

Meteors have been recorded by visual observers for thousands of years; however, only in the last century have these become coordinated observations. Initially composed of groups of people observing the night sky, optical systems have evolved to use photographic film and digital video systems. This has led to an extension of the visible magnitudes from +4 (Brown & Šimek & Jones & Arlt & Hocking, 1998) to +9 magnitude (Ceplecha et al, 1998). For accurate trajectory information, modern optical studies use at least two stations with post processing to identify the radiant based on direction and velocity of the meteor. Optical systems also measure the light radiated from the meteor, and mass is determined by integration of the light observed over the duration of the meteor. Because the ability

of a body to produce light depends on its mass and velocity, this leaves a broad range of masses which may be observed optically. The greatest disadvantage of optical methods is that they are restricted to clear, nighttime observations, and other luminous objects such as stars or satellites can increase the uncertainties of luminosity observations if the meteor trail crosses these objects in the field of view. Most optical systems do not have a uniform sensitivity across the field of view, and all image intensified systems show a difference in sensitivity between the centre and edge of the field of view (Hawkes & Mason & Fleming & Stultz, 1993). The most uncertain quantity of optical studies is the luminous efficiency which is the efficiency of energy converted from the kinetic energy of the meteoroid to light.

Spectral systems use a prism or transmission grating to look for the compositions of meteors. Composition is determined based on the emission and absorption lines observed from the light after it has passed through the prism or grating, and "the most prominent features of meteor spectra were found to be emission lines" (Ceplecha et al, 1998). These systems have evolved from photographic to digital video systems.

Photographic and video systems themselves have different advantages and disadvantages. While photographic systems have a higher resolution, video systems are more sensitive to light, especially when optically coupled to an image intensifier. Early image intensified video systems were more sensitive to light than photographic systems by several magnitudes (Hawkes & Jones, 1973) and video systems remain much more sensitive than photographic systems today (Molau & Gural, 2005). While

the increase in sensitivity leads to more meteor detections the reduced resolution increases the uncertainties in all dynamical data are increased.

## 1.6 Thesis Goals

The smallest meteoroid size able to produce a meteor depends on speed, and is approximately 0.01 mm in diameter (Ceplecha et al, 1998); there is no size limit for larger bodies. This distribution of sizes is assumed to be representative of the distribution of small bodies throughout the solar system. Studies have shown that by analysing the flux of shower meteors through our atmosphere we are able to extrapolate the distribution of bodies throughout the solar system (Pawlowski & Hebert & Hawkes & Matney & Stansbery, 2001). It is with this in mind that the current study seeks to determine the flux of sporadic meteors. It is important to note that objects with masses on the order of grams represent a peak (Figure 1.2) in the incremental mass distribution of meteoric flux (Ceplecha et al, 1998), and this mass falls within the magnitude range that has been chosen for this study.

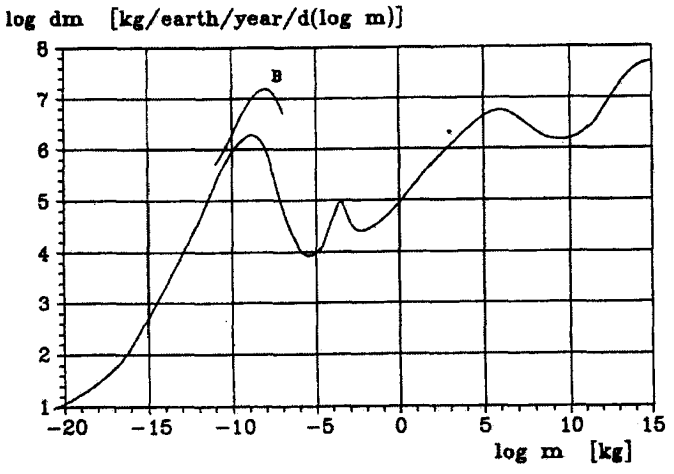


**Figure 1.2: Increment of mass, log dm, per one order of mass per the entire Earth's surface per year is plotted against the logarithm of mass, log m (Ceplecha et al, 1998)**

The goals of this thesis include calculation of the flux, mass distribution, and speed distribution of meteors in the $4^{th}$ to $6^{th}$ absolute visual magnitude range.

# 2. Equipment and Methods

## 2.1 Video Systems

### 2.1.1 Setup

Accidental photographs of meteors have been taken since the beginning of astronomical photography. The use of rotating shutters to segment meteor trails has allowed positional measurements to be made along the trail, but if the meteor fragments, these can be blurred out. Only bright meteors can be observed with photographic film, due to the limits of its sensitivity. Using video eliminates blurring of trail segments due to fragmentation, and using intensified video allows fainter meteors to be observed. When considering video systems, limiting sensitivity and resolution are the most important parameters. Because the number of meteors is expected to increase with decreasing mass (Ceplecha, 1996), the limiting sensitivity affects the number of observable meteors. As limiting sensitivity controls the quantity of data, resolution controls the quality. Higher resolution allows more accurate measurements of position which is the basic quantity from which trajectory information is calculated. In intensified video systems resolution is generally expressed in TV lines or line pairs per mm of the input photocathode (Hawkes & Jones, 1986). Significant improvements have been made to both these quantities since the early video meteor studies in the 1960's.

The first low light level television (LLLTV) studies were conducted with image orthicon cameras. The cameras had a resolution of 10 lines $mm^{-1}$ (500 TV lines), a frame rate of 30 fps (standard television rate), and a limiting magnitude of

+6.0 (Spalding & Colter & Hemenway & Cole & Dugan, 1963) and were used to record single station images of the Perseid meteor shower.

The next step in technology came in the 1970s with the addition of an optically coupled image intensifier. First generation image intensifiers used a photocathode followed by an accelerating electron lens focused onto a phosphor output window. The optical gains of the image intensifiers range from 30 to 100 000; however, setting several of them in sequence results in gains of the order 100 000 (Hawkes & Jones, 1986). Clifton (1971) compared a single stage intensified secondary electron conduction (I-SEC) vidicon camera to an image orthicon video system of equal limiting stellar magnitude. The I-SEC vidicon was determined to be superior to the image orthicon system for the detection of faster meteors. An example of a multi-staged first generation image intensified system can be found in Hawkes and Jones (1973), which describes a three stage intensified vidicon camera used to observe sporadic meteors. The gain was estimated to be 60000 resulting in a limiting meteor magnitude between +6.5 and +7.5. The resolution was 200 TV lines read at 30 fps, which is lower than the resolution of the orthicon system. New camera technology can also improve the sensitivity as seen in the I-SIT system. The acronym *I-SIT* stands for Intensified *S*ilicon *I*ntensified *T*arget and refers to the image intensifier and electro-optical detector. Using a single stage intensifier, the system has a stellar sensitivity of +9 compared to +8 for the Hawkes and Jones (1973) system. Note that the faintest star is fainter than the faintest meteor, since stars are stationary in single frames while meteor light is smeared over many pixels. The resolution of the system is better with 240 TV lines, and the frame rate is 30 fps

(Sarma & Jones, 1985). It is clear that advancing technology has rapidly increased the limiting sensitivity of video systems, but improvements have not yet been shown in terms of resolution.

Because resolution depends on the size of the area being observed, looking at a smaller area with the same system increases the resolution; therefore, the simplest way to increase the resolution of a system is to use a lens with a longer focal length. The drawback to this solution is that the field of view and therefore the detection rates decrease; also, most meteor trails will be incomplete. The introduction of solid state charge coupled devices (CCDs) has expanded the range of resolutions available from early 244 x 248 picture elements called pixels (Hawkes & Jones, 1986) to more recent sizes of 4096 x 4096 pixels (Howell, 2000). The number of pixels represents the upper limit of possible resolution in TV lines.

The system used in this study has been used in several other studies (Campbell et al, 2000; Campbell & Theijsmeijer & Jones & Hawkes & Brown, 2001; Brown et al, 2002a; Brown & Campbell & Suggs & Cooke & Theijsmeijer, 2002b), and consists of three COHU 4910 cameras using ITT Gen III image intensifiers. Table 2.1 contains the specifics for each camera, including the longitude and latitude of the observing site, and the altitude and azimuth of the pointing direction for each camera. Cameras Q and T were located at the same site; however, they have different objective lens focal lengths.

| Camera Letter | Lens | Field of View | Longitude | Latitude | Altitude | Azimuth |
|---|---|---|---|---|---|---|
| Q | 50 mm | ~18° | -110.953° | 31.675° | 60.0° | 267.0° |
| S | 25 mm | ~36° | -111.600° | 31.962° | 72.4° | 352.2° |
| T | 25 mm | ~36° | -110.953° | 31.675° | 60.0° | 267.0° |

**Table 2.1: Camera Information**

The resulting baseline between the observing sites was 75km. The Gen III image intensifiers used are especially sensitive in the red and near infrared regions. Data was recorded during the nights April 27, 2006 to May 6, 2006 with the exception of one night during which weather conditions prevented observation. The data were recorded to either Maxell P6-120HMBQ Hi 8 or JVC HMP Metal Particle HMP120NTSC Hi 8 digital cassette tapes using digital camcorders. Roughly 44 hours of operational time were recorded per camera. The common volume observed by all three cameras was southwest of Tucson, AZ.

### 2.1.2 Identification

Until recently, one of the biggest drawbacks to video studies was the effort involved in finding meteors and then processing the data from video tapes. It was necessary for an observer to review the tapes twice; any additional revisions resulted in less than 10% new detections (Hawkes & Jones, 1975). To quicken this step in the analysis, several software packages have been developed using three major methods: clustering and thresholding, spatial correlation, and temporal correlation.

Clustering and thresholding algorithms operate by searching for groups of pixels in an image that have values above the background threshold. The software package "MetRec" is an example of clustering and thresholding detection software, and it has been used in several autonomous systems (Molau, 1999).

Spatial correlation software operates in one of two ways: either by applying templates of line segments of different orientations to the image or by using a Hough transform. In the case of applying templates of line segments, many different templates of randomly oriented lines are generated and then compared to the pixels

above a threshold value in the image. If a match is found, detection is confirmed. The Hough transform maps Cartesian coordinates (x,y) to Hough space (p,φ) where the coordinates represent the parameterized line defined by (Gural, 1997):

$$p = x\cos(\varphi) + y\sin(\varphi) \qquad (2.1)$$

While the previous two methods searched for meteors within one frame, temporal correlation instead tracks detections across multiple frames of video data to match conditions for linear propagation; alternatively, matched filtering can be used to follow a path based on an estimated position and velocity (Molau & Gural, 2005). "Meteorscan" is a program which uses both spatial and temporal correlations to detect meteors. "UFO Capture" is another program that has been used in meteor detection, and it uses a combination of masking stationary light sources and thresholding to detect moving objects (Molau & Gural, 2005).

"Meteorscan" applies two correlations and achieves a run-time probability of detection of 80% or a post-process probability of detection (taking longer than real-time) of 99% under ideal settings (Molau & Gural, 2005). The almost perfect probability of detection is the reason that "Meteorscan" was selected for use in this study. The software looks for pixels with a value above some threshold then applies a Hough transform to look for co-linear pixels.

A meteor is detected by the bright co-linear points of the trail. Furthermore, the Hough transform is used in a matched-filter to track the meteor through several frames. This method has the unfortunate side effect of generating many false positives (> 20%) (Molau & Gural, 2005). Despite the false detections, the process is much less labour-intensive than identifying meteors by eye.

For the current project, "Meteorscan" was used to detect the meteors in the data tapes and extract a window of frames around the meteor after the detection was confirmed by a user. The total processing time, including confirmation, is estimated to be on average 1.5 times the length of the data tape; however, it was found that for one of the 25 mm cameras atmospheric scintillations caused a very high rate of false detections because of the increased number of pixels above the threshold value, and the processing time was roughly 2 times the length of the data. The actual time spent by a user in confirming meteors was significantly less, and the automation allowed the detections to be run overnight. The settings for "Meteorscan" (including the thresholds for detection and the length in frames retained per possible detection) are listed in Appendix A, and with the exception of the number of frames saved were the same for all data. Several hours of data were reduced before it was noticed that the frame buffer of the detections was not set to retain the maximum number of frames. Because the light curves of the meteors were analysed, as many frames as possible were desired for accuracy. After the extraction was complete, the frames were converted from Tagged Image File Format (TIFF) images, the output format of "Meteorscan", to Portable Network Graphics (PNG) format, the input format for "Photom", which was used to analyse the video frames.

## 2.2 Analysis

The analysis of a meteor using video observations comes in two parts. First, the position is determined in order to calculate the trajectory and orbit, generally referred to as astrometry. Second, the light emitted by the meteor is analysed to

determine the mass. Using current software with as much automation as is possible with reasonable accuracy, one meteor on one camera took roughly one half hour to analyse. Additionally, the time to make sufficient astrometric plates to confirm that there was no shift in the camera over the course of each night took up to a few hours, because of the time involved in matching stars in the field of view to the stars in the catalogue. Due to the time involved in analysing the first night of data, only two of the nine nights have been processed in full. The second night was chosen for the likelihood of observing the Eta Aquariid shower to compare fluxes with literature values. This resulted in 235 multi-station meteors of which 26 had too few points to be useable light curves, and 6 were saturated. Saturation describes an object which is so bright that it produces more light than a pixel can detect. Some of the light is lost and some is picked up in adjacent pixels. In meteor physics this is a problem because the light is used to calculate the mass of the meteoroid, and thus the mass is underestimated due to the photons not counted by the CCD. All of the remaining nights of data have been reduced to sets of frames containing meteors, ready for future analysis.

### 2.2.1 Astrometry

To calculate the trajectory of a meteor we follow several steps of calibration and calculation. In general the analysis will follow the approach of Hawkes et al (1993). First, the apparent spatial coordinates (altitude and azimuth) of the meteor must be determined from each station. Second, lines of best fit must be calculated to the beginning and end of the trail for each station. Third, the radiant vector must be calculated. Fourth, the true meteor trajectory must be triangulated. Following these

steps leads to a better fit to the trajectory than previous methods which triangulated individual points.

There are two important limits which apply to these solutions, because we have used an optical system. A major limit for the detection of meteors in the field of view is the angular velocity of the meteor from each station. With increasing angular velocity, the light of the meteor is spread over an increased number of pixels, and a sensitivity limit exists where the light per pixel is at the level of the background, rendering the meteor undetectable. Alternately, if the angular velocity is too small, the meteor will not be identified as a moving body. The latter case represents a limit to detection due to the geometry of the stations. If a meteor is travelling directly toward one station, it will have a very small angular velocity with respect to that station, and it will only be possible to identify it as a meteor at the other station.

The second limitation resulting from the station geometry is in the trajectory solution. If the distance between stations (often called the baseline) is too small, the error in the height of the meteor will increase greatly (Fig 2.1 left). If the stations are too far apart, the error in the position of the meteor will increase (Fig 2.1 right). In either case, the overall uncertainty of the trajectory will increase due to the uncertainty of the fit.

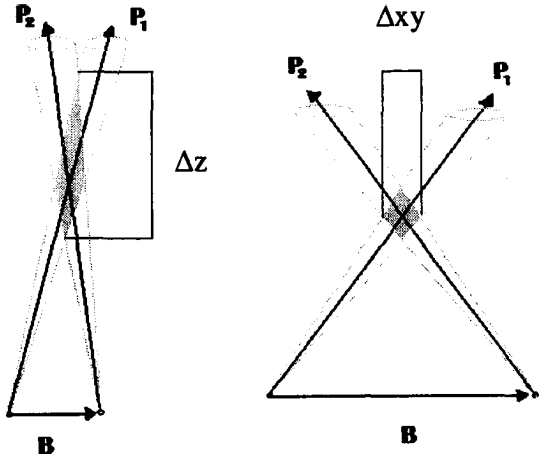


**Figure 2.1: Examples of increased error in stations. Short baseline (left) increases error in height, and a long baseline increases the error in the xy plane.**

When a meteor is detected by the observing system, corrections must be applied for the effects of the atmosphere and gravity. The simplest correction to apply is for the astronomical refraction of the stars. This atmospheric refraction affects the constants for the astrometric plate and the correction can be computed from atmospheric pressure and temperature data for the observing site at the time of observation (McCrosky & Posen, 1968).

The astronomical refraction correction (refraction for complete atmosphere) is used to calculate the correction for the refractive parallax (refraction of a partial atmosphere due to a meteor located within the atmosphere). McCrosky and Posen (1968) compute the refractive parallax correction using the range $R$ from the station to the meteor and the distance perpendicular to the corrected line of sight $K$. $K$ depends on the index of refraction $n$ at a station, the astronomical refraction $r_\infty$, and the zenith angle $z$. For $z < 88°$, they computed $K$ using the following empirical relation:

$$K \propto \frac{r_\infty}{\cos z + 0.00569/\sqrt{\cos z}} \qquad (2.2)$$

The final correction for gravity describes the deviation from a linear trail due to the pull of gravity. The correction is minor compared to the other corrections, but it becomes more significant for slower meteors with longer trail lengths. The non-linearity increases with time and proximity to Earth. The correction must be applied to correct for range and orientation of the meteor, and has the general form (McCrosky & Posen, 1968):

$$G = \frac{gt^2}{2} \tag{2.3}$$

Here $g$ is the acceleration due to gravity equal to 9.81 m $s^{-2}$, and $t$ is the time of flight. In this study astrometric plates were calculated on a nightly basis, and so these corrections have been incorporated into the plate calibrations.

The apparent equatorial position of a meteor in a video frame can be determined by comparing its Cartesian position in the frame to the Cartesian positions of known stars and calculating the parameters for an astrometric plate (Wray, 1967). The parameters for the astrometric plate are calculated by applying a third order least squares polynomial fit between the coordinates of the reference stars and the expected positions of those stars in an ideal image (Hawkes et al, 1993). The Cartesian coordinates (x,y) of the star are converted to equatorial coordinates ($\alpha$,$\delta$) and a "plate centre" is defined by equatorial coordinates ($\alpha_o$,$\delta_o$). Each star is mapped to the ideal system($\xi$ – points in the direction of increasing right ascension, $\eta$ – points along a circle towards the north celestial pole) using the method of Wray as implemented in Hawkes et al (1993):

$$\Delta\alpha = \alpha - \alpha_o \tag{2.4}$$

$$\Delta\delta = \delta - \delta_o \tag{2.5}$$

$$\xi = \frac{\cos\delta \sin\Delta\alpha}{D} \tag{2.6}$$

$$\eta = \frac{\sin\Delta\delta + \cos\delta \sin\delta_o[1-\cos\Delta\alpha]}{D} \tag{2.7}$$

Where D is:

$$D = \cos\Delta\delta + \cos\delta \cos\delta_o[\cos\Delta\alpha - 1] \tag{2.8}$$

The actual meteor positions (there will be a set for each station) will be defined by a set of vectors from the station to the meteor point of the form **P** according to Wray (1967):

$$P_x = \cos\delta_o - \eta \sin\delta_o \tag{2.9}$$

$$P_y = \xi \tag{2.10}$$

$$P_z = \sin\delta_o + \eta \cos\delta_o \tag{2.11}$$

In this study, astrometric plates and meteor positions are determined using the program "Photom" written by R. Weryk. Plate fits were accepted if the average error in the fit (in matching a measured star to its predicted position) was less than the resolution uncertainty, the angular width of one half of one pixel for a camera with objective focal length *f* (*f* = 25mm; 0.5 pixel = 0.025°, *f* = 50mm; 0.5 pixel = 0.0125°). In order to verify the accuracy and consistency of the astrometric fits, several plates are computed at different times throughout the night. Plate comparisons verified that the standard deviation was less than the resolution uncertainty of the cameras. A measure of the position of a meteor in the video frame was taken based on the leading edge of the meteor trail. This choice is subject to errors introduced by blooming; however, it was deemed the most accurate method of identifying a consistent position reference for the meteor. Ideally, one would calculate the width of the front the meteor trail and then find the position as a point

half the measured width behind the leading edge of the meteor. The improvement would in most cases be slight, approximately 10-15 pixels from the front of the meteor; however, this is frequently spread over several frames so the relative differences between adjacent frames are small, and the extra time needed would be significant.

Using the set of position vectors for the meteor, the plane of best fit, containing the observing site and the line of the meteor trajectory, can be determined. To minimize the error introduced by individual points a weighted average of the vector product of all vector pairs from one station is calculated according to the following:

$$N = \sum_{i=2}^{n} \sum_{j=1}^{i-1} P_i \, X \, P_j \qquad (2.12)$$

Here, **n** is the normal of the plane of best fit, and the **P** vectors are unit vectors from the stations to the points on the meteor trail. The summation serves to weigh the vectors inversely according to the sine of the angle between them. The weighting is important because for two closer vectors the magnitude of the cross product will be smaller resulting in a larger relative uncertainty.

After obtaining the normal vectors for each station's meteor plane, the radiant vector can be determined using the vector product of the normal vectors:

$$r = \pm n_1 \, X \, n_2 \qquad (2.13)$$

The sign in front of $\mathbf{n_1}$ can be determined by converting the equatorial coordinates to an Earth-based Cartesian system. First the right ascension, $\alpha$, and the declination, $\delta$, are converted to a Cartesian system.

$$x_s = \cos\alpha \cos\delta \qquad (2.14)$$

$$y_s = \sin\alpha\cos\delta \tag{2.15}$$

$$z_s = \sin\delta \tag{2.16}$$

Then the Cartesian coordinates in Equations 2.14 – 2.16 are translated to an Earth based frame according to the following:

$$\begin{bmatrix} x_e \\ y_e \\ z_e \end{bmatrix} = \begin{Bmatrix} -\sin\tau & \cos\tau & 0 \\ -\sin\lambda\cos\tau & -\sin\lambda\sin\tau & \cos\lambda \\ \cos\lambda\cos\tau & \cos\lambda\sin\tau & \sin\lambda \end{Bmatrix} \begin{bmatrix} x_s \\ y_s \\ z_s \end{bmatrix} \tag{2.17}$$

Here, $\lambda$ is the latitude and $\tau$ is the local mean sidereal time. The next step of the triangulation can now be calculated using the radiant (the point from which the meteor appears to originate) vector, **r** and any two position vectors (one from each station) as shown in Figure 2.2. The line of intersection of the planes can be calculated using a system of equations built from the general formula:

$$C_1\,\mathbf{P_1} = \mathbf{B} + C_2\mathbf{P_2} + C_r\mathbf{r} \tag{2.18}$$

Where $\boldsymbol{P_1}$ and $\boldsymbol{P_2}$ are unit vectors from the stations in the direction of the beginning and end points and *C*s refer to the range from the station to the apparent beginning, end, and radiant of the meteor. $\boldsymbol{B}$ is the baseline vector from station 1 to station 2. Ideally the chosen position vectors would be those closest to the line of intersection.

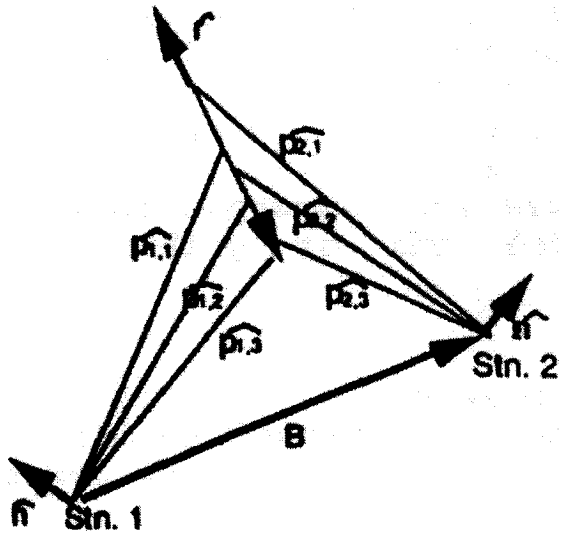


**Figure 2.2: Triangulation of a meteor with two stations (Hawkes et al, 1993).**

The beginning and end vectors for each station along with the baseline vector, and the radiant vector can be used with parameters corresponding to the apparent ranges to triangulate the best fit of the meteor trajectory. Triangulation of the points was accomplished using the "MILIG" software package which performs a non-linear least squares fit to the planar solutions, beginning with a first approximation using the beginning and end points on the trajectory from both stations (Borovička, 1990).

After corrections have been applied and the solution calculated, we have a precise radiant and velocity from which the orbit can be computed. The computation of orbital parameters is beyond the scope of this study. Because we are concerned only with the sporadic flux, radiant and velocity are sufficient for determining if a meteor is sporadic. In this study, meteors were accepted for the purpose of flux calculation if they met the following conditions:

1. The maximum luminosity was observed by both stations.
2. Had trajectory solutions with reasonable beginning heights from 70km (below lowest point seen by both cameras) to 120km (higher than theoretical video beginning heights) (Hawkes & Jones & Ceplecha, 1984)
3. Had velocities within the range 11.2km $s^{-1}$ – 72km $s^{-1}$ as discussed in Chapter 1

Of the 246 meteors detected as possible multi-station meteors, 4.5% were rejected based on obvious errors in the trajectory solution on grounds ranging from negative heights (i.e. meteor observed inside the Earth) to mixed negative and positive velocities (i.e. one camera observed the meteor's apparent motion towards the Earth and the other observed its apparent motion away from the Earth) to a few with velocities approaching or in excess of the lower limit galactic escape velocity of 400 km $s^{-1}$ (Carney & Latham, 1987). In addition to the meteors rejected because of their trajectories a small number were rejected because of visible geometric disagreements between stations. These erroneous solutions arose from either the simultaneous detection of two separate meteors, insufficient frames at one or more stations for an accurate solution, or poor meteor geometry conditions approaching the limits of detection (i.e. the meteor trajectory was close to the line of sight of one of the cameras).

### 2.2.3 Photometry

In addition to the positional measurement in each frame of a video meteor there is also a measurement of the light it emitted through ablation. The set of points representing the magnitude of the light emitted as a function of time are collectively called the 'light curve' of the meteor. By analysing the light curve and debiasing the measured magnitudes, the mass ablated - and for small meteoroids the mass ablated is the entire mass of the meteoroid - can be calculated. The biases and sensitivities of a detector determine its usefulness. The sensitive range of electro-optical detectors is determined by the limiting sensitivity and the limit of saturation.

The limiting sensitivity represents the lower limit of detection. Often the limiting stellar sensitivity is quoted, though the limiting meteor magnitude may be up to five magnitudes brighter because of the shorter dwell time of a moving source (Hawkes & Jones, 1986). Hawkes and Jones (1986) point out three major factors limiting the sensitivity of any electro-optical detector. Firstly, there exists a quantitative limit to the detector for the minimum number of photons per integration time for which an observation can be made, related to the quantum efficiency (Soule, 1968). The quantum efficiency of electro-optical devices describes the ability of a detector to convert incident photons to an electrical signal. Typical, modern electro-optical devices have a 60% quantum efficiency which is roughly thirty times that of photographic plates (Howell, 2000). Secondly, the meteor must be distinguishable from the background illumination. The background illumination in a ground based observation originates from unresolved stellar sources (faint stars which are cannot be

resolved), atmospheric effects, and miscellaneous sources such as light from man-made sources. Thirdly, the meteor must be bright enough to be noticed above the electronic noise of the system. Modern CCDs are almost noise free, and thermal noise in the intensifier is small when averaged over one field; in this study the effect of noise is negligible relative to the detection limits. For this study, the limiting sensitivities were dominated by the background illumination.

The upper limit of the sensitivity range is determined by saturation. In CCDs incident photons are converted to an electrical charge collected by the pixels; however, each pixel can only contain a finite amount of charge and very bright objects will produce an excess of charge that cannot be collected by the pixels. The finite charge capacity of a pixel is called its 'full well capacity', and when this limit is reached it is said to be saturated and will collect no further charge (Howell, 2000). CCDs enter a non-linear region near the full well capacity of a pixel, and the electronic response to photons starts to decrease. In the intensified video system used, the image intensifiers saturate first avoiding the non-linear region of the CCDs and the CCDs themselves only saturate for very bright meteors. Because data has been truncated when the full well capacity of a pixel is reached, no simple correction is available to account for the truncated light. For saturated meteors we were only able to calculate a lower limit for the mass of the meteoroid.

In addition to saturation there are two related effects: blooming and bleeding. Blooming and bleeding are similar in that both effects are the result of charge overflow from one pixel to adjacent pixels, blooming describes overflow in all directions and bleeding is directed mainly along a line of pixels. The effects of

blooming in the video system used in this study result mainly from the image intensifiers while the rare bleeding observed in some meteors occurred in the CCD. Fortunately, blooming and bleeding can be accounted for by measuring the light in the affected pixels (Duffy & Hawkes & Jones, 1988).

Measuring and debiasing the light curve of a meteor is accomplished in several steps repeated for each frame of the meteor. First, a correction was applied to account for the varied sensitivity across the pixels of the CCD. Howell (2000) describes *flat fielding* as a technique that can be used to determine the correction for non-uniform sensitivity. For each night of observation, the current study obtained spatially offset images throughout the night, due to the time difference between the images and diurnal motion. The offset images were then median filtered the images to remove the stars present in the images throughout the night. Each image frame was then divided by the flat field image to correct the image.

Second, the meteor trail was identified in the flat field corrected image, and the values of the pixels were calculated by subtracting the average value of the background illumination. Because the duration of a meteor is only a few seconds, no obvious shift in stellar positions is recorded, and the background subtraction can be carried out by subtracting the average of all frames containing the meteor, also called the stacked image. Hawkes et al (1993) define a parameter to represent the logarithm of the sum of light detected in the meteor trail as:

$$\psi = \log \sum_i (p_i - \bar{b}) \qquad (2.19)$$

In which $p_i$ is the intensity value of each pixel belonging to the meteor and $\bar{b}$ is the mean intensity of the background areas near the meteor. For the purposes of

this study $p_i$ - $\bar{b}$ is calculated automatically by the analysis software, Photom. Instead of using an average local background area near the meteor (Hawkes et al, 1993), the frames for the duration of the meteor are median combined and the result is subtracted from each meteor frame before the pixel values are summed. The subtraction removes all background light from the frame including light from stars leaving only the meteor light. Because of the fluctuations in the light detected from stars in each frame, frames in which the meteor passed in front of stars could have error in the pixel sum. Points were omitted from the light curve because this error could not be differentiated from meteor light. The parameter $\psi$ can be fitted to apparent visual magnitude by (Hawkes et al, 1993):

$$M_a = a_0 + a_1\psi + a_2\psi^2 \qquad (2.20)$$

The constants of the quadratic for apparent magnitude were calculated by fitting reference stars from the frame with their magnitudes from the Sky2000v4 stellar catalogue. The fit parameters were calculated in "Photom" using stars from the astrometric fit. Star magnitudes were calculated by masking a circle of pixels over the position of the star and a local background was determined by a ring with a slightly larger radius than the circle. Stars were rejected from the fit for several reasons:

I. Saturation; saturated stars yielded underestimated apparent magnitudes

II. Incomplete coverage by the masking circle; underestimates the magnitude due to missed light

III. Other stars in the background ring; overestimates the local background

IV. Extensive shadowing in the masking circle; a Fourier Transform is used to convert photon detection to the CCD output signal and generates artifacts where pixels beside bright stars can have values visibly below local background and this caused underestimation of magnitude.

The Gen III image intensifiers used are sensitive to red wavelengths so stars with spectral class K or M were frequently discarded as outliers because of overestimation of magnitude. The offset parameter $a_o$ between the apparent magnitudes in "Photom" and the catalogue magnitudes was calculated by assuming a slope of unity ($a_1 = 1$ and $a_2 = 0$) when plotting catalogue magnitude against absolute magnitude of the reference stars. This assumption scales the magnitudes in "Photom" to match those of the catalogue. The fit parameters for the photometric plate were then used to scale the apparent magnitude of the meteor intensity.

The apparent magnitudes were range-corrected to 100km to convert the apparent magnitude $M_a$ to absolute magnitude using the range $R$:

$$\mathrm{M_{abs}} = \mathrm{M_a} - 5\log\left(\frac{\mathrm{R}}{100}\right) \qquad (2.21)$$

After obtaining the light curves with absolute magnitudes, light curves from all available cameras were aligned by determining the smallest sum of residuals of the area under the light curve. This alignment is necessary because different cameras begin to measure the meteor at different points, depending on the meteor's position in the common volume and the sensitivity of each camera. A single light curve for the meteor was calculated by taking the error-weighted average of each frame of the light curves. An example of this is shown in Figure 2.3.

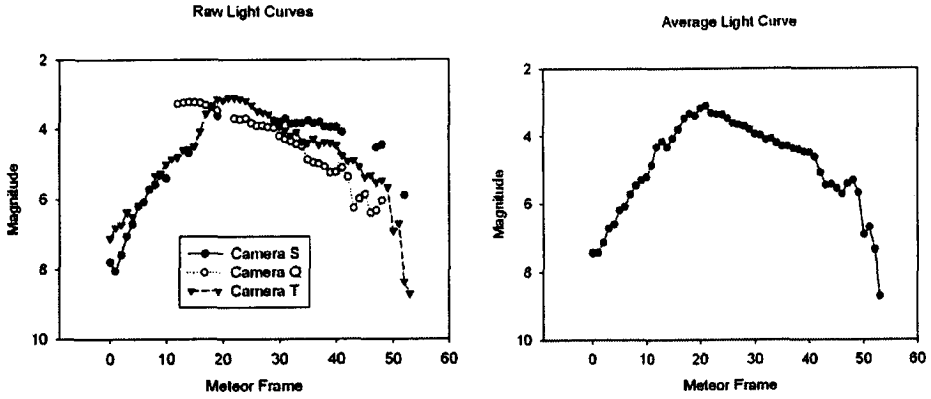


**Figure 2.3: Example of combination of light curves. A meteor observed by all three cameras (left) was averaged point by point weighted with the uncertainty of each point to obtain an average light curve (right).**

The photometric mass was estimated by summing the intensity of light over the entire light curve and converting from luminous energy to lost mass using the luminous efficiency (Hawkes et al, 1993):

$$m_{p_\infty} = \frac{2}{\tau_{op}\, v^4 \cos z} \sum_{i=2}^{f} (H_i - H_{i-1}) 10^{\frac{(M_i + M_{i-1})}{5}} \qquad (2.22)$$

Here $m_{p_\infty}$ was the photometric mass, $v$ was the geocentric speed, which was assumed to be constant over the trail, $z$ was the zenith angle, $\tau_{op}$ was the luminous efficiency, $H_i$ was the height in the $i$th frame, $M_i$ was the absolute magnitude in the $i$th frame, and $f$ was the number of frames.

The optical luminous efficiency, $\tau_{op}$, is the most uncertain quantity involved in calculating the mass of a meteoroid, and is defined as the fraction of meteoroid kinetic energy converted into light during ablation (Ceplecha, 1996):

$$I = -\tau_{op} \frac{v^2}{2} \frac{dm}{dt} \qquad (2.23)$$

Here the intensity $I$ is defined in watts for velocity $v$ in m s$^{-1}$ and mass loss $\frac{dm}{dt}$ in kg s$^{-1}$. The value of luminous efficiency is not well characterized. No available

value has been derived from laboratory work for the average velocity above 47 km $s^{-1}$ (Becker & Friichtenicht, 1971). The luminous efficiency depends on the velocity of the meteoroid and its composition, since different atoms have emission lines at different wavelengths, some of which may fall outside the sensitivity range of the detector. Values for luminous efficiency have been calculated by several authors summarized in Table 2.2. Only the range of photographic luminous efficiencies is listed for Ayers et al (1970) and their values are quoted in cgs units and referenced to a zero magnitude star.

| Author | Method | Values |
|---|---|---|
| Ayers et al (1970) | Observations of artificial iron and nickel meteors. | $1.4 \times 10^{11} - 2.0 \times 10^{12}$ s $erg^{-1}$ 0mag ($\tau_{pg}$) |
| Halliday et al (1981) | Photographic observations of Innisfree meteorite confirmed by recovered fragments | 4% - 8% |
| Ceplecha (1996) | Photographic records combined with modeling confirmed by recovered meteorite fragments. | 6.1% @ v = 13 km/s<br>1.2% @ v = 4 km/s |

**Table 2.2: Luminous efficiencies from previous studies.**

For this study, the values of luminous efficiency were derived ranging from 0.64% at an initial velocity of 80 km/s to 2.3% at an initial velocity of 17 km/s according to the method of Hill et al (2001) described in more detail in Chapter 3. While these values are quite low compared to those listed in Table 2.2, there is currently no conclusive method for calculating the luminous efficiency and the values range over orders of magnitude. The method used in this study was chosen for its basis in laboratory experiments and for compatibility with the development of mass calculations within "Photom".

# 3. Analysis of Data

The meteor flux can be described simply as the number of meteoroids per unit area entering the Earth's atmosphere. Because the observations do not encompass the entire atmosphere the calculation of flux can be described by:

$$\Phi = \frac{n}{At} \tag{3.1}$$

Here the flux is considered because it is the primary value of interest in the study. The division of the number of meteors $n$ by the collecting area $A$ and the time $t$ gives the flux. The mass is also important in order to give reference to the limiting mass for the flux. The mass itself is considered to be a lower limit of the true mass, which cannot currently be calculated primarily due to assumptions involved in the efficiency of the conversion of kinetic energy into observable light. Both mass and collecting area are themselves the product of several calculations.

## 3.1 Mass

The first step in the calculation of meteor mass is to relate light intensity to the decrease in kinetic energy of the ablating mass:

$$I = -\frac{\tau}{2}\frac{dm}{dt}v^2 \tag{3.2}$$

Here, $\tau$ is the fraction of kinetic energy converted to visible light, which is known as the luminous efficiency. Additional kinetic energy may be converted into light outside the visible spectrum by emission lines of some elements. The deceleration of the body is assumed to be negligible so that $v$ represents the initial

speed of the meteor as it enters the atmosphere. Equation 3.2 can be rearranged to solve for the total mass $m$ as follows:

$$m = 2\int_t \frac{I}{\tau v^2} dt + m_e \qquad (3.3)$$

The constant $m_e$ represents the mass at the end of ablation; however, for small meteoroids of the size observable in this study, the residual mass $m_e$ is assumed to be zero for meteors with geocentric speeds greater than 30km $s^{-1}$, because they should have no significant residual mass (Fyfe & Hawkes, 1986). $I$ is the total light intensity emitted by the meteor and all energy loss is assumed to be due to mass loss, because the energy loss due to deceleration has been identified as only significant for meteors with velocities less than 16 km $s^{-1}$ (Ceplecha et al, 1998). These velocities represent only 1.6% of the sporadic meteors observed in this study.

Most of the deceleration for small meteors comes in the last part of the trajectory; the initial observed velocity will be close to the true initial velocity. In order to compute the initial velocity, fluctuations in the solutions for individual cameras were removed by averaging the velocities for the first four points on the trajectory for each station according. The four earliest frames; $j$ = 1 to 4, of the meteor are identified from the alignment of the light curves and for each camera an average velocity, $v_{s,i}$ is calculated over the three subsequent frames for that camera from $i$ to $i+3$, where $i$ is the frame reference for the camera:

$$v_{s,i} = \frac{l_{i+3} - l_i}{t_{i+3} - t_i} \qquad (3.4)$$

Here the velocity is calculated as the length, $l$, along the trail divided by the time, $t$. Then velocities $v_j$ are averaged for all cameras which included the point,

weighted by the sum of squared residuals of the trajectory solution for the station, $ssr_s$.

$$v_j = \frac{\sum_s ssr_s v_{s,i}}{\sum_s ssr_s} \qquad (3.5)$$

The average of the velocities, $v_j$ was deemed the best estimate of the initial speed. Because of the assumption that deceleration is not a source of energy loss the average velocities will be used for the photometric mass calculation.

### 3.1.1 Light Intensity

The light intensity used in equation 3.2 represents all visible light emitted by the meteor. Bronshten (1983) has shown that less than 3% of the visible light emitted is due to atmospheric molecule excitation. Ceplecha et al (1998) claim that more than 90% of meteor light is released by the de-excitation of meteor atoms. Because the current system is predominantly sensitive in the R band of light (approximately 550nm – 850nm), the intensity of the meteor in one video frame is defined based on the observed magnitude for the R band. In order to use the light for calculations of photometric mass, it must be converted from the magnitude scale to a luminous intensity. In order to convert an observed magnitude to intensity, the following equation is defined (Opik, 1955):

$$M_R = 6.8 - 2.5 \log_{10} I \qquad (3.6)$$

Here the absolute magnitude of the meteor, $M_R$, is calculated first by determining the observed magnitude of the meteor within the frame (Hawkes et al, 1993):

$$\psi = \log \sum_i (p_i - b) \qquad (3.7)$$

Where $p_i$ is the intensity value of the pixel and $b$ is the background illumination of the image. For the "Photom" calculation of observed meteor magnitude $M_{obs}$, $\psi$ is calculated as listed above, and $a_o$ is the scaling factor between the light of known stars in the field of view and their catalogue magnitudes as described in Chapter 2:

$$M_{obs} = a_o + \psi \tag{3.8}$$

The observed magnitude is then corrected to the absolute magnitude, the magnitude if the meteor were at a range of 100 km, using Equation 2.21.

In addition to the range correction, three corrections for atmospheric extinction were considered: Rayleigh scattering, ozone absorption, aerosol scattering (Hayes & Latham, 1975). The effects of these corrections are governed by the mass of air through which the light travels, which is approximated by the secant of the zenith angle. Due to the methods of photometric calibration in this study, where light intensity from the meteor is quantified by comparison to stars within a maximum angular separation of 36 degrees, these correction factors are implicitly taken into account. The maximum difference in the correction factor between the calibration stars and the meteor is 0.236 magnitudes, which is on the order of the uncertainty of $M_{obs}$. Consequently, no additional correction for atmospheric effects was made.

### 3.1.2 Luminous efficiency

The luminous efficiency is the most uncertain quantity dealt with in meteor photometry. Several attempts have been made to try to quantify it in the lab, in simulated meteor events (Ayers et al, 1970), and using meteorite dropping events (Ceplecha, 1996). The uncertainty results from the dependence of luminous

efficiency on velocity, chemical composition, shape, and surface area of the meteoroid. In order to maintain consistency with the analysis software "Photom" $\tau$ has been defined using the piecewise method described by Hill et al (2005).

From the definition of the excitation coefficient $\zeta$ (Jones & Halliday, 2001) the luminous efficiency can be derived for an element with mean excitation energy $\varepsilon$, and atomic mass $\mu$.

$$\tau = 2\frac{\varepsilon}{\mu}\frac{\zeta}{v^2} \qquad (3.9)$$

Hill et al (2005) assume a mean value of $\frac{\varepsilon}{\mu} = 7.668 \times 10^6$ J kg$^{-1}$ for meteor spectra and derive the excitation coefficients corresponding to velocity ranges summarized in Table 3.1.

| Velocity Range | Equation of the excitation coefficient | Luminous Efficiency |
|---|---|---|
| $v \leq 20$km/s | $\zeta = -2.1887 \times 10^{-9} v^2 + 4.2903 \times 10^{-13} v^3 - 1.2447 \times 10^{-17} v^4$ | $\tau = -3.3566 \times 10^{-2} + 6.5796 \times 10^{-6} v - 1.9089 \times 10^{-10} v^2$ |
| $20\text{km/s} \leq v \leq 60\text{km/s}$ | $\zeta = 0.01333 v^{1.25}$ | $\tau = 2.044 \times 10^{5} v^{-0.75}$ |
| $60\text{km/s} \leq v \leq 100\text{km/s}$ | $\zeta = -12.835 + 6.7672 \times 10^{-4} v - 1.163076 \times 10^{-8} v^2 + 9.191681 \times 10^{-14} v^3 - 2.7465805 \times 10^{-19} v^4$ | $\tau = -1.9684 \times 10^{8} v^{-2} + 1.0378 \times 10^{4} v^{-1} - 0.1783693 + 1.409636 \times 10^{-6} v - 4.2121559 \times 10^{-12} v^2$ |
| $v \geq 100$km/s | $\zeta = 1.615 + 1.3725 \times 10^{-5} v$ | $\tau = 2.477 \times 10^{7} v^{-2} + 2.1049 \times 10^{2} v^{-1}$ |

**Table 3.1 Velocity dependent excitation coefficients and luminous efficiencies**

Substitution of the excitation coefficients into Equation 3.9 yield the luminous efficiencies used in this study.

### 3.1.3 System Limits

When considering the mass of a meteor, or the masses of a larger number of meteors, several features pertaining to the results are interesting. In order to observe a meteor, it must be brighter than the magnitude limit, a combination of the observing conditions and the sensitivities of the systems. This limiting magnitude of the system gives a smallest mass observable by the system. The mass distribution is in general assumed to follow a power law distribution of the form (Hawkes & Jones, 1975):

$$N_c = Cm^{1-s} \qquad (3.10)$$

Where $N_c$ is the cumulative number of meteors of mass $m$ or greater, $C$ and $s$ are constants, and $s$ is referred to as the mass distribution index. An $s$ value of 2 indicates that the total mass of meteoroids in any mass bin is equal, with the larger number of small mass meteoroids precisely making up for their smaller size. A mass index less than two indicates more mass in larger particles; $s$ greater than two indicates more mass in smaller particles. Showers typically have $s$ less than 2 (Pecinova & Pecina, 2007). The slope of the straight line portion of a plot of the logarithm of $N_c$ against the logarithm of $m$ is equal to $1$-$s$. Figure 3.1 is a logarithmic plot of the mass distribution observed in this study. There is no obvious straight line portion of the curve with which to obtain a constant slope; this is likely due to different populations of sporadic meteors having different mass distribution indices, though this has not been measured. For this study, a value of $s = 2.14 \pm 0.12$, which is in good agreement with the values presented in Hawkes and Jones (1975), was found by taking a line of best fit through the data from $m = 10^{-6}$ kg to $m = 2.5 \times 10^{-5}$ kg. The uncertainty has been taken as the standard error of the slope.

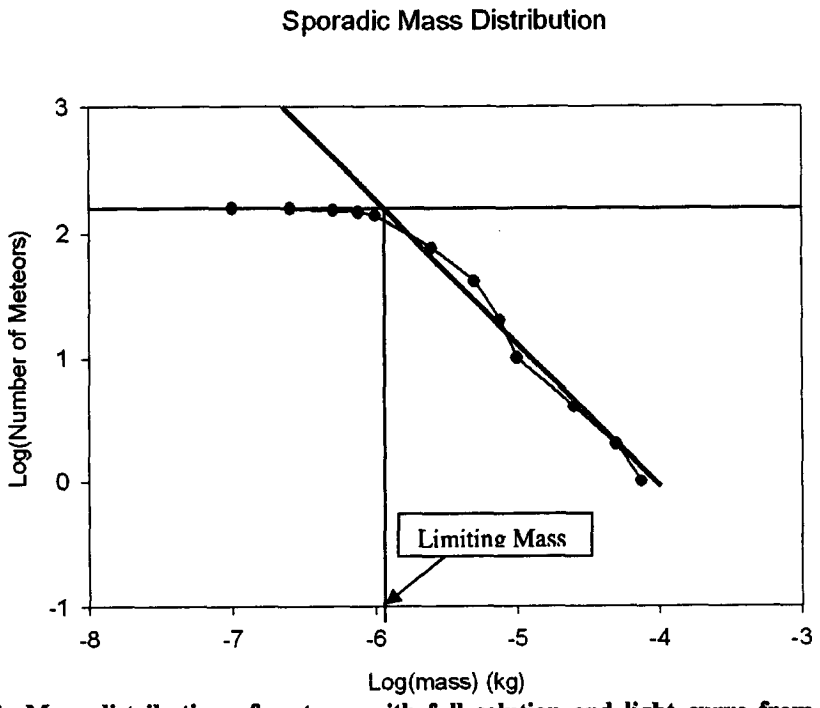


**Figure 3.1: Mass distribution of meteors with full solution and light curve from data (filled circles) and the line of best fit for the slope representing 1-s (solid gray).**

To understand the scope of the results for the flux they must be referenced to a limit of the detectable meteors, the limiting mass. The limiting mass of the system is determined from an extrapolation of the straight line portion (solid gray) of Figure 3.1 and then reading the mass at which all meteors observed in the study are seen. This is a more reliable measure of the limiting mass than choosing the smallest mass seen, because the smallest mass seen depends largely on the geometry and velocity of the meteor and many meteors at the same mass could easily be missed. The limiting mass is the mass at which the number of meteors predicted by the mass distribution index equals the number of meteors observed, and it is based on the assumption that the number of meteors observed below this mass compensates for the number of meteors missed above it. The effective limiting mass for this study is $(1.1 \pm 2.1) \times 10^{-}$

$^{6}$ kg, which is the equivalent mass to which all sporadic meteors would be detected. The uncertainty in the limiting mass was taken from the standard error of the fit parameters in the line of best fit: the y-intercept was - 4.61 ± 0.62, and the slope was - 1.14 ± 0.12. A similar calculation can be performed to obtain a limiting magnitude for the system.

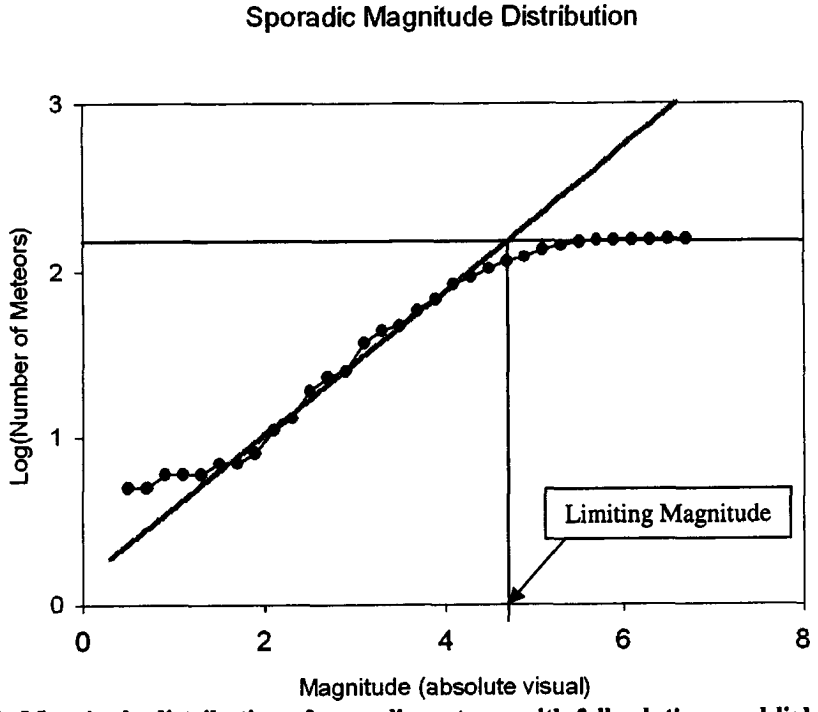


**Figure 3.2: Magnitude distribution of sporadic meteors with full solutions and light curve data (filled circles) and the line of best fit for the straight portion of the plot (solid gray).**

Often quoted for showers, the limiting magnitude is the equivalent magnitude at which all meteors of that magnitude and brighter will be observed by the system. Following the same procedure for determining the limiting mass of the system, an effective limiting magnitude of 4.72 ± 0.19 in absolute visual magnitude was found. The uncertainty is taken from the standard error of the line of best fit: the y-intercept was 0.149 ± 0.046, and the slope was 0.432 ± 0.014.

Another characteristic of the sporadic meteors is the population index $r$ which describes the distribution of meteor magnitudes. It can be determined from the mass distribution index, where $s$ is the mass distribution index and $r$ is the population index for the sample:

$$r = 10^{\frac{s-1}{2.5}} \qquad (3.11)$$

Here $r$ was found to be $2.87 \pm 0.11$ using the mass index value $s = 2.14 \pm 0.12$. Again the value of $r$, much like the value of $s$, may be different for the different sporadic sources, and the numbers of meteors in this study are too few to consider individual source population indices.

## 3.2 Collecting Area

The collecting area is the quantity that changes the observed rate into a flux. If all meteoroids ablated at a single height, and cameras were perfect detectors, the collecting area would simply be the area of the surface at 100 km altitude observed by both cameras in a two-station campaign. In practice, the probability of detection depends on the distance to each camera, the sensitivity of the camera in different parts of the field of view, and the geometry of the meteor relative to the camera. Previously, collecting area and detector sensitivity to meteors have been treated separately (Duffy et al 1988; Brown et al 2002a); however, for the purposes of this study, the collecting area for a particular radiant was calculated in half hour intervals and was weighted by a number of corrections for different aspects of the sensitivity of the system.

First, the volume common to both cameras must be determined. Using a numerical solution an array of points in the common volume is calculated by looking for points in a rectangular grid, with elements 4x4x2 $km^3$, visible to both cameras. To accept a point as detected it must fall between the minimum and maximum azimuth visible for the camera, and the zenith angle must be within the minimum and maximum values tabulated for that azimuth. When a point is detected by both cameras it is added to the common volume.

Again, if meteors occurred at a single altitude and the cameras detected all of them, the collecting area would be a slice through the volume. Instead, we take many slices through the volume at all the heights where meteors reach their maximum luminosity, and calculate their area, taking into account the probability of detection of every point on each slice. We take an average of the slices to find the effective collecting area, weighting for the probability that a meteor will reach maximum luminosity at that slice.

The next step for the collecting area is to calculate the position of a given radiant for the date and time of the observations. The location of a radiant at a specific time can be calculated by converting the date to Julian day and calculating the local mean sidereal time (which gives the direction the observing site is facing relative to the fixed stars), which is done for each half hour time bin in the analysis. The radiant in celestial coordinates is defined by the vector:

$$X_c = \cos\delta\cos\alpha \tag{3.12}$$

$$Y_c = \cos\delta\sin\alpha \tag{3.13}$$

$$Z_c = \sin\delta \tag{3.14}$$

Where $\alpha$ is right ascension and $\delta$ is declination. The local mean sidereal time is used to convert the radiant from celestial coordinates to the local Cartesian coordinates referenced from local east:

$$X = X_c \sin t_l + Y_c \cos t_l \quad (3.15)$$

$$Y = X_c \cos t_l \sin \varphi - Y_c \sin t_l \sin \varphi + Z_c \cos \varphi \quad (3.16)$$

$$Z = X_c \cos t_l \cos \varphi + Y_c \sin t_l \cos \varphi + Z_c \sin \varphi \quad (3.17)$$

Here $t_l$ is the local mean sidereal time and $\varphi$ is the local latitude. The local radiant can now be used to calculate the corresponding collecting area of the system.

Provided the radiant is above the horizon, the collecting area of the system will be non-zero. The effective collecting area for the radiant is calculated as horizontal slices though the common volume of the camera system and weighted by the distribution of heights of maximum luminosity. The distribution of heights of maximum luminosity has been determined empirically from the current data set. The height of maximum luminosity for a meteor is calculated by taking the weighted average of the light curves from each camera and determining the point of maximum luminosity, and then taking a weighted average of the heights for each camera at that point. The light curve points are weighted by their uncertainties, and the heights are weighted by the sum of squared residuals for the trajectory solution in which the height is calculated.

Slices of area are calculated by summing the area of the face (4x4 $km^2$) of each grid element (4x4x2 $km^3$) at the same height in the common volume, and weighting it with the sensitivity of the cameras at that location. The sensitivity of the camera is a combination of the range correction for light and the location of the point

in the field of view. The location of the point in the field of view is important because neither the image intensifier nor the CCD of the camera has a uniform sensitivity across all pixels in the field of view. The lenses do not deliver an even intensity of light across each sensor. Pixels at the edges of the field of view will collect less light than pixels in the centre and will therefore be less sensitive to meteors.

The sensitivity profiles were calculated empirically from the flat field images used on the days for which data was analysed. Flat field images were generated for each camera by taking a frame from each meteor video detected by the camera in a night and then averaging them. Because the stars move across the field of view of the camera through the course of the night, the stars will be removed and the flat field is left as an effective view of the uniformly illuminated sky. The profile equation for each camera is the result of fitting the line profile of the horizontal and vertical centres of the field. The line profiles have been fitted with the equation:

$$I = A_0 + A_1\cos^2(A_2 - x) + A_3\cos^4(A_2 - x) \qquad (3.18)$$

Here $I$ is the intensity value of at pixel $x$ from the centre of the row. As an example, Figure 3.3 shows the surface profile for the flat field image of camera Q on the night of May 6, 2006. The values at the rightmost edge represent an image combination artifact.

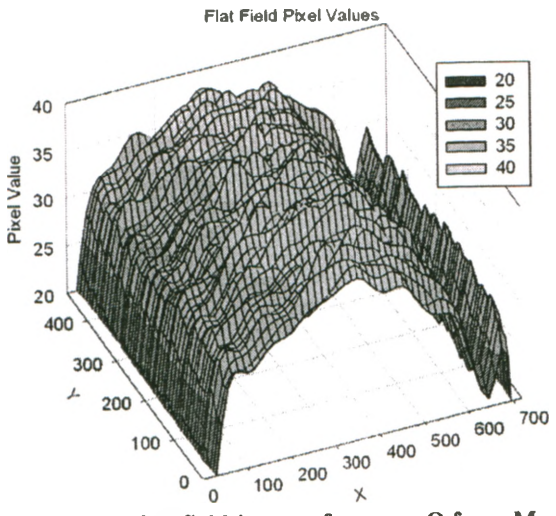


**Figure 3.3: The surface plot of the flat field image of camera Q from May 6, 2006. X and Y are pixel coordinates.**

In order to compute the sensitivity profile, the pixel intensities of individual line profiles taken horizontally and vertically through the flat field images were expressed as a fraction of the maximum intensity for the line. The pixel coordinates were converted to an angular separation from the maximum pixel intensity in the line profile. The data for all line profiles for each camera were combined and fitted according to Equation 3.18 as seen in Figure 3.4. The fit parameters for each camera are listed in Table 3.2 as well as the $R^2$ value of the fit. The sensitivity fits of all vertical line profiles for camera Q indicated that it had uniform sensitivity in the vertical direction. This discrepancy is visible in Figure 3.5 as data deviating from the general trend on each side of the curve. The surface profile of a flat field image of camera S (Figure 3.4) illustrates the sensitivity fall off in both directions. The values at the rightmost edge represent an image combination artifact.

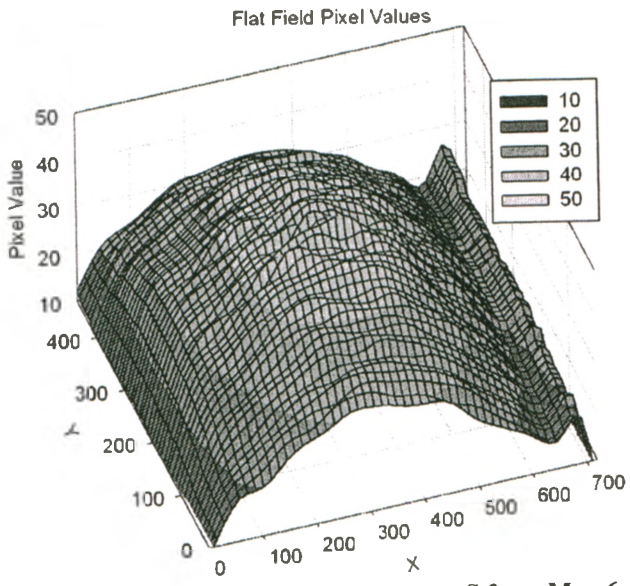


**Figure 3.4: The surface plot of the flat field image of camera S from May 6, 2006. X and Y are pixel coordinates.**

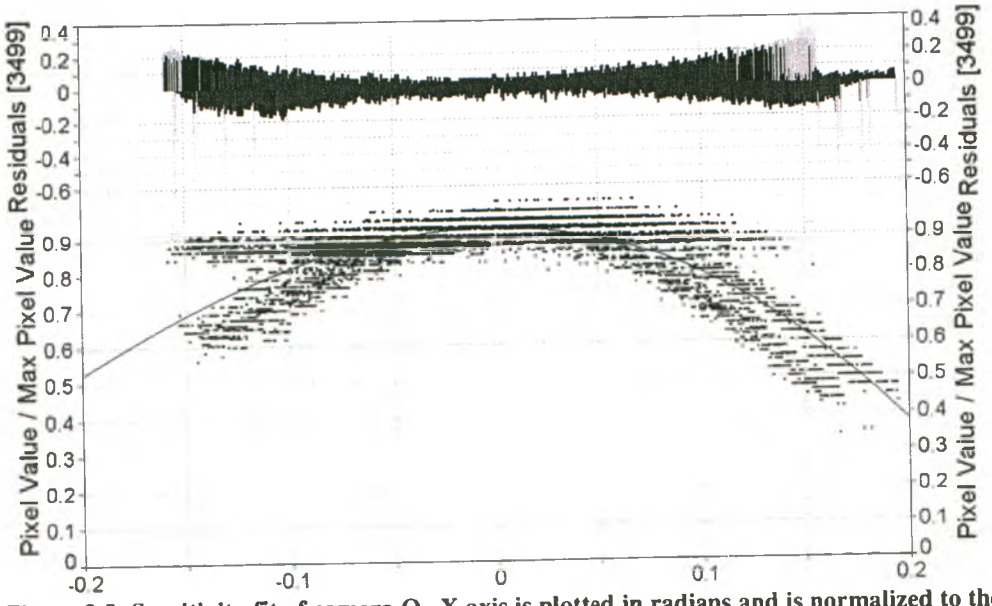


**Figure 3.5: Sensitivity fit of camera Q. X axis is plotted in radians and is normalized to the point of maximum sensitivity for each line profile.**

| Parameter | Camera Q | | Camera S | | Camera T | |
|---|---|---|---|---|---|---|
| | Value | Standard Error | Value | Standard Error | Value | Standard Error |
| $A_0$ | -5.32185 | 0.592421 | -1.69371 | 0.055026 | -0.53029 | 0.03024 |
| $A_0$' (normalized) | -5.2496 | | -1.63161 | | -0.46771 | |
| $A_1$ | 18.72793 | 1.164818 | 8.806192 | 0.122995 | 5.892472 | 0.067199 |
| $A_2$ | 2.52584 | 0.023967 | 0.680259 | 0.004907 | 0.810776 | 0.005305 |
| $A_3$ | -14.0303 | 0.423288 | -7.36618 | 0.053408 | -5.89966 | 0.023175 |
| $r^2$ | 0.675042 | | 0.911687 | | 0.910321 | |

**Table 3.2: Sensitivity fit parameters with standard errors and $r^2$ coefficient for all cameras and nights. $r^2$ is a measure of how well the function fits the data and has a maximum value of 1.0.**

In order to use the sensitivity fit parameters as a weighting factor in the calculation of the effective collecting area they were normalized to a value of 1 resulting in the sensitivity weighting factor:

$$S = A_0' + A_1 * \cos^2(A_2 - \theta) + A_3\cos^4(A_2 - \theta) \qquad (3.19)$$

Here *S* is the predicted value of the sensitivity at an angle $\theta$ from the centre of sensitivity of the camera. Pixel sensitivities for the cameras were generated using Equation 3.19 and the difference between the generated sensitivities and the values of the normalized flat field images from May 6, 2006 was approximately 10% in the centre of the field of view for cameras S and T, and approximately 20% in the centre of the field of view for camera Q. The differences between the normalized flat field pixel values and the generated pixel values was greater closer to the edges of the field of view, and reaching values of approximately 20% for camera S, 25% for camera T, and 35% for camera Q. Part of the reason for the increased disagreement at the edges is due to the fact that the generated sensitivities are based on the average of several

pixel rows which were not necessarily at the centre of maximum sensitivity for each camera.

Because the maximum sensitivity was not aligned perfectly with the coordinate centre of the camera images, corrections had to be made to account for the offset. The offset, both horizontal and vertical, was used to generate a new centre of sensitivity vector to be used in the computation of collecting area.

Additional effects on the sensitivities of the cameras for the detection of meteors arise from the angular velocity and the number of pixels covered by the meteor. The number of pixels covered by the meteor in one frame imposes a firm lower limit to the angular velocities which will be detected. Considering the width in pixels of the brightest stars in the field of view, it was determined that meteors covering less than one pixel would not be detected, because they would appear as dots rather than lines in individual frames. There is also an upper limit to the angular velocity for faint meteors, since the light will be spread over more pixels and may drop below the noise threshold. The number of pixels covered in a frame is dependent upon the velocity of the meteor, $v$, the frame rate of the video system, $F$, the unit vector location of the radiant, ***Rad***, the range from the site to the point, $R$, and the resolution of the camera, $r$.

$$N = 2\frac{\tan^{-1}\left(\frac{v\sin(\cos^{-1}(Pn \bullet Rad))}{2RF}\right)}{r} \qquad (3.20)$$

The argument of the arccosine is the scalar product of ***Pn***, the unit vector from the camera station to the point in the volume, and ***Rad***, the direction of the local radiant. All coordinates in this step are referenced in Earth centred coordinates. The

step is repeated for both cameras. The total sensitivity weight for an element of the common volume is the product of the camera sensitivities for that element.

The total sensitivity weight of an element is calculated by multiplying the sensitivities of each station:

$$A_{sens} = S_1 S_2 \tag{3.21}$$

Where $S_1$ and $S_2$ are the individual sensitivities of the point for each camera calculated using equation 3.19, and the area is calculated as:

$$A = xy\left[\left(\frac{100km}{R_a}\right)^2\left(\frac{100km}{R_b}\right)^2 A_{sens}\cos Z_{av}\right]^{s-1} \tag{3.22}$$

Here $xy$ is the area of the element, $R_a$ and $R_b$ are the ranges in km to the point with respect to each station, $A_{sens}$ is the total sensitivity weight for the point, $Z_{av}$ is the zenith angle, and $s$ is the mass distribution index. The dependence of the sensitivity weighted collecting area on $cos(Z_{av})$ is required, because as the meteor travels at a non-perpendicular trajectory through the atmosphere, the trail is longer than if the meteor were perpendicular to the ground. The light it emits is therefore spread over a longer distance through the atmosphere. As a result of this spreading, the light may fall below the detection threshold of the analysis software, leaving the meteor indistinguishable from the background illumination, so the probability of detection must take into account the $cos(Z_{av})$ term. It is important to remember that this is not the same as the angular velocity correction; it is a result of the light intensity decreasing due to of interactions with the atmosphere. The final collecting area of this horizontal slice is the sum of the weighted area of all elements at the same height calculated using Equation 3.22. The rate at which a less sensitive part of the detector will see meteors depends on the mass distribution index because the number of

meteors missed will be greater if there is more mass in small particles, and fewer will be missed if there is more mass in large particles.

$$\text{Collecting Area} = \sum dh \sum \left( \frac{A_i}{\max A_{sens}^{s-1}} \right) \qquad (3.23)$$

This final effective collecting area now accounts for the height distribution, the sensitivity of the camera system, and the shape and size of the area slices. The height distribution is accounted for by summing all the slices of area and then normalizing.

The effective collecting area will vary based on the declination of the radiant and the mass distribution index. In order to understand the variations in effective collecting area due to these effects several collecting areas were calculated keeping all other variables fixed. The constant variables are listed below:

| | |
|---|---|
| Date | 2006-05-06 |
| Radiant Right Ascension | 336.2° |
| Meteor Velocity | 66 km $s^{-1}$ |

First, the effect of the mass distribution index will be considered. The range of 1.7 to 2.3 for the value of $s$ was chosen as it represents the proposed values of the mass distribution index for sporadic meteors 1.67 (Jones, 1968) to 2.25 (Clifton, 1973). It can be seen in Figure 3.6 that as the mass index $s$ increases, the effective collecting area decreases. The effective collecting area for $s = 1.7$ is approximately 3 times that of $s = 2.3$. We expect that with increasing mass distribution index the effective collecting area will decrease, because as $s$ increases there will be more small meteors which are more easily missed in the less sensitive parts of the field of view.

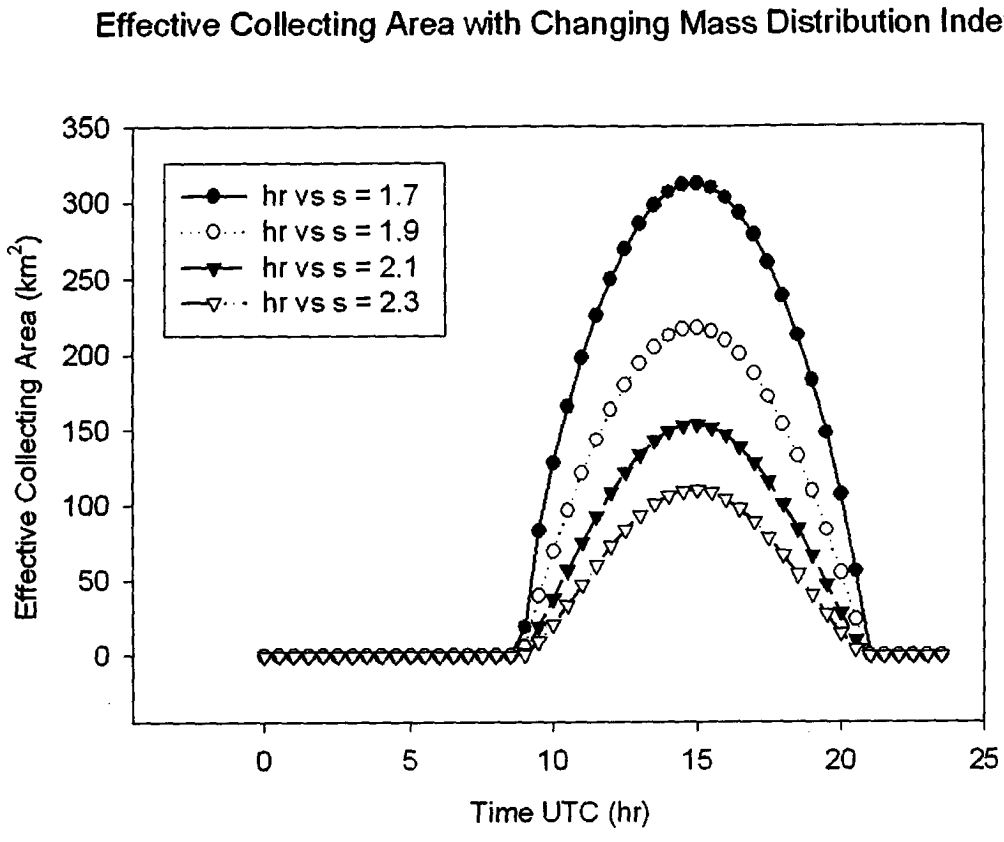


**Figure 3.6: Effective collecting area for s ranging from 1.7 to 2.3**

Second, Figure 3.7 shows the variation of the effective collecting area with declination of the radiant. More structure effects are present because changing declination will affect the geometry of the meteors, and in some instances this will result in meteors travelling towards one station or the other. Because meteors travelling towards a station will have smaller angular width, they will have less chance of being detected and the effective collecting area for the radiant will very quickly decrease. These effects are restricted to times when the radiant passes through or near the field of view of either camera in the system. As the radiant declination decreases, it spends an increasing amount of time below the horizon at which times no meteors from the radiant will be seen and the effective collecting area

is zero. The unchanging effective collecting area for radiants with declination equal to 90° is expected given the pointing direction of the camera system because these radiants will be able to produce meteors that pass through the collecting volume throughout the entire day, with the same relative geometry.

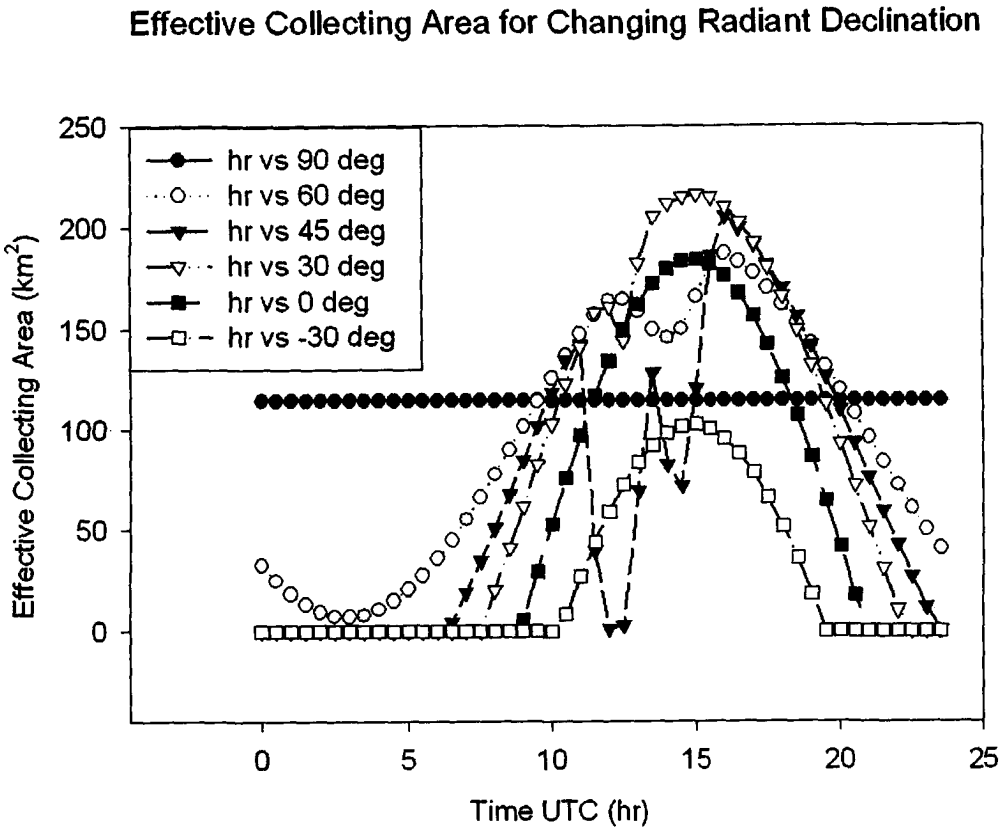


**Figure 3.7: Effective collecting area for radiants with declinations ranging from 90 degrees to -30 degrees.**

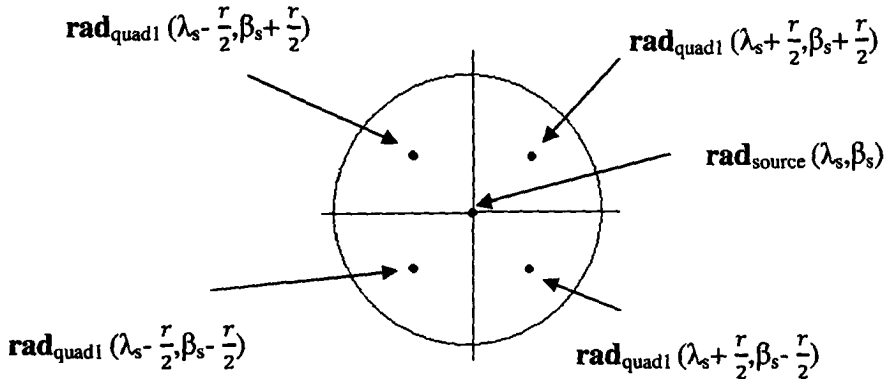


**Figure 3.8: Treatment of sporadic source effective collecting area. Here we show radiants $\mathbf{rad}_x$ and their ecliptic coordinates with r defined as the radius of the sporadic source.**

We can now calculate the flux of meteoroids from a single radiant by calculating the hourly rate, *R*:

$$R = \frac{\Sigma n}{\frac{N}{2}} \tag{3.24}$$

Where *n* is the number of meteors in a bin, and *N* is the number of half hour bins. Here we divide the number of bins by two in order to obtain the number of meteors per hour. Now, R can be divided by the time averaged effective collecting area with *N* time bins and corresponding areas $A_i$:

$$A = \frac{\Sigma A_i}{N} \tag{3.25}$$

And the total flux for a single radiant, $\Phi$ will be:

$$\Phi = 2\,\frac{\Sigma n}{\Sigma A_i} \tag{3.26}$$

In the case of a broad sporadic source, simply increasing the radiant spread in the effective collecting area is not sufficient to determine the flux from a broad sporadic source. Because the effective collecting area software is currently restricted to calculations involving only a single radiant, the effective collecting area of the

sporadic source will remain zero until the centre of the source has risen above the horizon. Even though meteors from the source will begin to appear when the edge of the source rises the collecting area will be zero. To account for the large radius of the sporadic sources each source was divided into four quadrants. The flux for any sporadic source, $\Phi_{sporadic}$, follows Equations 3.24 and 3.25 except that the effective collecting area must now be averaged over the four quadrants as follows where $j = 1$ to 4 for the quadrants and $i = 1$ to $N$ for the number of time bins involved:

$$\Phi_{\text{sporadic}} = R\left(\frac{\Sigma_i \Sigma_j A_{i,j}}{4N}\right)^{-1} \tag{3.27}$$

Because the quadrant radiants are so close, they will have almost the same effective collecting areas. These collecting areas are all roughly the same as the collecting area of the centre of the sporadic source would be and thus produce a collecting area approximately four times the true effective collecting area of the source. The quadrant treatment of the source is a device to account for the earlier rise of the edge and does not scale down the effective collecting areas to a size befitting the smaller portion of the source. The final equation for the flux from a sporadic source is:

$$\Phi_{\text{sporadic}} = 8\frac{\Sigma n}{\Sigma_i \Sigma_j A_{i,j}} \tag{3.28}$$

Ideally, each source would be divided into a large number of small radiants for which fluxes would be individually calculated, but the number of meteors with radiants in each region will become smaller as the areas of the regions become smaller. The flux for a sporadic source was calculated as the sum of the fluxes for each quadrant.

# 4. Results

The data analysis was carried out in several steps using two camera pairings: Camera S and Camera T (both f = 25 mm) at Kitt Peak and Whipple respectively, and Camera S and Camera Q (f = 50 mm, at Whipple). In order to compare the current system to other observations, meteors from the Eta Aquariid shower were identified and separated from the sporadic sample. To compare to visual data, flux values for the Eta Aquariid shower were converted to zenithal hourly rate (ZHR). ZHR is defined as the number of meteors a standard visual observer would see under an unobstructed sky with the radiant directly overhead and a limiting magnitude of +6.5 (Brown & Rendtel, 1996). Once the flux calculation has been tested against other observing methods, velocity and mass distributions of the sample must be determined before the effective collecting area can be calculated for the sporadic meteor sources. Final values of the sporadic meteor flux are calculated for the sample using the effective collecting areas for each visible source.

## 4.1 Eta Aquariids

The Eta Aquariids are a strong meteor shower associated with comet 1P/Halley. The Earth passes through the meteoroid stream between late April and early May with a maximum between May 5$^{th}$ and May 10$^{th}$. The radiant is visible predominantly in the southern hemisphere. Since the radiant is below the ecliptic Eta Aquariid meteors are hardly observable from northern latitudes, especially those greater than 45° N (Rendtel, 1997). The radiant rises shortly before dawn leaving only a few hours for optical observations (Dubietis, 2003; Rendtel, 1997). The

International Meteor Organization lists the following for the Eta Aquariid shower in 2006 (McBeath, 2006):

| | |
|---|---|
| Active | Apr 19 – May 28 |
| Maximum Activity | May 6 |
| $\lambda$ | 45.5° |
| $\alpha$ | 338° |
| $\delta$ | -0.1° |
| $V_{initial}$ | 66 km/s |
| r | 2.4 |
| ZHR | 60 meteors/hr |

**Table 4.1: Eta Aquariid parameters as defined by the IMO**

Here $\lambda$ is the solar longitude at maximum shower activity; $\alpha$ and $\delta$ are the right ascension and declination of the radiant, $v_{initial}$ is the pre-atmospheric speed, $r$ the population index (relating the number of meteors in bins of magnitude) and *ZHR* the zenithal hourly rate at the shower maximum. The radiant drifts from day to day because of the motion of the Earth; for our analysis, this was calculated from the radar shower data in Brown et al (2008).

In order to calculate the ZHR of the Eta Aquariid shower from the sample, the flux as seen by the camera system must be calculated. The effective collecting area was calculated for both nights using the values listed in Table 4.2.

| | 2006-04-27 | 2006-05-06 |
|---|---|---|
| Radiant Right Ascension | 330.3° | 336.2° |
| Radiant Declination | -3.7° | -0.9° |
| Meteor Speed | 66.0 km $s^{-1}$ | 66.0 km $s^{-1}$ |
| Mass Distribution Index | 1.72 | 1.72 |

**Table 4.2: Effective Collecting Area Parameters for the Eta Aquariid meteor shower for the nights of April 27, 2006 and May 6, 2006**

A mass index of 1.72 was used for the Eta Aquariid shower based on the studies of Rendtel (1997) and Hughes (1987). Figures 4.1 and 4.2 show the effective collecting areas for both nights of data for both ST and SQ camera pairings.

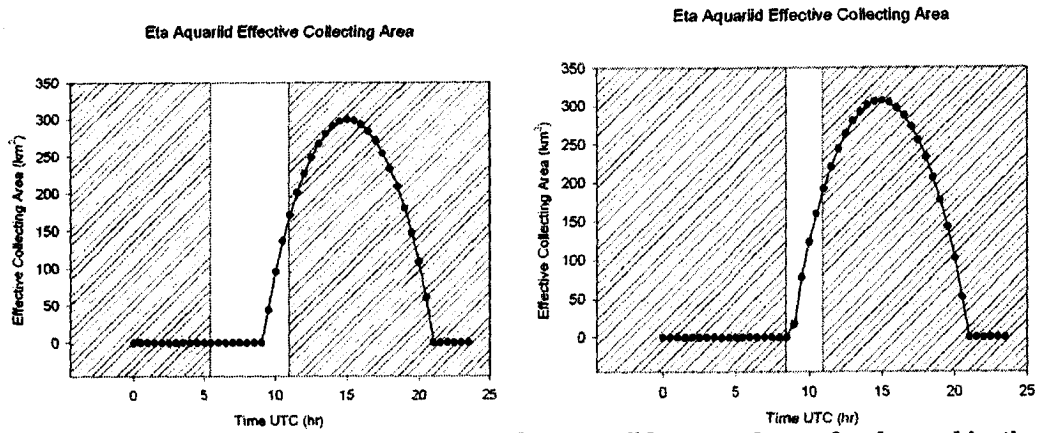


**Figure 4.1: The effective collecting area of the Eta-Aquariid meteor shower for the combination of camera S and camera T for the nights of April 27, 2006 (left) and May 6, 2006 (right). Shaded areas indicate unobserved time.**

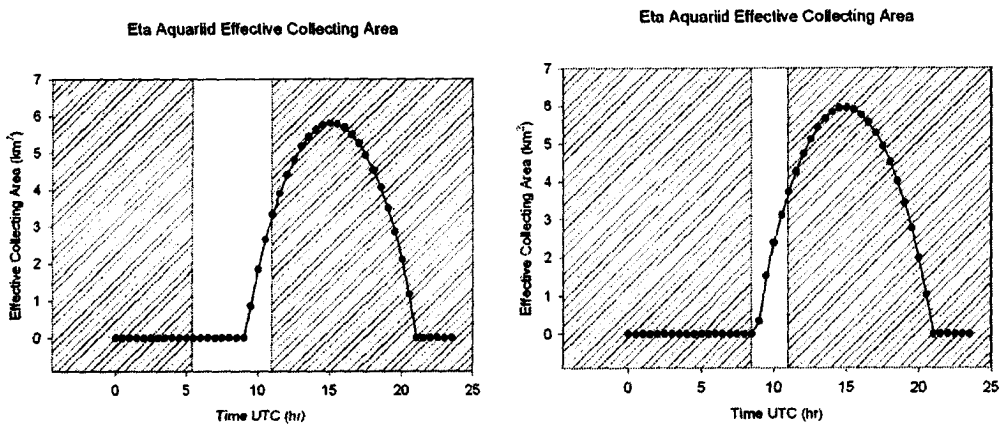


**Figure 4.2: The effective collecting area of the Eta Aquariid meteor shower for the combination of camera S and camera Q for the nights of April 27, 2006 (left) and May 6, 2006 (right). Shaded areas indicate unobserved times.**

While there is very little difference in collecting area for each camera pairing between observing nights, there is a significant difference in the collecting area between the pairings. The camera S and camera T pairing has an effective collecting area roughly fifty times greater than that of the camera S and camera Q pairing, at this time the reason for this discrepancy is not understood and it remains a goal for future research. Because the locations are the same for both camera pairings, the radiant rises at the same time for both. The radiant does not pass close enough to the field of

view to disrupt the effective collecting area by geometrically decreasing the sensitivity of either station. Because of this anomalous value of collecting area for the camera S and camera Q pairing and the unusual apparently uniform vertical sensitivity of camera Q, further analysis will only be carried out using cameras S and T. Solutions and light curve values will remain enhanced by the higher resolution values from camera Q.

A total of 11 meteors were accepted as Eta Aquariids (Table 4.3) within 5° of the radiant and 10 km $s^{-1}$ of the velocity, this velocity constraint was used to avoid counting sporadic meteors with radiants near the Eta Aquariids. All except 20060506-094911, which was only observed on Cameras S and T, and 20060427-110522, which was observed by cameras S and Q, were observed by all three cameras. The difference between the accepted speed of the Eta Aquariid shower and the observed speed of the meteors is listed in Table 4.3.

| Date-Time | Alpha (°) | Delta (°) | Speed Difference (km $s^{-1}$) |
|---|---|---|---|
| 20060506-094005 | 337 | -0.4 | -4.4 |
| 20060506-094911 | 336.1 | -0.44 | -3.4 |
| 20060506-095134 | 337.01 | -0.27 | -2.4 |
| 20060506-095411 | 337.7 | -0.43 | -5.4 |
| 20060506-102059 | 338.5 | -1 | -5.4 |
| 20060506-102422 | 336.2 | 0.22 | -4.4 |
| 20060506-104600 | 339.1 | -1.2 | 0.6 |
| 20060506-111241 | 337.3 | -0.2 | 0.6 |
| 20060506-112511 | 336.9 | 0 | -4.4 |
| 20060427-111042 | 332.1 | -3.8 | -3.4 |
| 20060427-110522 | 330.99 | -3.01 | -5.4 |

**Table 4.3: Observed Eta Aquariid meteors.**

The fluxes computed in half hour intervals. The flux is converted to ZHR by first determining the spatial number density *S*. This can be compared to the spatial number density defined by Brown and Rendtel (1996) based on ZHR:

$$S = \frac{\Phi}{3600v} = \frac{ZHR_{true}}{3600Av} \quad (4.1)$$

Therefore,

$$ZHR_{true} = \Phi A \quad (4.2)$$

Here $\Phi$ [$km^{-2}hr^{-1}$] is the observed flux, $ZHR_{true}$ is the ZHR for a visual observer corrected to a limiting magnitude of +6.5, $A$ is the collecting area for a visual observer and is equal to 34640 $km^2$, and $v$ is the velocity of the meteors in km $s^{-1}$. Here we take $v$ as the known velocity of the Eta Aquariid shower, 66 km $s^{-1}$. Brown and Rendtel (1996) define $A$ as a function of the population index $r$. The collecting area is based on the assumption that the elevation angle of the observer is 50° and that the average height of ablation of a meteor is at 100 km, which implicitly assumes that all meteors seen by a visual observer are in absolute magnitude:

$$A = 37200\,(r - 1.3)^{-0.748} \quad (4.3)$$

$$ZHR_{true} = ZHR_{obs} * C(r) \quad (4.4)$$

$$C(r) = 13.10 * r - 16.45 \quad (4.5)$$

$ZHR_{obs}$ is the uncorrected ZHR, which is desired for comparison with the accepted value listed in Table 4.1, and $C(r)$ is the correction for meteors within an observer's field of view which were not seen (Brown & Rendtel, 1996). Final ZHR values were obtained by calculating the flux from radiant rise until the end of observations and multiplying by $A$. A Poisson distribution was assumed to calculate the uncertainties in meteor detection probability. The Poisson distribution was selected because meteor detections occur as a function of time and the small number of detections for the shower. The error in the sampling rate $\sigma$ is expressed as the square root of the number of meteors $n$ divided by the number of time bins $N$:

$$\sigma = \sqrt{\frac{n}{N}} \tag{4.6}$$

The final $ZHR_{true}$ values were determined to be 214 ± 68 meteors per hour for the night of April 27, 2006, and 972 ± 154 meteors per hour for the night of May 6, 2006. The values of $ZHR_{obs}$ were 14.3 ± 4.5 meteors per hour for April 27$^{th}$, and 65 ± 10 meteors per hour for May 6$^{th}$. The ecliptic longitude for April 27 ranged from 37.7° to 37.9° for the observable part of the night and 14.3 meteors are in good agreement with the value of 12 meteors per hour found by Rendtel (1997) at ecliptic longitude 38.8°. The ecliptic longitude for May 6 ranged from 47.5° to 47.6°, and the $ZHR_{obs}$ of 65 meteors per hour is much higher than Rendtel's (1997) 32 meteors per hour at ecliptic longitude 46.7°; however, the maximum ZHR found by Rendtel was also found 1° ecliptic longitude earlier than expected. The International Meteor Organization (IMO) predicted a maximum ZHR of 60 meteors per hour in 2006 would occur on May 6$^{th}$ (McBeath, 2006) and the $ZHR_{obs}$ calculated here is in agreement with the IMO value. From the good agreement of the Eta Aquariid meteor fluxes with visual data it is clear that the system has no significant unaccounted-for observing bias. The sporadic flux will now be calculated without any further observational bias corrections.

## 4.2 Velocity Distribution

Before a calculation of flux is possible, the velocity distribution or at least a representative velocity is needed in order to compute the sensitivity correction due to angular velocity. Here the initial speed of the meteors has been used to determine the

most common meteor speed to be used in the sensitivity corrections. Figure 4.3 shows a frequency histogram of all sporadic meteors with full solutions.

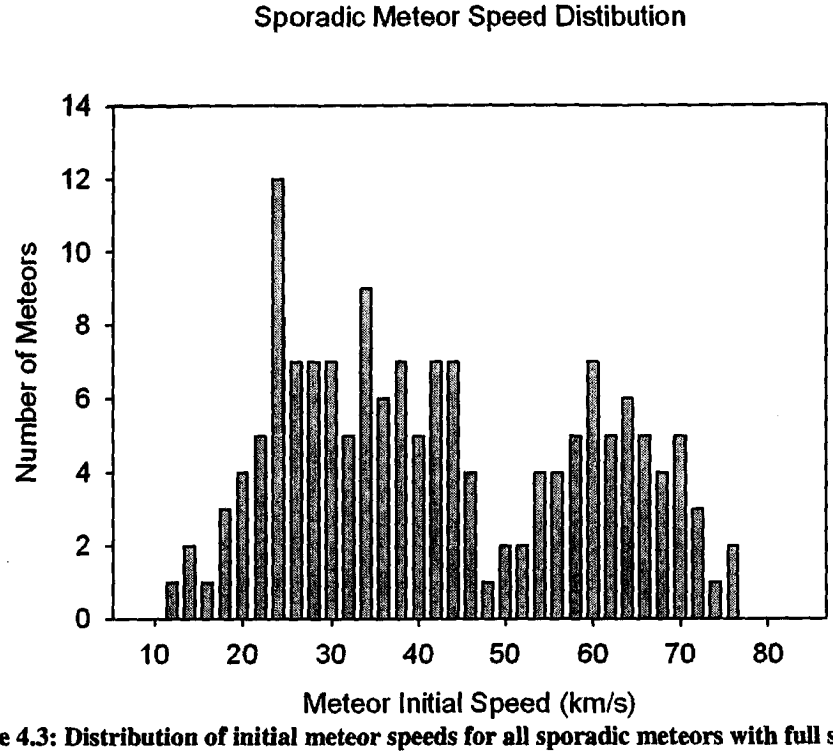


**Figure 4.3: Distribution of initial meteor speeds for all sporadic meteors with full solutions.**

The distribution of speeds has two separate regions, 10 km $s^{-1}$ to 48 km $s^{-1}$ and 50 km $s^{-1}$ to 80 km $s^{-1}$. Several peaks are visible in the sample at 24 km $s^{-1}$, 34 km $s^{-1}$, and a smaller peak at 60 km $s^{-1}$. The velocity distributions of the individual sources are presented in Figure 4.4. In considering the distributions it is appropriate to use different values of most common meteor velocity for different sources (see Table 4.4).

| Source | Velocity (km $s^{-1}$) | Number of Meteors |
|---|---|---|
| antihelion | 28 | 32 |
| north apex (south apex) | 58 | 25(2) |
| north toroidal | 44 | 17 |
| unassigned | 24 | 79 |

**Table 4.4: The most common velocities observed for the sensitivity calculation for each sporadic source.**

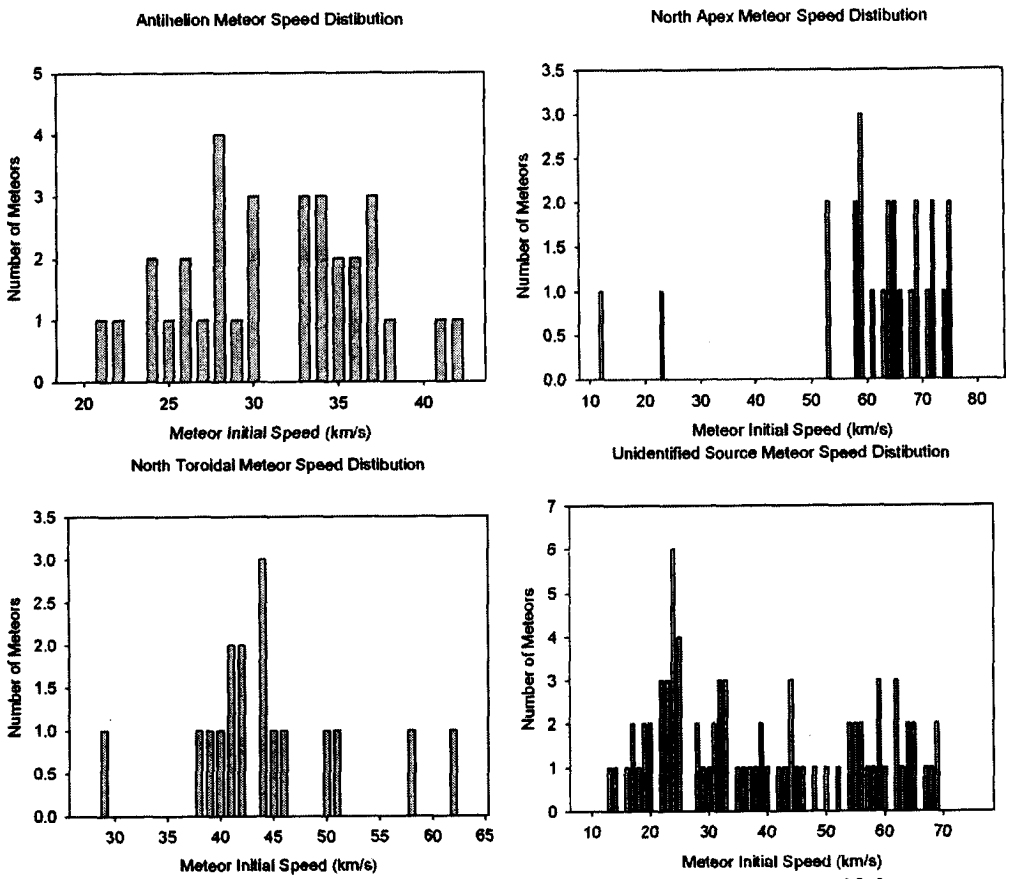


**Figure 4.4: Speed distributions for the antihelion, north apex, and north toroidal sources and the unassigned meteors.**

In light of the high velocities, 67 km $s^{-1}$ and 69 km $s^{-1}$, of the two meteors originating from the south apex source and the symmetry between the north and south apex sources (Chau et al, 2007), the effective collecting area of the south apex source was calculated using the same most common meteor velocity as the north apex source. Because the apex sources are in the direction of the Earth's orbital motion the observed meteor velocities will be a combination of the heliocentric velocities of the meteor and the Earth, and thus are expected to have higher velocities than meteors from other orbits. Using the most common velocities, the effective collecting areas of the sporadic sources can now be calculated.

## 4.3 Sporadic Flux

The sporadic meteor flux is the most important quantity to be calculated in this project. Sporadic meteors dominate the flux of meteoroids at the earth, and measurements are lacking. The flux values are calculated from a small sample of the total number of meteors observed, and all meteors used for flux calculations have full solutions which means they have met the requirements that they were observed by two stations, had convergent trajectory solutions, and the point of maximum luminosity was seen within the field of view at both stations.

While 155 sporadic meteors with full solutions were observed, and 79 meteors were not identified as part of a sporadic source. Flux values can only be calculated for those with well defined sources, because the effective collecting area is calculated for a specific radiant. Of the sporadic sources, meteors were only observed originating from the antihelion, north apex, south apex, and north toroidal sources, as the helion source is not observable at night and the south toroidal source is far below the ecliptic. The sporadic sources have been broken into four quadrants in order to improve the accuracy of the effective collecting area. Unlike shower radiants, sporadic radiants are very broad and the collecting area can differ significantly from one side to another. Because of this, the total fluxes will be calculated as the total number of meteors divided by the time average of the average effective collecting area averaged over all four quadrant sources according to Equation 3.27. Each collecting area was calculated beginning at 0:00 UTC, mass distribution index 2.07, and the appropriate velocity from Table 4.4. The observations occurred between

5:29:26 and 11:33:26 UTC on April 27, 2006 and between 8:49:08 and 11:29:41 UTC on May 6, 2006.

### 4.3.1 The antihelion source

The antihelion source is located nearly opposite the sun on the ecliptic and perpendicular to the Earth's orbital motion at coordinates $\lambda$-$\lambda_o$ = 198° and $\beta$ = 0°. In this study it is numerically the best observed sporadic source with 32 meteors (see Table 4.6). The most common meteor velocity was taken as 28 km $s^{-1}$, which compares favourably with the peak in the velocity distribution of the antihelion source (Campbell-Brown, 2008), for the calculation of effective collecting areas which are plotted in Figure 4.5. As was seen in Figure 3.6 the effective collecting area of Quadrant 4 is lower on May 6 because of the larger negative declination. Additionally, the time that the Quadrant 4 radiant was above the horizon is shorter indicating that it did not achieve an altitude much above the horizon.

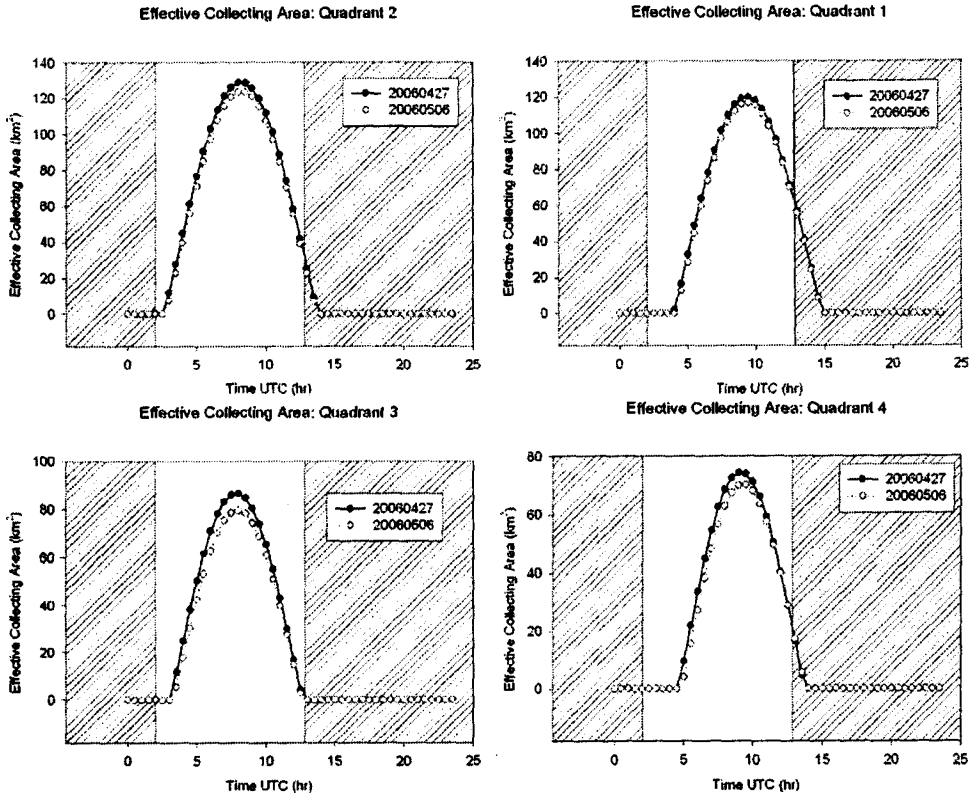


**Figure 4.5: Effective collecting area of the antihelion source separated into four quadrants. Filled circles represent the effective collecting area for April 27 and empty circles represent the data from May 6. Shaded areas indicate daylight.**

| Date | Quadrant | α (°) | δ(°) | Rise (hr UTC) | Set (hr UTC) |
|---|---|---|---|---|---|
| 20060427 | 1 | 244.61 | -12.25 | 4 | 15 |
| 20060427 | 2 | 227.01 | -8.24 | 3 | 14 |
| 20060427 | 3 | 221.61 | -25.49 | 3.5 | 13 |
| 20060427 | 4 | 241.08 | -29.95 | 5 | 14 |
| 20060506 | 1 | 254.34 | -13.61 | 4.5 | 15 |
| 20060506 | 2 | 236.41 | -10.63 | 3 | 14 |
| 20060506 | 3 | 231.93 | -28.13 | 3.5 | 13 |
| 20060506 | 4 | 252.08 | -31.49 | 5 | 14 |

**Table 4.5: Quadrant radiants and rise and set times in UTC.**

| Date-Time | λ (°) | β (°) | Velocity (km $s^{-1}$) | +/- (km $s^{-1}$) | Mass (kg) | Stations | Quadrant |
|---|---|---|---|---|---|---|---|
| 20060427-064653 | 190.79 | -3.29 | 27 | 3.3 | 4.31E-06 | SQT | 1 |
| 20060427-065335 | 184.52 | 2.21 | 38 | 4.8 | 5.35E-06 | SQT | 4 |
| 20060427-065439 | 199.65 | -0.02 | 37 | 4.5 | 2.6E-06 | SQT | 2 |
| 20060427-065955 | 197.1 | -0.33 | 36 | 4 | 1.62E-05 | SQT | 1 |
| 20060427-071908 | 195.1 | 9.49 | 29 | 3.3 | 1.58E-06 | ST | 4 |
| 20060427-072632 | 197.58 | 0.72 | 42 | 3.5 | 3.66E-06 | SQT | 4 |
| 20060427-083057 | 205.19 | 6.48 | 21 | 2.8 | 3.82E-06 | SQT | 3 |
| 20060427-084608 | 200.17 | -1.11 | 25 | 2.2 | 1.7E-06 | QST | 2 |
| 20060427-085429 | 191.2 | 12.11 | 36 | 4.5 | 8.4E-06 | ST | 4 |
| 20060427-085509 | 199.54 | -4.46 | 28 | 3.5 | 1.04E-06 | SQ | 2 |
| 20060427-090730 | 194.34 | 13.34 | 33 | 4 | 3.42E-06 | ST | 4 |
| 20060427-090837 | 213.18 | 8.58 | 35 | 4.3 | 1.74E-06 | ST | 3 |
| 20060427-091730 | 192.11 | 2.94 | 26 | 3.3 | 2.78E-06 | ST | 4 |
| 20060427-093007 | 202.85 | 5.75 | 30 | 3.8 | 1.37E-05 | SQT | 3 |
| 20060427-094519 | 202.25 | 0.71 | 33 | 4 | 2.62E-05 | ST | 3 |
| 20060427-094623 | 192.58 | 9.8 | 30 | 3.5 | 4.31E-06 | ST | 4 |
| 20060427-094932 | 182.46 | -0.83 | 28 | 3.5 | 8.24E-06 | ST | 1 |
| 20060427-100942 | 200.83 | 3.05 | 33 | 4 | 1.56E-06 | SQT | 3 |
| 20060427-101025 | 193.44 | 2.33 | 34 | 4 | 6.12E-06 | ST | 4 |
| 20060427-103715 | 194.2 | 0.41 | 34 | 3.3 | 1.41E-06 | SQT | 4 |
| 20060427-104155 | 194.54 | 2.67 | 28 | 3.5 | 1.93E-06 | SQT | 4 |
| 20060427-105916 | 183.59 | 10.51 | 24 | 2.3 | 3.59E-06 | SQT | 4 |
| 20060427-105947 | 199.72 | 5.55 | 26 | 3.3 | 8.49E-06 | ST | 3 |
| 20060506-085746 | 198.81 | 4.24 | 22 | 2.8 | 5.87E-06 | ST | 3 |
| 20060506-091824 | 197.29 | 2.76 | 35 | 4 | 8.02E-06 | SQT | 4 |
| 20060506-095207 | 193.69 | -0.09 | 34 | 3.3 | 1.1E-06 | ST | 1 |
| 20060506-100804 | 212.94 | 1.21 | 37 | 3.5 | 7.6E-07 | SQT | 3 |
| 20060506-102934 | 201.65 | -0.17 | 24 | 2.8 | 6.15E-06 | TSQ | 2 |
| 20060506-103248 | 213.79 | 7.07 | 37 | 4.5 | 1.54E-06 | ST | 3 |
| 20060506-103946 | 190.99 | 7.59 | 30 | 3.5 | 7.18E-06 | SQT | 4 |
| 20060506-104159 | 186.95 | 3.36 | 28 | 2.8 | 7.07E-06 | TSQ | 4 |
| 20060506-110304 | 204.41 | -13.97 | 41 | 4 | 5.98E-06 | SQT | 2 |

**Table 4.6: Identified antihelion meteors with full solutions.**

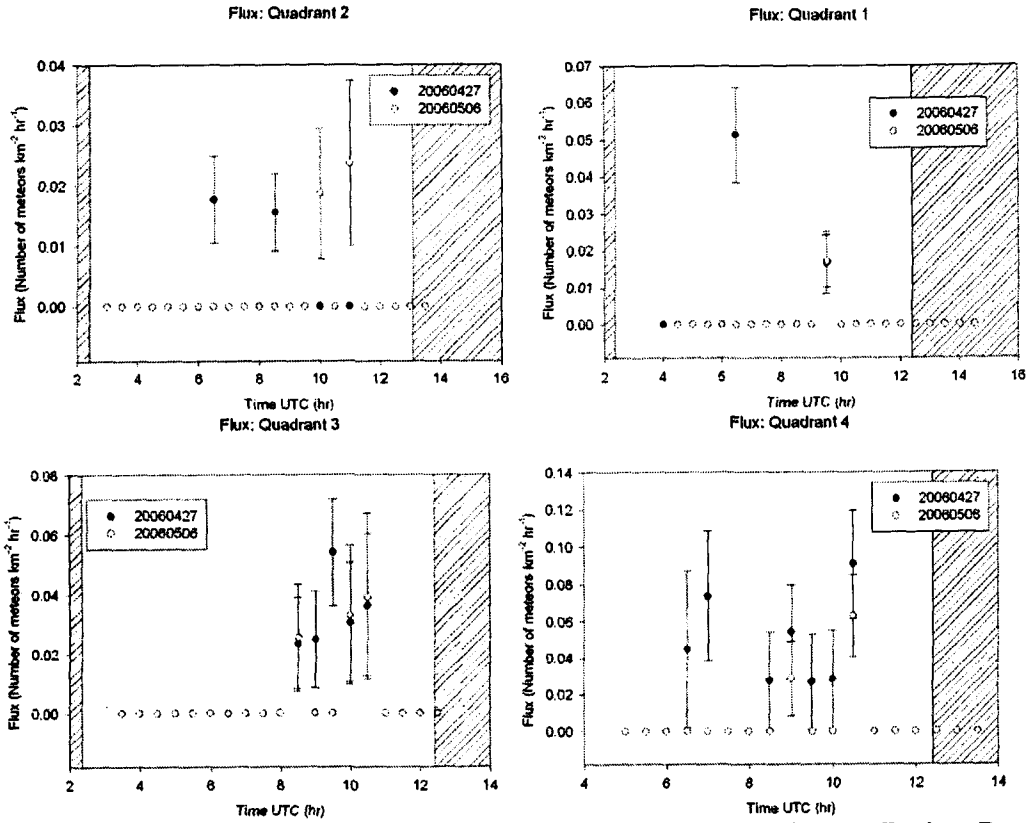


**Figure 4.6: Meteor flux values for the antihelion source for both nights of data collection. Data from April 27 are plotted as filled circles with a solid line and data from May 6 are plotted as empty circles with a dotted line. Shaded areas indicate daylight.**

The individual flux values are calculated by dividing the number of meteors in a half hour bin by the effective collecting area for the bin. The quadrant fluxes are shown in Figure 4.6. The points plotted are only those for times at which the quadrant radiants (see Table 4.5) were above the horizon.

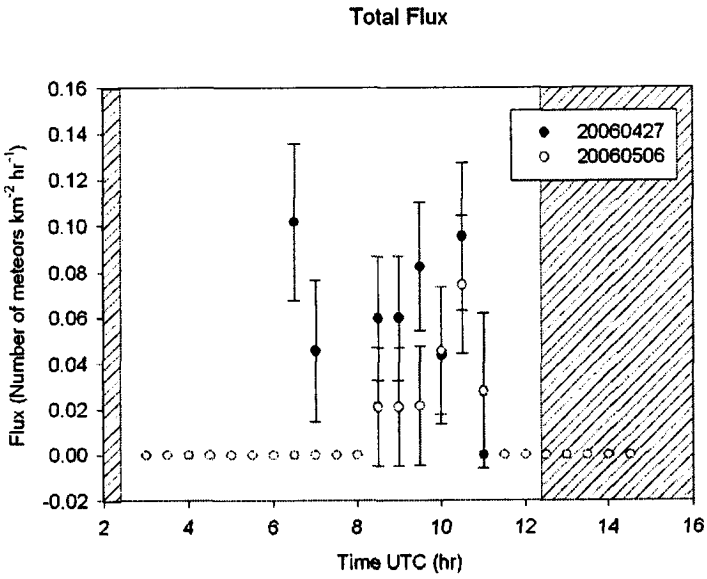


**Figure 4.7: Cumulative flux over all quadrants for the antihelion source. Filled circles represent April 27 data and empty circles represent May 6 data. Shaded areas indicate daylight.**

The cumulative flux curves for both nights are plotted in Figure 4.7. Plot points for the cumulative flux values range from the earliest radiant rise to the latest radiant set times. Peak flux values were measured as: $0.102 \pm 0.034$ meteors $km^{-2}hr^{-1}$ for April 27 between 6:30 and 7:00 UTC, and $0.074 \pm 0.030$ meteors $km^{-2}hr^{-1}$ for May 6 between 10:30 and 11:00 UTC. The uncertainties of these values are the propagation of the sampling uncertainty calculated using Equation 4.6. Because the counts within each bin were small, the uncertainties are quite large. With a larger sample of data these statistical uncertainties will be greatly reduced. The 22 meteors observed on April 27 by Camera S and Camera T produced a total flux of $(42.8 \pm 2.6) \times 10^{-3}$ meteors $km^{-2}hr^{-1}$. The total flux from the 9 meteors observed by Camera S and Camera T on May 6 was $(34.4 \pm 4.7) \times 10^{-3}$ meteors $km^{-2}hr^{-1}$.

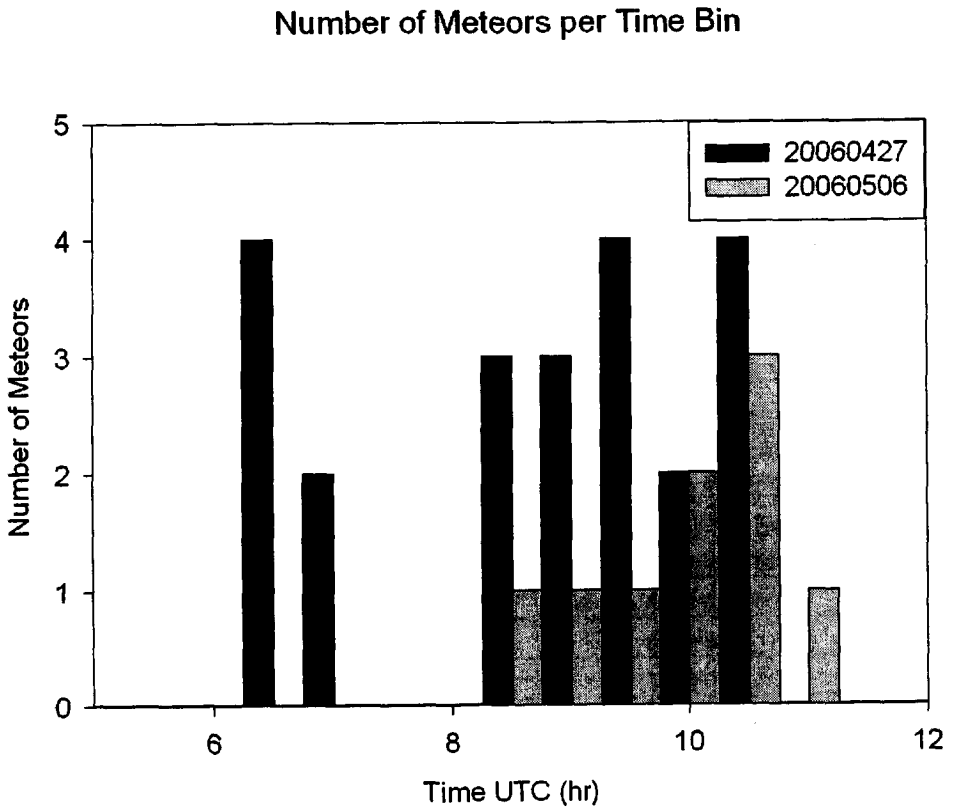


**Figure 4.8: Number of antihelion meteors per time bin.**

To better demonstrate the source of the uncertainties the meteor counts for both nights have been plotted as a histogram (Figure 4.8). The Poisson uncertainties for the statistical fluctuations of the observations in all bins were: ± 1.4 meteors for April 27 observations, and ± 1.2 meteors for May 6 observations. With counts in some bins equal to one this uncertainty is capable of accounting for the lack of observations before 8:00 UTC on May 6.

### 4.3.2 The north apex source

The north apex source is located in the direction of the Earth's orbital motion at the ecliptic coordinates $\lambda$-$\lambda_o$ = 271° and $\beta$ = 19°. This is the second most active source as seen by the current system, consisting of a set of 25 meteors listed in Table 4.7. The most common meteor velocity for the north apex source is 58 km $s^{-1}$ which

is in agreement with Campbell-Brown (2008). The velocities are expected to be higher than those of the antihelion source as these meteors are in the direction of motion of the earth and so will have geocentric velocities which include the orbital speed of the Earth. Quadrant collecting areas for the north apex source are shown in Figure 4.10 for the Quadrant radiants (Table 4.8).

| Date-Time | λ (°) | β (°) | Velocity (km $s^{-1}$) | +/- (km $s^{-1}$) | Mass (kg) | Stations | Quadrant |
|---|---|---|---|---|---|---|---|
| 20060427-082456 | 258.58 | 27.32 | 59 | 7.3 | 1.8E-06 | SQ | 4 |
| 20060427-084157 | 257.88 | 17.99 | 66 | 7.8 | 4.18E-06 | SQT | 1 |
| 20060427-085549 | 258.35 | 25.63 | 59 | 7.5 | 2.2E-06 | SQT | 4 |
| 20060427-090624 | 269.27 | 11.14 | 72 | 8.5 | 4.22E-05 | SQT | 1 |
| 20060427-091326 | 261.72 | 28.31 | 59 | 5.5 | 8.82E-06 | ST | 4 |
| 20060427-095209 | 258.42 | 12.1 | 53 | 6.5 | 3.62E-06 | SQT | 1 |
| 20060427-100556 | 256.06 | 16.55 | 61 | 7.3 | 8.49E-07 | SQ | 1 |
| 20060427-104347 | 260.25 | 22.24 | 63 | 7.8 | 9.54E-06 | ST | 4 |
| 20060427-104556 | 284.39 | 32.69 | 58 | 7 | 6.12E-07 | SQ | 3 |
| 20060427-105416 | 280.22 | 19.39 | 64 | 7.8 | 2.17E-06 | SQ | 3 |
| 20060427-110046 | 263.31 | 15.53 | 75 | 9 | 4.5E-06 | ST | 1 |
| 20060427-112110 | 268.9 | 6.77 | 68 | 8.3 | 4.99E-06 | SQT | 1 |
| 20060427-112124 | 264.49 | 29.11 | 74 | 9 | 9.54E-07 | SQT | 4 |
| 20060427-112351 | 278.07 | 28.2 | 23 | 2.8 | 0.000008 | SQT | 3 |
| 20060427-112815 | 273.83 | 27.76 | 64 | 7.8 | 1.19E-06 | SQT | 3 |
| 20060506-091247 | 281.8 | 21.3 | 53 | 5.5 | 1.4E-06 | SQT | 3 |
| 20060506-100221 | 266 | 26.27 | 12 | 1.4 | 9.04E-06 | ST | 4 |
| 20060506-103050 | 267.22 | 25.43 | 58 | 10 | 4.86E-06 | TSQ | 4 |
| 20060506-103608 | 267.46 | 21.61 | 65 | 6 | 1.12E-06 | SQ | 4 |
| 20060506-105841 | 254.46 | 33.58 | 69 | 8.3 | 8.07E-07 | SQ | 4 |
| 20060506-105856 | 283.78 | 9.6 | 71 | 7 | 1.21E-06 | ST | 2 |
| 20060506-110645 | 260.82 | 7.5 | 75 | 6 | 2.4E-06 | SQT | 1 |
| 20060506-110813 | 277.33 | 15.88 | 72 | 8 | 1.47E-06 | ST | 2 |
| 20060506-110826 | 255.78 | 11.69 | 69 | 6 | 2.94E-06 | TSQ | 1 |
| 20060506-112238 | 264.29 | 33.97 | 65 | 6.3 | 4.96E-07 | SQ | 4 |

**Table 4.7: Identified north apex meteors with full solutions.**

| Date | Quadrant | α (°) | δ (°) | Rise (hr UTC) | Set (hr UTC) |
|---|---|---|---|---|---|
| 20060427 | 1 | -47.28 | 13.09 | 7.5 | 20.5 |
| 20060427 | 2 | -65.26 | 8.47 | 6.5 | 19.5 |
| 20060427 | 3 | -61.24 | -12.15 | 8 | 18.5 |
| 20060427 | 4 | -40.85 | -6.92 | *9 | 20.5 |
| 20060506 | 1 | -39.06 | 15.9 | 7.5 | 20.5 |
| 20060506 | 2 | -56.92 | 10.33 | 6.5 | 19.5 |
| 20060506 | 3 | -51.71 | -10.02 | 7.5 | 19 |
| 20060506 | 4 | -31.73 | -3.81 | 9 | 20.5 |

**Table 4.8: Quadrant radiants and rise and set times in hours UTC.**

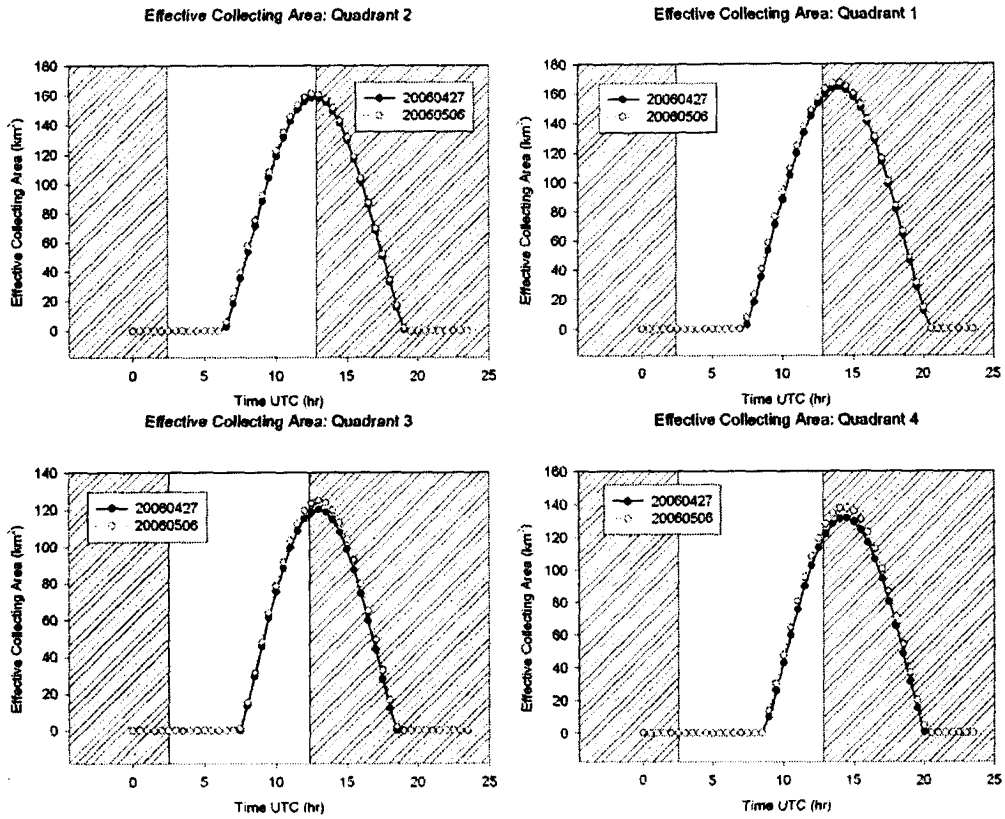


**Figure 4.9: Effective collecting area of the north apex source separated into four quadrants. Filled circles represent the effective collecting area for April 27 and empty circles represent the data from May 6. Shaded areas indicate daylight.**

From Figure 4.9 we see that the north apex source rises several hours after the antihelion source and has a larger effective collecting area, especially for the night of May 6 where the quadrant 4 has roughly twice the effective collecting area at its peak.

The other difference is that the north apex source is up for less observable time than the antihelion source.

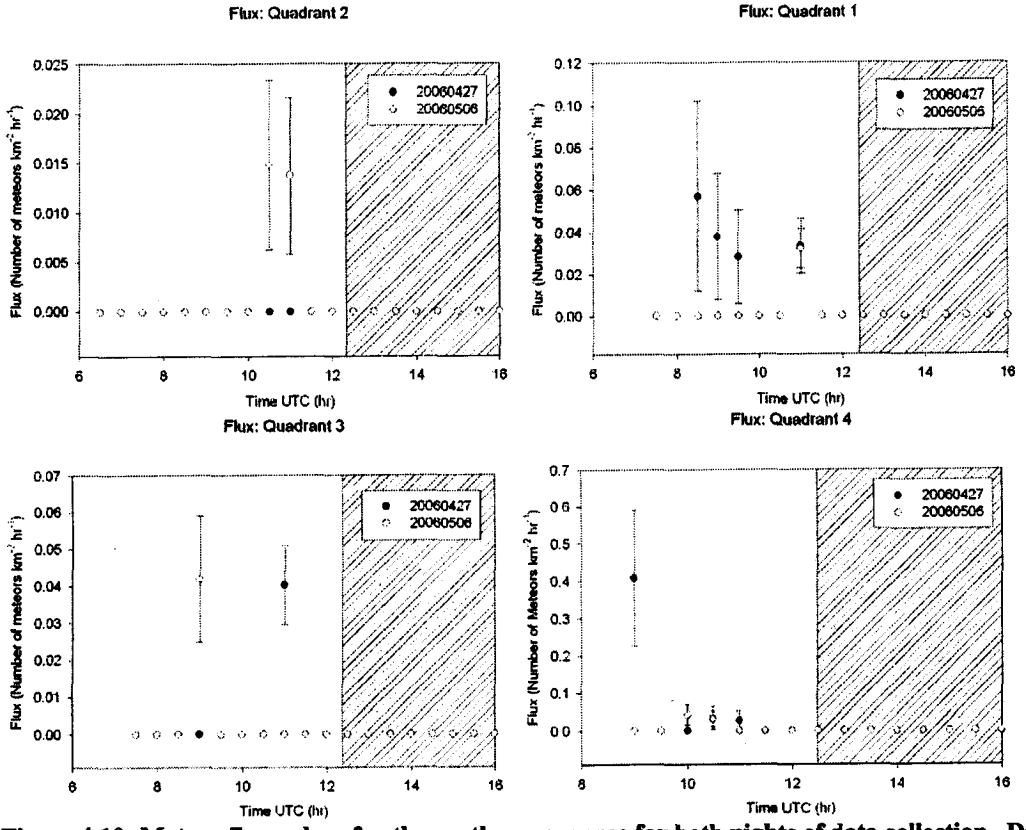


**Figure 4.10: Meteor flux values for the north apex source for both nights of data collection. Data from April 27 are plotted as filled circles with a solid line and data from May 6 are plotted as empty circles with a dotted line. Shaded areas indicate daylight.**

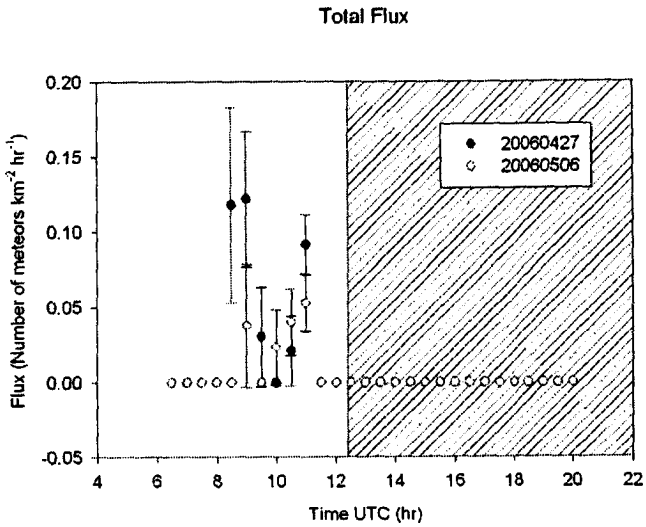


**Figure 4.11: Cumulative meteor flux from the north apex source. Filled circles represent April 27 data and empty circles represent May 6 data. Shaded areas indicate daylight.**

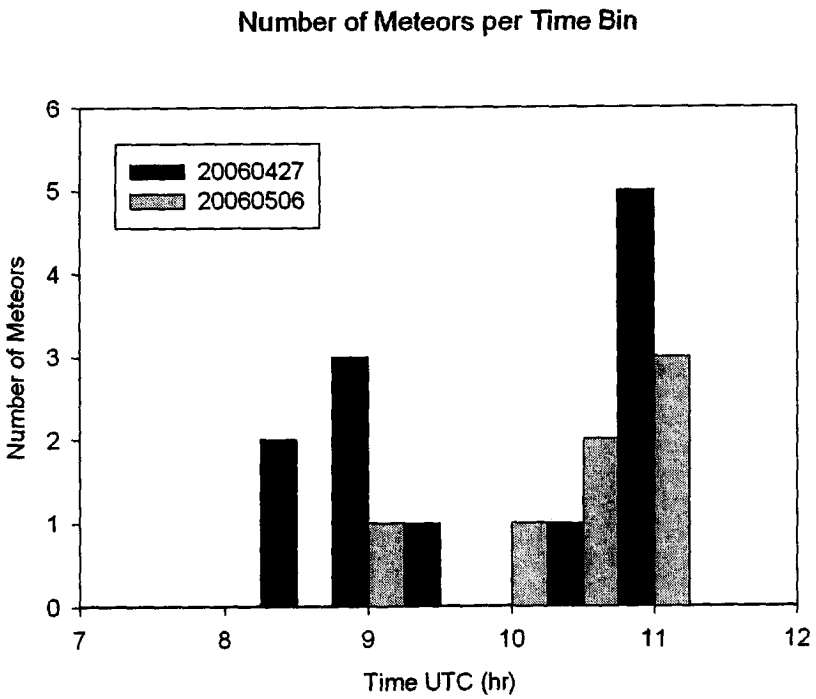


**Figure 4.12: Number of north apex meteors per time bin for both nights of data. Shaded area indicates daylight.**

The quadrant fluxes are shown in Figure 4.10. Points are only plotted for those times at which the quadrant radiants (Table 4.8) were above the horizon. One meteor was present before the first bin in which the radiant in quadrant 4 was active.

Because collecting area is only calculated for a bin if the radiant is above the horizon at the start time of the bin and the meteor time 08:55:49 UTC is so close to the 09:00:00 UTC bin, the meteor was added to the 9:00 UTC bin.

Once again the cumulative flux is plotted for all points from the earliest radiant rise to the latest radiant set and daylight is represented by the shaded portions of the plot (see Figure 4.11). The peak flux value of $0.118 \pm 0.065$ meteors $km^{-2}hr^{-1}$ on April 27 for the north apex source occurred between 8:30 and 9:00 UTC. The peak flux value of $0.053 \pm 0.019$ meteors $km^{-2}hr^{-1}$ on May 6 for the north apex source occurred between 11:00 and 11:30 UTC. The flux for the entire night of April 27 was $(50.9 \pm 4.6) \times 10^{-3}$ meteors $km^{-2}hr^{-1}$ with the uncertainty dominated by the Poisson uncertainty of the observations. The total flux on May 6 was $(30.5 \pm 4.7) \times 10^{-3}$ meteors $km^{-2}hr^{-1}$. Because of the small number of meteors per time bin (see Figure 4.12), the statistical uncertainties are again very large, and with more data these errors will decrease. The Poisson uncertainties for the statistical fluctuations of the observations in all bins were: $\pm$ 1.1 meteors for April 27 observations, and $\pm$ 1.1 meteors for May 6 observations.

### 4.3.3 The south apex source

The south apex source is located below the ecliptic at $\lambda-\lambda_o = 273°$ and $\beta = -11°$. The source is symmetric to the north apex source (Chau et al, 2007). Only two meteors were detected with radiants located within the radiant spread of the south apex source and are listed below (Table 4.9). No flux values have been calculated for this source due to a lack of data. The effective collecting areas have been included for completeness (Figure 4.13); the assumption was made that 58 km $s^{-1}$ would be the

most common meteor velocity because of the symmetry with the north apex source. In the future, these collecting areas can be used to calculate fluxes when more data has been amassed.

| Date-Time | λ (°) | β (°) | Velocity (km $s^{-1}$) | +/- (km $s^{-1}$) | Mass (kg) | Stations | Quadrant |
|---|---|---|---|---|---|---|---|
| 20060506-101453 | 259.5 | -1.86 | 67 | 7.8 | 4.48E-07 | SQ | 4 |
| 20060506-110856 | 275.34 | -6.83 | 69 | 8.5 | 4.27E-06 | ST | 3 |

**Table 4.9: Identified south apex meteors with full solutions.**

The effective collecting areas for quadrants 3 and 4 are low because of the large negative declination of their radiants. Table 4.10 lists the quadrant radiants for the south apex source.

| Date | Quadrant | α (°) | δ (°) | Rise (hr UTC) | Set (hr UTC) |
|---|---|---|---|---|---|
| 20060427 | 1 | -36.05 | -14.84 | 9.5 | 20 |
| 20060427 | 2 | -57.29 | -20.55 | 8.5 | 18.5 |
| 20060427 | 3 | -51.43 | -40.96 | 10 | 17.5 |
| 20060427 | 4 | -28.01 | -34.55 | 11 | 19.5 |
| 20060506 | 1 | -26.68 | -11.55 | 9.5 | 20.5 |
| 20060506 | 2 | -47.31 | -18.2 | 8.5 | 18.5 |
| 20060506 | 3 | -40.24 | -38.27 | 10 | 18 |
| 20060506 | 4 | -18.13 | -31.01 | 11 | 20 |

**Table 4.10: Quadrant radiants for the south apex source.**

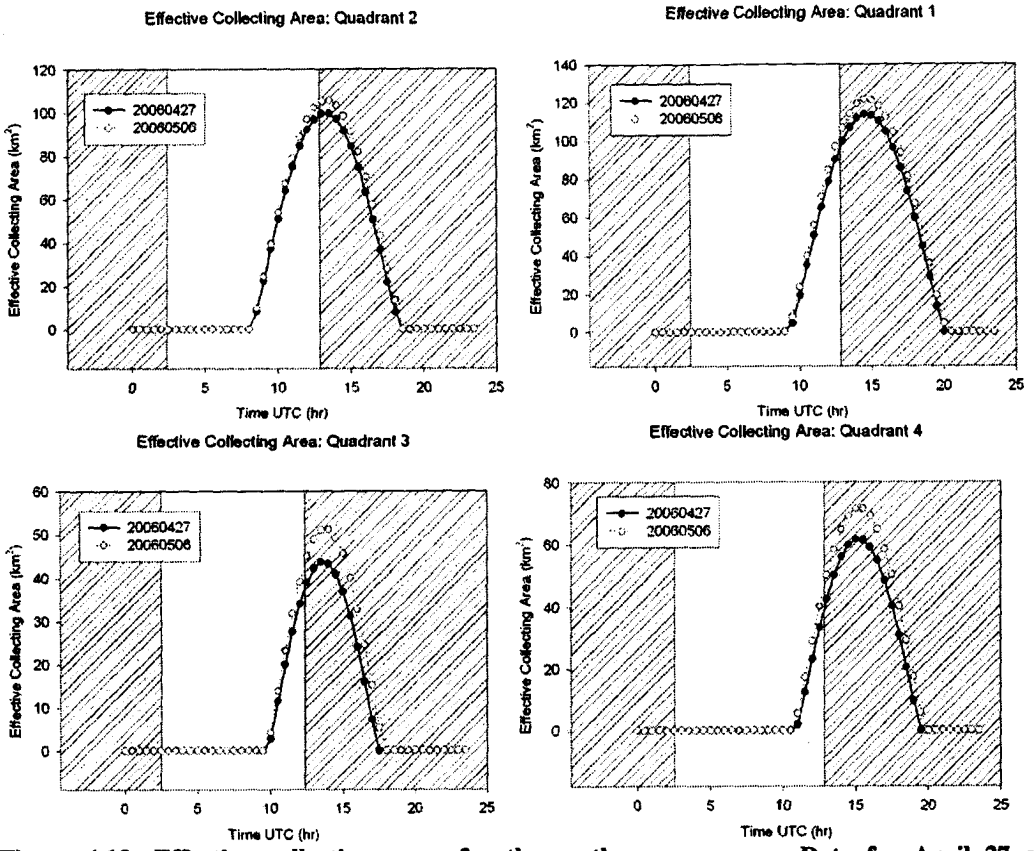


**Figure 4.13: Effective collecting areas for the south apex source. Data for April 27 are represented by the filled circles and data for May 6 are represented by the empty circles. Shaded areas indicate daylight.**

From the quadrant collecting areas, it is observed that the system has a small collecting area for the south apex source for only a couple of hours before dawn. It is worth noting that the shaded areas represent daylight hours based on sunrise and sunset, and that there may be some discrepancy between the times at which dawn occurs and when observations are no longer practical due to background illumination.

### 4.3.4 The north toroidal source

The north toroidal source is located at roughly the same ecliptic longitude as the apex sources, but it has much larger ecliptic latitude: $\lambda-\lambda_\odot = 271°$ and $\beta = 58°$. 17 meteors were observed with radiants within the bounds of the north toroidal source

(see Table 4.11). The most common meteor velocity of the north toroidal source was taken to be 44 km $s^{-1}$ which is in agreement with Campbell-Brown (2008). The effective collecting areas are plotted in Figure 4.14 for the radiants listed in Table 4.12.

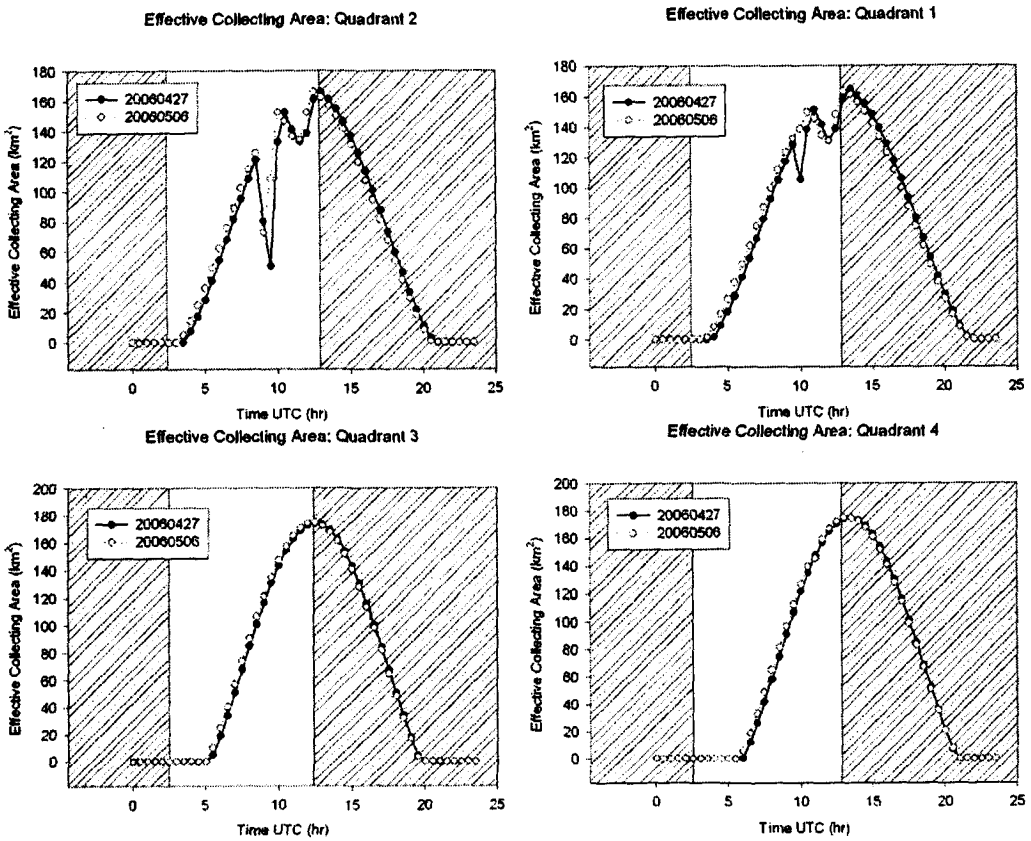


**Figure 4.14: Effective collecting areas for the north toroidal source for both nights of data. Shaded areas indicate daylight.**

The sudden drops in effective collecting area in quadrants 1 and 2 are the result of the radiant entering the field of view of the cameras. This drop in effective collecting area results from a decline in sensitivity of the cameras to meteors from the source near the radiant. This is a geometrical effect because the angular width of the meteor as seen by one camera or the other falls below the angle subtended by one

pixel. When this happens the probability of detection of the meteors and the sensitivity become zero.

| Date-Time | λ (°) | β (°) | Velocity (km $s^{-1}$) | +/- (km $s^{-1}$) | Mass (kg) | Stations | Quadrant |
|---|---|---|---|---|---|---|---|
| 20060427-065540 | 241.3 | 59.2 | 29 | 3.5 | 3.14E-06 | SQT | 4 |
| 20060427-075810 | 292.65 | 62.3 | 42 | 5 | 4.9E-06 | ST | 3 |
| 20060427-084012 | 248.05 | 54.85 | 44 | 5.3 | 2.03E-06 | ST | 1 |
| 20060427-091016 | 259.8 | 59.59 | 51 | 6.3 | 1.42E-06 | SQ | 4 |
| 20060427-091824 | 252.81 | 65.59 | 41 | 5 | 3.85E-06 | ST | 4 |
| 20060427-093557 | 305.49 | 56.18 | 44 | 4.8 | 2.08E-05 | SQT | 2 |
| 20060427-094622 | 258.15 | 43.2 | 45 | 5.5 | 1.96E-06 | SQT | 1 |
| 20060427-103721 | 249.82 | 48.56 | 39 | 4.8 | 8.41E-07 | SQ | 1 |
| 20060427-105531 | 298.01 | 61.2 | 41 | 5 | 6.37E-06 | QST | 3 |
| 20060427-105835 | 295.36 | 53.88 | 44 | 5.5 | 2.09E-05 | SQT | 2 |
| 20060427-110038 | 244.88 | 61.75 | 46 | 5.5 | 2.44E-06 | SQT | 4 |
| 20060427-110643 | 284.43 | 60.99 | 42 | 5 | 1.38E-06 | SQT | 3 |
| 20060427-112606 | 294.83 | 73.65 | 38 | 4.5 | 1.4E-06 | SQ | 3 |
| 20060506-090819 | 263.72 | 39.71 | 62 | 6.5 | 1.08E-06 | ST | 1 |
| 20060506-094652 | 272.39 | 40.38 | 58 | 6.8 | 9.73E-07 | TSQ | 2 |
| 20060506-101436 | 290.35 | 50.43 | 50 | 4.5 | 2.44E-06 | TSQ | 2 |
| 20060506-103206 | 252.74 | 71.43 | 40 | 4.8 | 5.41E-05 | ST | 4 |

**Table 4.11: Meteors detected originating from the north toroidal source.**

Because of the latitude at which the observations were taken and the azimuths of the camera pointing directions, the north toroidal source is visible for almost the entire night. Compared to the north apex source, all radiants for the north toroidal source were above the horizon before the first radiant of the north apex on both nights. Compared to the analysis of sensitivity of varying declinations in Chapter 3, the behavior of the observations of this source is expected.

| Date | Quadrant | α (°) | δ (°) | Rise (hr UTC) | Set (hr UTC) |
|---|---|---|---|---|---|
| 20060427 | 1 | -64.52 | 48.29 | 4 | 22 |
| 20060427 | 2 | -74.41 | 45.64 | 4 | 21 |
| 20060427 | 3 | -68.54 | 27.23 | 5.5 | 20 |
| 20060427 | 4 | -54.77 | 30.81 | 6 | 21 |
| 20060506 | 1 | -59.57 | 50.1 | 3.5 | 22 |
| 20060506 | 2 | -69.34 | 46.84 | 3.5 | 21 |
| 20060506 | 3 | -61.5 | 28.85 | 5.5 | 20 |
| 20060506 | 4 | -47.75 | 33.22 | 6 | 21 |

**Table 4.12: Quadrant radiants and rise and set times in UTC for the north toroidal source.**

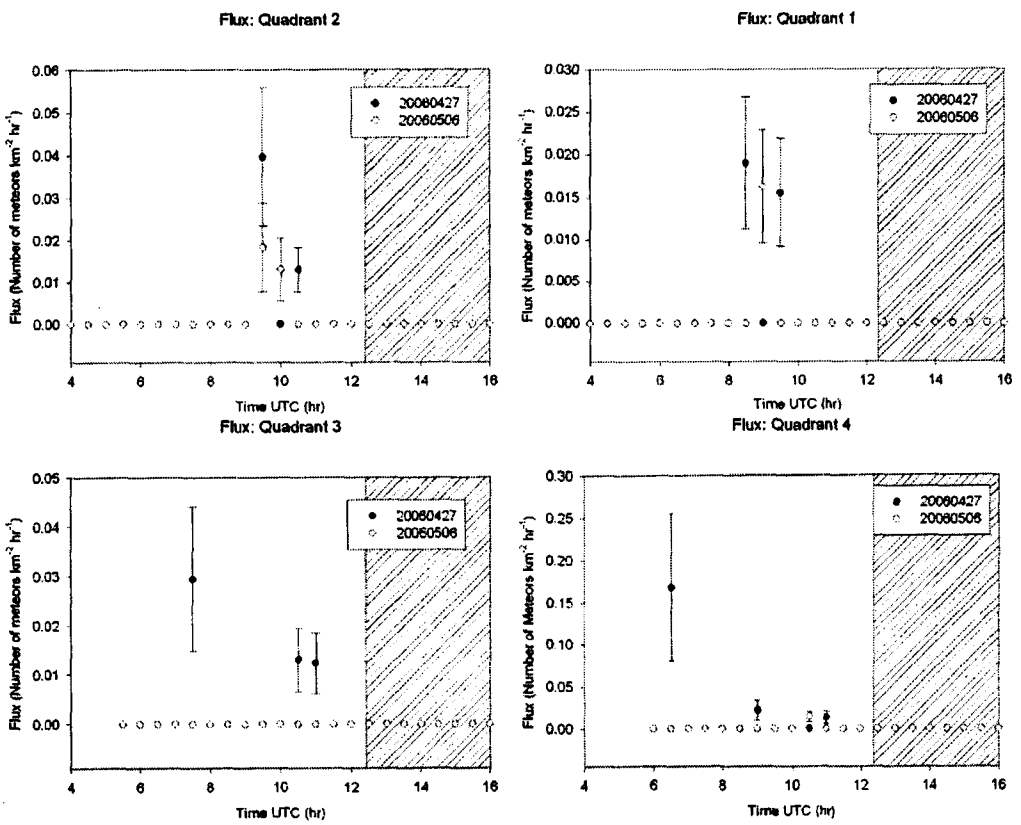


**Figure 4.15: Meteor flux values for the nights of April 27 (filled circles) and May 6 (empty circles) for the north toroidal source. Shaded areas indicate daylight.**

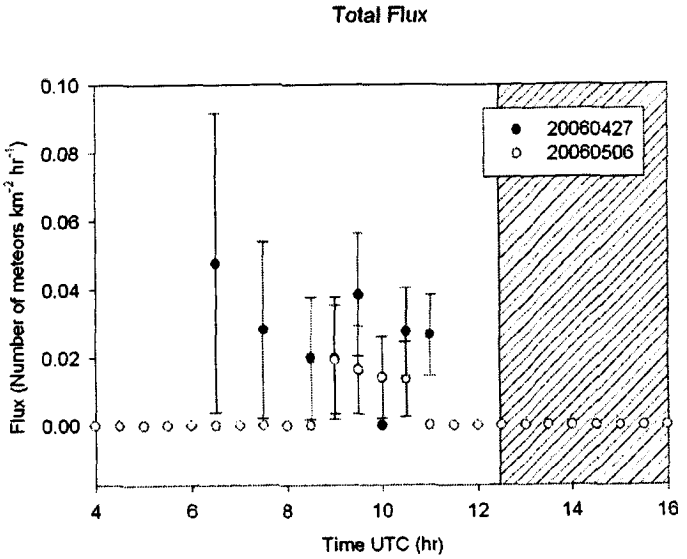


**Figure 4.16: Cumulative meteor flux from the north toroidal source. Data from April 27 are shown as filled circles and data from May 6 are shown as empty circles. Shaded areas represent daylight.**

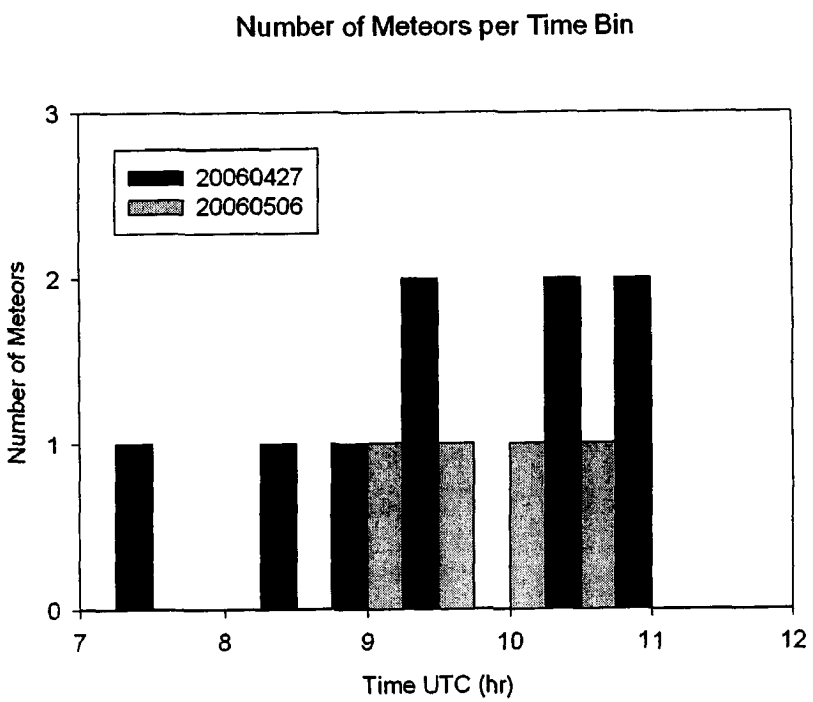


**Figure 4.17: Meteors detected for each time bin from the north toroidal source.**

The cumulative flux for the north toroidal source is plotted for both nights in Figure 4.16. The values are plotted from the earliest radiant rise to latest radiant set.

Peak values of 0.048 ± 0.044 meteors $km^{-2}hr^{-1}$ and 0.019 ± 0.016 meteors $km^{-2}hr^{-1}$ were found between 6:30 UTC and 7:00 UTC on April 27 and 9:00 UTC and 9:30 UTC on May 6 respectively. Total fluxes for each night were: (19.4 ± 1.8) x $10^{-3}$ meteors $km^{-2}hr^{-1}$ on April 27 and (10.4 ± 2.1) x $10^{-3}$ meteors $km^{-2}hr^{-1}$ on May 6. The uncertainties shown in Figure 4.18 are the propagation of the uncertainties derived in Equation 4.6. The counts expressed in Figure 4.17 have associated uncertainties of: ± 0.9 for April 27 and ± 0.8 for May 6.

### 4.3.4 Full night fluxes

While fluxes have been calculated for the individual sources for each night (summarized in Table 4.13), alone they do not give a complete picture of the sporadic flux. Here the nightly flux for each source was doubled, to account for the unobservable sources; helion, south apex, south toroidal, and then the sum of the fluxes are taken as an estimate of the total sporadic flux.

| Source | Number of Meteors (Cameras S and T) | | Peak Flux (meteors $km^{-2}$ $hr^{-1}$) | | Nightly Flux ($10^{-3}$ meteors $km^{-2}$ $hr^{-1}$) | |
|---|---|---|---|---|---|---|
| | Apr 27 | May 6 | Apr 27 | May 6 | Apr 27 | May 6 |
| AH | 22 | 9 | 0.102 ± 0.034 | 0.074 ± 0.030 | 42.8 ± 2.6 | 34.4 ± 4.7 |
| NA | 12 | 7 | 0.118 ± 0.034 | 0.053 ± 0.019 | 50.9 ± 4.6 | 30.5 ± 4.7 |
| NT | 10 | 4 | 0.048 ± 0.044 | 0.019 ± 0.016 | 19.4 ± 1.8 | 10.4 ± 2.1 |

**Table 4.13: Summary of the flux from sporadic sources.**

To an effective limiting mass of (1.1 ± 2.1) x $10^{-6}$ kg and an effective limiting magnitude of 4.72 ± 0.19 absolute visual magnitude, the estimated total sporadic flux was 0.226 ± 0.018 meteors $km^{-2}hr^{-1}$ for April 27 and 0.151 ± 0.023 meteors $km^{-2}hr^{-1}$ for May 6.

# 5. Discussion

The goals of this study were to find the mass distribution index of the sporadic sources, calculate the velocity distributions of the sporadic sources, and estimate the sporadic meteor flux. The calculated values will be compared to other studies designed to test or determine these quantities.

From the sporadic meteors with full solutions presented here, the mass distribution index, s, was determined to be 2.14 ± 0.12. This value is preliminary because there was not enough data to show any clear straight line portion of the mass distribution curve (Figure 3.1) and so a best fit was performed on a portion of the data. This value of s is in agreement with the lower end of the range of sporadic mass indices; 2.048 – 2.363, reported by Hughes and Stephenson (1972) for initial radius corrected radar observations, and is also in agreement with the value 2.02 for an intensified vidicon television system (Hawkes & Jones, 1975). In their study, Hawkes and Jones (1975) compared their results to several other studies and found that they were in good agreement, and so it can be concluded that the current value of 2.14 ± 0.12 is in agreement with previous studies and the mass distribution of the data is in agreement with that represented in the sporadic meteor population.

Campbell-Brown (2008) has presented the orbital distributions of 2.35 million high quality orbits from The Canadian Meteor Orbit Radar (CMOR) operating at 29MHz. Comparing the speed distributions of the current sporadic meteor sample to the full sporadic distribution of Campbell-Brown (2008) is not useful because their data was sampled from five sporadic sources: helion, antihelion, north apex, south apex, and north toroidal, while this study observed only three sources in any

significant numbers: antihelion, north apex, and north toroidal. In order to compare the speed distributions of each individual source appropriately, the current distributions were converted to a number fraction in 1 km $s^{-1}$ bins (Figure 5.1) and were compared to the bias-corrected distributions. Table 5.1 specifies the identifications of the plot symbols in Campbell-Brown's plots in Figure 5.1 (left side). Campbell-Brown (2008) also pairs symmetric sources for orbital parameters so that antihelion and helion sources form one set of data and north and south apex sources are combined into another set, while the third set is solely the north toroidal source.

From the CMOR data the antihelion/helion data set begins at 12 km $s^{-1}$ and ends at 48 km $s^{-1}$ and shows a peak value in the number fraction of 0.05 at a geocentric speed at 28 km $s^{-1}$. While the current set is not as well defined due to the small sample, it does show a peak value in the number fraction of 0.12 at a geocentric speed of 28 km $s^{-1}$. The CMOR distribution is more sharply peaked, although this is almost certainly due to the difference in sample size.

The combined apex sources have a distribution which spans the entire range of possible meteor speeds (12 km $s^{-1}$ – 72 km $s^{-1}$) and two peaks are present in the distribution at 16 km $s^{-1}$ and 58 km $s^{-1}$. The current distribution shows a peak at 58 km $s^{-1}$ which is the same as that observed by CMOR. Two meteors were observed in the apex sample with much lower speeds of 12 km $s^{-1}$ and 23 km $s^{-1}$ which fall within the peak at 16 km $s^{-1}$ from the radar data. The lower speed peak is not clearly represented in Figure 5.1; however, the peak centered on 58 km $s^{-1}$ indicates a

resemblance to the shape in the CMOR data; however, the lack of sample size prohibits a clear match.

Campbell-Brown's north toroidal source shows a clear peak at a geocentric speed of 34 km $s^{-1}$ and a less defined increase in the distribution at 16 km $s^{-1}$. The current north toroidal source shows a peak value at 44 km $s^{-1}$ and trails out to both sides. This peak is at a slightly higher speed than that quoted by Campbell-Brown; however, the higher relative number of meteors just below the peak matches their distribution which falls off slower at lower speeds. While the speed distributions found here might not be in complete agreement with CMOR values their relative shapes indicate that the discrepancies are more likely due to the small sample sizes found here rather than any true differences. The limiting magnitude of CMOR is between +8 M and +9 M (Campbell-Brown & Jones, 2006) so it observes smaller masses than the current system. Because it is possible that different regimes have different distributions, this could also account for some of the differences. A larger sample would be crucial in order to confirm a good agreement between the systems and full consideration to the individual system biases would be necessary to compare the video and radar data.

| Symbol | Helion/Antihelion (top) | Apex Sources (middle) | North Toroidal (bottom) |
|---|---|---|---|
| circle | CMOR helion | CMOR north apex | CMOR |
| triangle | CMOR antihelion | CMOR south apex | HRMP |
| square | AMOR helion | AMOR apex | CMOR corrected |

**Table 5.1: Description of symbols used in speed distribution plots.**

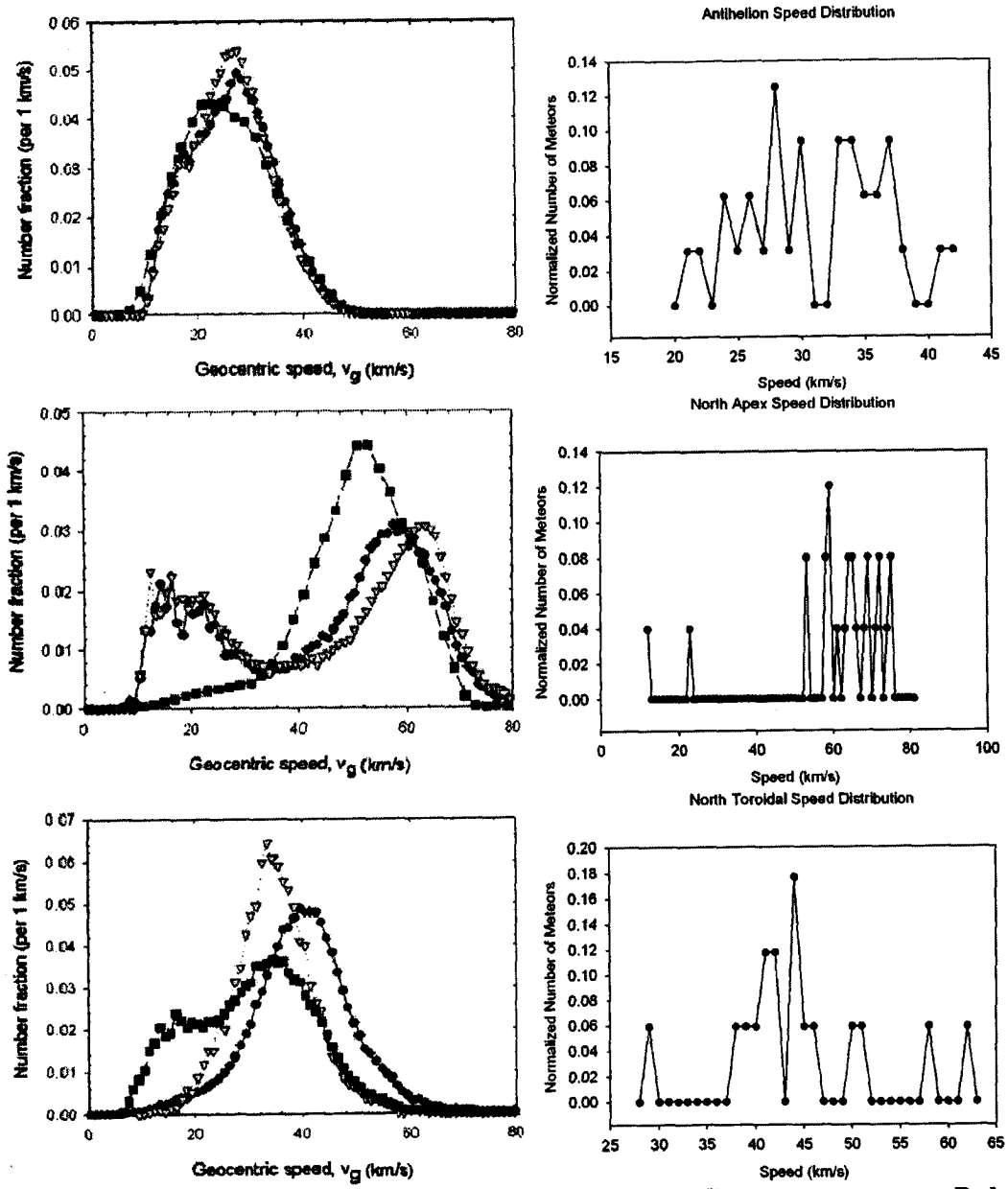


**Figure 5.1: Normalized speed distributions for visible sporadic meteor sources. Radar distributions for paired sources (AH-H, NA-SA, NT is unpaired) from Campbell-Brown (2008) (left) are compared to current distributions (right) for the antihelion (top), north apex (middle), and north toroidal (bottom).**

Nightly sporadic meteor fluxes from the antihelion, north apex, and north toroidal sources were extrapolated by symmetry to encompass all six sporadic sources to give estimated meteor fluxes to an limiting mass of $(1.1 \pm 2.1) \times 10^{-6}$ kg of $0.226 \pm$

0.018 meteors $km^{-2}hr^{-1}$ for April 27 and 0.151 ± 0.023 meteors $km^{-2}hr^{-1}$ for May 6. Because these values are an extrapolation of three sources and a significant number of the meteor solutions observed (half of all sporadic solutions) were not associated with a sporadic source, these values represent lower limits to the sporadic flux. Taking 100 km to be the average ablation height of meteors and assuming Earth is a sphere the estimated lower limit to sporadic meteor fluxes annually are (1.04 ± 0.08) x $10^{12}$ meteors per year from the April 27 value, and (7 ± 1) x $10^{11}$ meteors per year at an effective limiting magnitude of 4.72 ± 0.19. These values are in plotted with the values in Zolensky et al (2006) in Figure 5.2.

For reasons we cannot currently explain, the axes presented in Figure 5.2 do not match both limiting mass and limiting magnitude, and so cumulative flux values are referenced to the limiting magnitude, 4.72 ± 0.19. We suspect that this discrepancy is due to a combination of the differences in meteor speeds and luminous efficiencies used to calculate mass. At the limiting magnitude, the values obtained in this study appear to be reasonable when compared to the other studies, with the exception of Ceplecha (2001). The fluxes may be a bit higher than the expected values; however, it is not a significant difference because of the errors associated with the assumption that the south apex, south toroidal, and helion sources have equivalent fluxes to their counterparts observed in this study.

When compared to the flux curve of Ceplecha (2001), these values overestimate the cumulative numbers hitting the Earth's atmosphere by about two orders of magnitude when compared to the flux from photographic and television meteors.

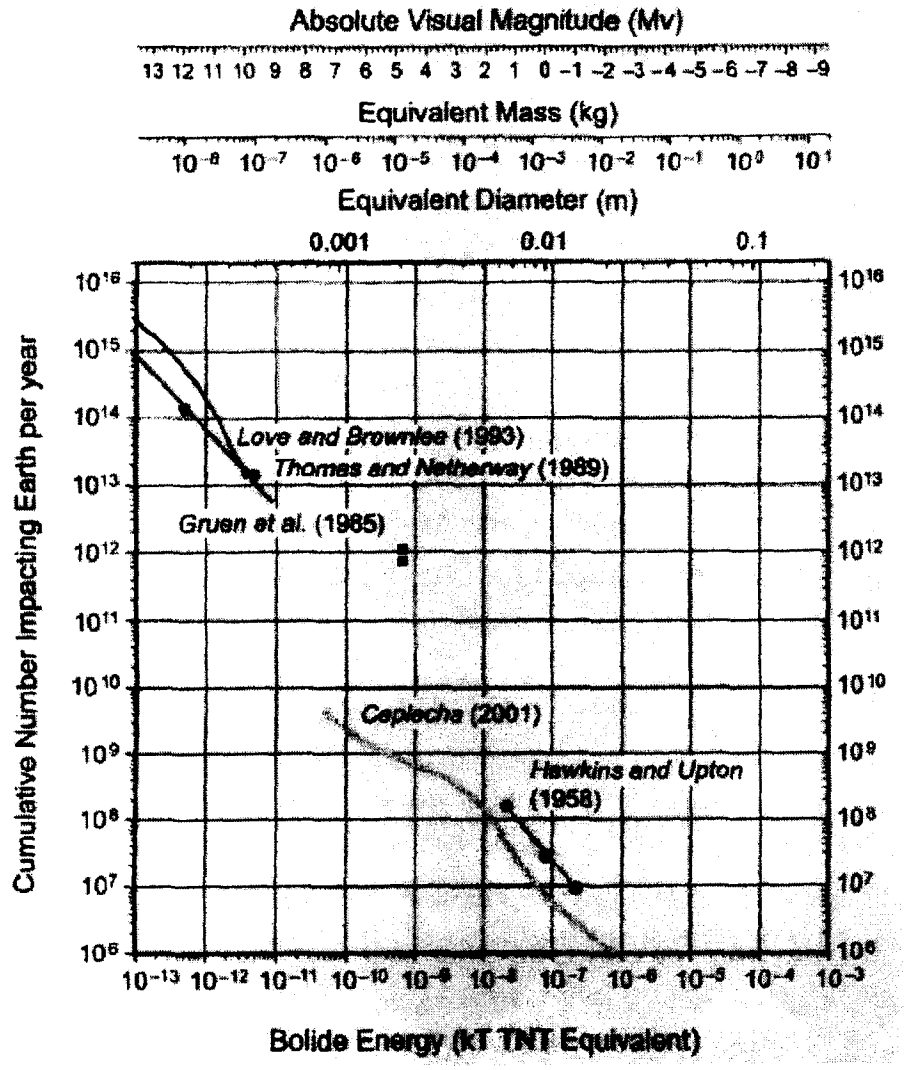


**Figure 5.2: Cumulative annual fluxes for sporadic meteors (Zolensky et al 2006). The current annual flux values for April 27, 2006 (upper point) and May 6, 2006 (lower point) have been added to the plot and are represented by filled squares.**

To compare with scaled radar flux values, the fluxes are scaled to a limiting magnitude of +6.5 using the factor:

$$C = 10^{\left((6.5-lm)\frac{s-1}{2.5}\right)} \qquad (5.1)$$

Here *lm* is the limiting magnitude of the system and *s* is the mass distribution index. For the limiting magnitude in this study, $C = 6.46 \pm 0.97$ and the fluxes

become: $1.46 \pm 0.25$ meteors $km^{-2}hr^{-1}$ and $0.98 \pm 0.21$ meteors $km^{-2}hr^{-1}$ and are now corrected to a limiting magnitude of +6.5 mag. These values are in agreement with the scaled fluxes; however, the nights are not far enough apart to show any significant between night differences as seen in Campbell-Brown and Jones (2006).

From the current results one the most important directions for research to take are to gather a larger sample and improve the statistics so that individual mass and velocity distributions can be obtained for the sporadic sources. With improved characterization of the sporadic sources, corrections to provide the appropriate scaling for comparisons with other systems may be achieved with greater confidence. Calibration of optical and radar together, by observing the same meteors, will greatly improve the understanding of the luminous efficiency, which is probably the greatest source of uncertainty in electro-optical meteor physics.

## Bibliography

Ayers, W.G., McCrosky, R.E., & Shao,C.Y. (1970). Photographic Observations of 10 Artificial Meteors. *Smithsonian Astrophysical Observatory. Special Report #317.*

Becker, D.G., & Friichtenicht, J. F. (1971). Measurement and Interpretation of the Luminous Efficencies of Iron and Copper Simulated Micrometeors. *Astrophysical Journal. 166*, 699-716.

Borovička, J. (1990). The comparison of two methods of determining meteor trajectories from photographs. *Astronomical Institutes of Czechoslovakia, Bulletin. 41*, 391-396.

Bronshten, V.A. (1983). Physics of Meteor Phenomena. In: Hill et al (2005).

Brown, P., Šimek, M., Jones, J., Arlt, R., Hocking, W. K., & Beech, M. (1998). Observations of the 1996 Leonid meteor shower by radar, visual video techniques. *Monthly Notes Royal Astronomical Society. 300*, 244–250.

Brown, P., & Jones, J. (1995). A Determination of Strengths of the Sporadic Radio-Meteor Sources. *Earth, Moon, and Planets. 68*, 1-3. 223-245.

Brown, P., & Rendtel, J. (1996). The Perseid Meteoroid Stream: Characterization of Recent Activity from Visual Observations. *Icarus. 124*, 414-428.

Brown, P., Campbell, M. D., Hawkes, R. L., Theijsmeijer, C., & Jones, J. (2002a). Multi-station electro-optical observations of the 1999 Leonid meteor storm. *Planetary and Space Science. 50*, 45-55.

Brown, P., Campbell, M., Suggs, R., Cooke, W., Theijsmeijer, C., Hawkes, R. L., Jones, J., & Ellis, K. J. (2002b). Video and radar observations of the 2000

Leonids: evidence for a strong flux peak associated with 1932 ejecta?. *Monthly Notices of the Royal Astronomical Society. 335,* 473-479.

Brown, P., Weryk, R. J., Wong, D. K., & Jones, J. (2008). The Canadian Meteor Orbit Radar Meteor Stream Catalogue. *Earth, Moon and Planets. 102.* 209-219.

Campbell, M. D., Brown, P. G., LeBlanc, A. G., Hawkes, R. L., Jones, J., Worden, S. P., & Correll, R. R. (2000). Image –Intensified Video Results from the 1998 Leonid Shower I. Atmospheric Trajectories and Physical Structure. *Meteoritics and Planetary Science. 35,* 1259-1267.

Campbell, M., Theijsmeijer, C., Jones, J., Hawkes, R. L., & Brown, P. (2001). Ground-based observations of the Leonids 1999 – 2000. *Proceedings of the Meteoroids 2001 Conference. 2001*, 197 – 201.

Campbell-Brown, M., & Koschny, D. (2004). Model of the Ablation of Faint Meteors. *Astronomy and Astrophysics.418*, 751-758.

Campbell-Brown, M.D. (2008). High resolution radiant distribution and orbits of sporadic radar meteoroids. *Icarus. 196*, 144-163.

Campbell-Brown, M.D., & Jones, J. (2006). Annual variation of sporadic radar meteor rates. *Monthly Notices of the Royal Astronomical Society. 367*, 709–716.

Campbell-Brown, M., & Brown, P. (2005). The Meteoroid Environment: Shower and Sporadic Meteors. *Proceedings 'Dust in Planetary Systems'. 2005,* 29-30.

Carney, B.W., & Latham, D.W. (1987). The local galactic escape velocity. *Proceedings of the IAU Symposium. 1985*, 39-48.

Ceplecha, Z., Borovička, J., Elford, W.G., Revelle, D.O., Hawkes, R. L., Porubčan, V., & Šimek, M. (1998). Meteor Phenomena and Bodies. *Space Science Reviews. 84*, 327-471.

Ceplecha, Z. (1996). Luminous Efficiency Based on Photographic Observations of the Lost City Fireball and Implications for the Influx of Interplanetary Bodies to Earth. *Astronomy and Astrophysics. 311*, 329-332.

Chau, J.L., Woodman, R.F., & Galindo, F. (2007). Sporadic meteor sources as observed by the Jicamarca high-power large-aperture VHF radar. *Icarus. 188*, 162-174.

Clifton, K.S. (1971). Airborne Meteor Observations at High Latitudes. *NASA Technical Note. NASA TN D-6303*, 1-54.

Clifton, K.S. (1973). Television Studies of Faint Meteors, *Journal of Geophysical Research. 78*, 6511-6521.

Dubietis, A. (2003). Long-term Activity of Meteor Showers from Comet 1P/Halley. *Journal of the International Meteor Organization. 31*, 43-48.

Duffy, A.G., Hawkes, R.L., & Jones, J. (1988). Television observations of the 1984 Orionid shower. *Monthly Notices of the Royal Astronomical Society. 234*, 643-654.

Fyfe, J. D., & Hawkes, R.L. (1986). Residual mass from ablation of meteoroid grains detached during atmospheric flight. *Planetary and Space Science. 34*, 1201-1212.

Greenhow, J.S. (1963). Limitations of Radar Techniques for the Study of Meteors. *Smithsonian Contributions to Astrophysics. 7*, 5-18.

Gural, P. (1997). An Operational Autonomous Meteor Detector. *Journal of the International Meteor Organization. 25*, 136-140.

Hawkes, R., & Jones, J. (1973). An Inexpensive Meteor Observing System. *The Observatory. 93*, 233-235.

Hawkes, R.L., & Jones, J. (1975). Television Observations of Faint Meteors – I: Mass Distribution and Diurnal Rate Variation. *Monthly Notices of the Royal Astronomical Society. 170*, 363-377.

Hawkes, R.L., Jones, J., & Ceplecha, Z. (1984). The populations and orbits of double-station TV meteors. *Astronomical Institutes of Czechoslovakia Bulletin, 35, 1.* 46-64.

Hawkes, R.L., Mason, K.I., Fleming, D.E.B., & Stultz, C.T. (1993). Analysis Procedures for Two Station Television Meteors. *Proceedings of the International Meteor Conference. 1992*, 28-42.

Hawkes, R. L., & Jones, J. (1986). Electro-optical meteor observation techniques and results. *Royal Astronomical Society, Quarterly Journal. 27*, 569-589.

Hayes, D.S., & Latham, D.W. (1975). A Rediscussion of the Atmospheric Extinction and the Absolute Spectral-Energy Distribution of Vega. *Astrophysical Journal. 197*, 593-601.

Hill, K.A., Rogers, L.A., & Hawkes, R.L. (2005). High geocentric velocity meteor ablation. *Astronomy and Astrophysics. 444,* 615-624.

Howell, S.B. (2000). *Handbook of CCD Astronomy*. Cambridge University Press: Cambridge, U.K.

Hughes, D.W. (1987). P/Halley Dust Characteristics: A Comparison Between Orionid and Eta Aquarid Meteor Observations and Those From Fly-by Spacecraft. *Astronomy and Astropysics.187*, 879-888.

Hughes, D.W., & Stephenson, D. G. (1972). The diurnal variation in the massdistribution of sporadic meteors. *Monthly Notices of the Royal Astronomical Society. 155*, 403-413

McBeath, A. (2006). 2006 Meteor Shower Calendar. IMO INFO(2-05) (online) http://www.imo.net/files/data/calendar/cal06.pdf.

Jones, J. (1968). The mass distributions of meteoroids and asteroids. *Canadian Journal of Physics. 46*, 1101-1107.

Jones, J, & Brown, P. (1993). Sporadic meteor radiant distributions: orbital survey results. *Monthly Notices of the Royal Astronomical Society. 265*, 524-532.

Jones, W., & Halliday, I. (2001). Effects of excitation and ionization in meteor trains. *Monthly Notices of the Royal Astronomical Society. 320*, 417-423.

McCord, T. B., Morris, J., Persing, D., Tagliaferri, E., Jacobs, C., Spalding, R., Grady, L., & Schmidt, R. (1995). Detection of a meteoroid entry into the Earth's atmosphere on February 1, 1994. *Journal of Geophysical Research. 100*, 3245–3249.

McCrosky, P.E., & Posen, A. (1968). Special Data Reduction Procedures for Prairie Network Meteor Photographs. *Smithsonian Astrophysical Observatory. Special Report, 273.*

McKinley, D.W.R. (1961). *Meteor Science and Engineering*. McGraw-Hill Book Company, Inc. New York.

Molau, S. (1999). The Meteor Detection Software MetRec. *Proceedings Meteroids 1998. 1999*, 131-134.

Molau, S., & Gural, P. (2005). A Review of Video Meteor Detection and Analysis Software. *Journal of the International Meteor Organization. 33,* 1,15-20.

Opik, E.J. (1955). The masses of meteors In: McKinley, D.W.R (1961)

Pawlowski, J.F, Hebert, T.J, Hawkes, R.L, Matney, M.J., & Stansbery, E.G. (2001). Flux of very faint leonid meteors observed with a 3 m liquid mirror telescope intensified CCD system. *Meteoritics and Planetary Science. 36*, 1467-1477.

Pecinova, D., & Pecina, P. (2007). Radar meteors range distribution model II. Shower flux density and mass distribution index. *The Contributions of Astronomical Observatory Skalnate Pleso. 37, 2.* 107-124.

Rendtel, J. (1997). The η-Aquarid Meteor Shower in 1997. *Journal of International Meteor Organization. 25,* 153-156.

Sarma, T., & Jones, J. (1985). Double-station observations of 454 TV meteors. I – Trajectories. *Astronomical Institutes of Czechoslovakia, Bulletin. 36,* 9-14.

# Appendices

## Appendix A) Detection settings for Meteorscan

Version = 2.800000

SITE GEOMETRY:

Longitude (+West deg) = 110.120000

Latitude (+North deg) = 31.680000

Platform Vel Azimuth (deg): Gnd->0 = 0.000000

CALIBRATION PARAMETERS:

Calibration UT (m/d/y h:m:s) = 4/29/2006 9:25:51

Calibration Center RA (hr min) = 13 48.350000

Calibration Center Dec (deg min) = 27 9.789000

Arcminutes/Pixel (columns) = 2.833333

Arcminutes/Pixel (rows) = 2.833333

Arcminutes/Pixel**2 (Not Used) = 0.000000

Arcminutes/Pixel**2 (Not Used) = 0.000000

Arcminutes/Pixel**3 (Not Used) = 0.000000

Arcminutes/Pixel**3 (Not Used) = 0.000000

Barrel Distortion (Not Used) = 0.000000

Plate Roll wrt Std Coords (+ccw deg) = -75.428047

B-V red star warning limit = 1.200000

MAGNITUDE FIT PARAMETERS:

Magnitude / Log(Intensity) Slope = -28.415378

Magnitude / Log(Intensity) Intercept = 97.867077

THRESHOLD FACTORS:

j1 -> Jitter sigma factor = 10

k1 -> Primary sigma factor x 4 = 7

k2 -> Secondary HNR sigma factor = 4

k3 -> Tertiary SNR sigma factor x 2 = 11

kb -> Binary SNR sigma factor x 2 = 17

Hough autodetect HNR level (dB) = 32.000000

DETECTION PROCESSING PARAMETERS:

Movie loop 1/2 band width (pixels) = 21

Hough refinement 1/2 bw (pixels) = 7

Hough refinement pre-sum (bits) = 1

Hough refinement number of angles = 81

Hough refinement max angle (deg) = 10.000000

Tilt + Hough error tolerance (deg) = 5.000000

Radiant diam. extra tolerance (deg) = 1.500000

Velocity association tolerance (%) = 30.000000

SCAN MODE DEFAULT PARAMETERS:

Mode: 0-5 Tape BIT Live D AVI DV = 4

Algorithm: 0-2: 200, >300MHz, NRT = 2

Dyn Range: 0,4-10,20,30,40,Full = 4

Display: 0,2-history,trk,trk/train = 0

Jitter Rejection: 0-NO 1-YES = 0

Reject Corner Tracks: 0-NO 1-YES = 1

Screen Out Static: 0-NO 1-YES = 0

Pixels per Image Speed Cutoff = 2

Report Period 0,5-10,15,20,30,45,60 = 5

Bell 0,4-Detect,Assoc,Rad,Period,No = 4

Save Format 0,4-No,One,Half,All,Four = 3

PROCESSING REGION PARAMETERS:

Row for the top of proc. window = 0

Row for the bottom of proc. window = 449

Column for the left of proc. window = 10

Column for the right of proc. window = 709

MASKING REGION PARAMETERS:

Row for the top of the mask = 420

Row for the bottom of the mask = 421

Column for the left of the mask = 580

Column for the right of the mask = 587

JITTER REGION PARAMETERS:

Row for the jitter area center = 459

Column for the jitter area center = 25

TRACKING FILTER RESPONSE COEFFICIENTS:

Primary filter, power of two = 5

Secondary filter, power of two = 5

Tertairy filter, power of two = 7

FILE CONTROL PARAMETERS:

TIFF File Compression: 0-No, 1-TBD= 0

Input Parameter Files Directory = C:\Meteor Scan\

Input Digitized Data Directory =

Z:\shannon\ARIZONA\CameraT\apr28-29\apr28-29cameraTtape4\

Output File Directory =

Z:\shannon\ARIZONA\CameraT\apr28-29\apr28-29cameraTtape4\out -

dave\

Report File Directory =

Z:\shannon\ARIZONA\CameraT\apr28-29\apr28-29cameraTtape4\out -

dave\

Single Track/Train File Directory = Meteordata\

Single Track/Train Image Cutout Size = 0

Single Track Image: 0-Raw 1-Enhance = 0

Sequence Format: 1-3 TIFF,AVI,JPEG = 1

# frames in sequence prior to peak = 12

# frames in sequence after the peak = 27

# Appendix B) Full solution data for eta aquariids

| Date-Time | Stations | Alpha | Delta | Lambda-1 | Lambda-2 | Phi-1 | Phi-2 | Height-1 | Height-2 | Velocity-1 | Velocity-2 | Magnitude | Hmax | Mass |
|---|---|---|---|---|---|---|---|---|---|---|---|---|---|---|
| | | +/- | +/- | +/- | +/- | +/- | +/- | +/- | +/- | +/- | +/- | | | +/- |
| 20060427-110522 | SQT | 330.99 | -3.01 | 248.368 | 248.052 | 31.601 | 31.692 | 124.7 | 111.6 | 70 | 66.8 | 0.58 | 113.494 | 1.48E-05 |
| | | 0.06 | 0.2 | 0.0001 | 0.0001 | 0.001 | 0.001 | 0.2 | 0.2 | 8.5 | 4.8 | | | 1.2E-06 |
| 20060427-111042 | SQT | 332.1 | -3.8 | 248.724 | 248.115 | 31.436 | 31.617 | 124.9 | 100.1 | 68 | 64 | -0.6 | 112.5737 | 0.00021 |
| | | 0.8 | 0.2 | 0.002 | 0.002 | 0.002 | 0.002 | 0.4 | 0.3 | 8 | 4.6 | | | 0.00001 |
| 20060506-094005 | TSQ | 337 | -0.4 | 248.798 | 248.376 | 31.762 | 31.799 | 110.6 | 104.4 | 69 | 65.9 | 2.7 | 107.729 | 1.21E-05 |
| | | 1 | 0.5 | 0.003 | 0.0008 | 0.004 | 0.001 | 0.6 | 0.2 | 9.7 | 4.6 | | | 5E-07 |
| 20060506-094911 | ST | 336.1 | -0.44 | 248.677 | 248.016 | 31.4798 | 31.5506 | 126.2 | 114.14 | 68 | 66.7 | 2.2 | 116.824 | 7.48E-06 |
| | | 0.2 | 0.05 | 0.0006 | 0.0005 | 0.0007 | 0.0006 | 0.1 | 0.09 | 8.3 | 5.6 | | | 5.5E-07 |
| 20060506-095134 | TSQ | 337.01 | -0.27 | 248.815 | 248.096 | 31.5309 | 31.6101 | 120.7 | 106.79 | 67 | 65.3 | 0.9 | 110.721 | 5.02E-05 |
| | | 0.2 | 0.04 | 0.0006 | 0.0004 | 0.0007 | 0.0005 | 0.1 | 0.08 | 8 | 4.6 | | | 2.5E-06 |
| 20060506-095411 | SQT | 337.7 | -0.43 | 248.746 | 248.176 | 31.5201 | 31.5842 | 114.8 | 103.84 | 70 | 67.6 | 3.5 | 105.133 | 5.57E-06 |
| | | 0.1 | 0.03 | 0.0003 | 0.0003 | 0.0004 | 0.0003 | 0.06 | 0.05 | 8.5 | 4.7 | | | 3.2E-07 |
| 20060506-102059 | TSQ | 338.5 | -1 | 248.421 | 248.095 | 31.7068 | 31.762 | 117.78 | 108.9 | 70 | 68.9 | 2.79 | 114.529 | 5.06E-06 |
| | | 0.4 | 0.2 | 0.0004 | 0.0005 | 0.0008 | 0.0008 | 0.09 | 0.1 | 8.5 | 4.8 | | | 4E-07 |
| 20060506-102422 | SQT | 336.2 | 0.22 | 248.542 | 248.19 | 31.5463 | 31.6105 | 116.09 | 104.04 | 69 | 64.3 | 2.9 | 112.849 | 5.87E-06 |
| | | 0.3 | 0.09 | 0.0004 | 0.0005 | 0.0006 | 0.0006 | 0.09 | 0.09 | 5.3 | 4.6 | | | 4.3E-07 |
| 20060506-104600 | TSQ | 339.1 | -1.2 | 248.662 | 248.408 | 31.5819 | 31.6393 | 111.1 | 101.749 | 64 | 62.9 | 4 | 103.693 | 1.57E-06 |
| | | 0.5 | 0.2 | 0.0005 | 0.0005 | 0.0008 | 0.0007 | 0.1 | 0.01 | 7.8 | 5.1 | | | 7.6E-08 |
| 20060506-111241 | SQT | 337.3 | -0.2 | 248.601 | 248.306 | 31.44 | 31.5294 | 115.3 | 99.17 | 64 | 63.1 | 2.1 | 106.572 | 1.07E-05 |
| | | 0.9 | 0.1 | 0.002 | 0.0005 | 0.002 | 0.0005 | 0.3 | 0.09 | 9 | 4.5 | | | 8E-07 |
| 20060506-112511 | SQ | 336.9 | 0 | 248.43 | 248.21 | 31.585 | 31.662 | 114.8 | 100.9 | 69 | 67.2 | 2.4 | 108.371 | 6.25E-06 |
| | | 0.7 | 0.2 | 0.0007 | 0.001 | 0.0008 | 0.001 | 0.1 | 0.2 | 7.8 | 5.8 | | | 2E-07 |

## Appendix C) Full solution data for all sporadic meteors

| Date-Time | Stations | Alpha | Delta | Lambda-1 | Lambda-2 | Phi-1 | Phi-2 | Height-1 | Height-2 | Velocity-1 | Velocity-2 | Magnitude | Hmax | Mass |
|---|---|---|---|---|---|---|---|---|---|---|---|---|---|---|
| | | +/- | +/- | +/- | +/- | +/- | +/- | +/- | +/- | +/- | +/- | | | +/- |
| 20060506-085344 | SQ | 282 | 3.9 | 248.53 | 248.47 | 31.597 | 31.634 | 107.48 | 99.41 | 52 | 49.1 | 4.2 | 102.21 | 9.38E-07 |
| | | 1 | 0.4 | 0.001 | 0.001 | 0.0006 | 0.0005 | 0.06 | 0.05 | 5 | 4.3 | | | 8.8E-08 |
| 20060506-090757 | SQT | 221.4 | -32.41 | 248.46 | 248.549 | 31.499 | 31.6691 | 100.32 | 93.61 | 32 | 27 | 4.9 | 98.8794 | 2.11E-06 |
| | | 0.1 | 0.09 | 0.0001 | 0.0003 | 0.0001 | 0.0003 | 0.01 | 0.03 | 3 | 1.9 | | | 1E-07 |
| 20060506-090819 | ST | 302.9 | 20.87 | 248.44 | 248.33 | 31.517 | 31.514 | 107.54 | 97.88 | 62 | 56 | 3 | 99.225 | 1.08E-06 |
| | | 0.5 | 0.09 | 0.0005 | 0.0005 | 0.0002 | 0.0002 | 0.03 | 0.03 | 6.5 | 4.7 | | | 8E-08 |
| 20060506-091247 | SQT | 324.1 | 8.3 | 248.55 | 248.38 | 31.558 | 31.562 | 109.36 | 103.83 | 53 | 52 | 4.4 | 107.001 | 1.4E-06 |
| | | 0.4 | 0.1 | 0.0004 | 0.0004 | 0.0003 | 0.0003 | 0.04 | 0.04 | 5.5 | 3.1 | | | 1E-07 |
| 20060506-091824 | SQT | 243.42 | -18.39 | 248.365 | 248.396 | 31.5221 | 31.6765 | 104.39 | 89.899 | 35 | 31.2 | 3.6 | 97.2206 | 8.02E-06 |
| | | 0.03 | 0.07 | 0.0001 | 0.0001 | 0.0001 | 0.0001 | 0.008 | 0.008 | 4 | 2.3 | | | 4E-07 |
| 20060506-092251 | ST | 261.39 | 14.5 | 248.51 | 248.49 | 31.51 | 31.54 | 98.95 | 87.775 | 28 | 26.1 | 5 | 93.089 | 1.87E-06 |
| | | 0.08 | 0.2 | 0.0003 | 0.0001 | 0.0002 | 0.00005 | 0.01 | 0.004 | 3.5 | 2.3 | | | 1.4E-07 |
| 20060506-092548 | ST | 285 | 68 | 248.33 | 248.31 | 31.724 | 31.686 | 85.7 | 80.528 | 16 | 14.3 | 5.3 | 82.957 | 2.75E-06 |
| | | 1 | 2 | 0.0004 | 0.0003 | 0.00006 | 0.00006 | 0.01 | 0.009 | 1.9 | 1.2 | | | 2.7E-07 |
| 20060506-093804 | SQT | 287.2 | -34.7 | 248.54 | 248.43 | 31.691 | 31.8901 | 107.83 | 99.86 | 58 | 62.3 | 4.1 | 105.092 | 1.86E-06 |
| | | 0.2 | 0.3 | 0.0006 | 0.0001 | 0.0002 | 0.0004 | 0.02 | 0.03 | 5.8 | 4.7 | | | 7.4E-08 |
| 20060506-093850 | SQT | 286.9 | 16.78 | 248.4 | 248.32 | 31.662 | 31.689 | 98.32 | 85.11 | 54 | 50.3 | 4 | 91.452 | 1.69E-06 |
| | | 0.8 | 0.09 | 0.0006 | 0.002 | 0.0001 | 0.0003 | 0.02 | 0.05 | 7.3 | 3.4 | | | 1.8E-07 |
| 20060506-094349 | SQT | 251.2 | 39.5 | 248.55 | 248.56 | 31.701 | 31.695 | 81.823 | 76.613 | 13 | 10.4 | 5.7 | 79.738 | 3.83E-06 |
| | | 0.2 | 0.1 | 0.0001 | 0.00009 | 0.00003 | 0.00003 | 0.003 | 0.003 | 1.5 | 0.8 | | | 2.7E-07 |
| 20060506-094652 | TSQ | 309.5 | 23.54 | 248.458 | 248.345 | 31.5835 | 31.5788 | 110.42 | 99.07 | 58 | 53.7 | 3.9 | 106.522 | 9.73E-07 |
| | | 0.4 | 0.08 | 0.0004 | 0.0005 | 0.0002 | 0.0002 | 0.03 | 0.04 | 6.8 | 3.8 | | | 1.1E-07 |

| Date-Time | Stations | Alpha | Delta | Lambda-1 | Lambda-2 | Phi-1 | Phi-2 | Height-1 | Height-2 | Velocity-1 | Velocity-2 | Magnitude | Hmax | Mass |
|---|---|---|---|---|---|---|---|---|---|---|---|---|---|---|
| | | +/- | +/- | +/- | +/- | +/- | +/- | +/- | +/- | +/- | +/- | | | +/- |
| 20060506-095207 | ST | 239.1 | -20.5 | 248.63 | 248.67 | 31.612 | 31.692 | 102.31 | 95.54 | 34 | 30.6 | 5 | 99.935 | 1.1E-06 |
| | | 0.2 | 0.2 | 0.0002 | 0.0002 | 0.0002 | 0.0002 | 0.01 | 0.01 | 3.3 | 2.6 | | | 5.8E-08 |
| 20060506-095234 | ST | 226.3 | -1.7 | 248.46 | 248.54 | 31.792 | 31.846 | 99.49 | 90.37 | 24 | 23.4 | 5 | 97.0253 | 2.66E-06 |
| | | 0.1 | 0.1 | 0.0001 | 0.0002 | 0.0002 | 0.0002 | 0.01 | 0.02 | 2.8 | 2 | | | 2.2E-07 |
| 20060506-095445 | TSQ | 331.2 | 60.65 | 248.394 | 248.295 | 31.6861 | 31.5715 | 98.34 | 86.53 | 25 | 21.6 | 4.7 | 93.5101 | 5.56E-06 |
| | | 0.3 | 0.04 | 0.0001 | 0.0002 | 0.00008 | 0.0002 | 0.01 | 0.03 | 3 | 1.6 | | | 3.4E-07 |
| 20060506-095639 | ST | 344.9 | 18 | 248.712 | 248.49 | 31.8449 | 31.8045 | 101.46 | 95.58 | 31 | 28.7 | 4.9 | 98.779 | 3.33E-06 |
| | | 0.3 | 0.1 | 0.0002 | 0.0002 | 0.0004 | 0.0004 | 0.04 | 0.05 | 3 | 2.5 | | | 1.5E-07 |
| 20060506-100221 | ST | 308.7 | 8.5 | 248.47 | 248.39 | 31.618 | 31.638 | 86.12 | 79.71 | 12 | 9.86 | 5.5 | 84.1538 | 9.04E-06 |
| | | 0.4 | 0.1 | 0.0004 | 0.0003 | 0.0002 | 0.0002 | 0.02 | 0.02 | 1.4 | 0.92 | | | 3E-07 |
| 20060506-100804 | SQT | 259.8 | -21.9 | 248.563 | 248.574 | 31.5407 | 31.6381 | 91.233 | 83.134 | 37 | 34.5 | 5.5 | 87.8416 | 7.6E-07 |
| | | 0.1 | 0.2 | 0.0003 | 0.0002 | 0.0001 | 0.00009 | 0.007 | 0.005 | 3.5 | 2.8 | | | 5.7E-08 |
| 20060506-101436 | TSQ | 318.3 | 37.74 | 248.43 | 248.3 | 31.622 | 31.576 | 98.16 | 83.92 | 50 | 50.2 | 4 | 92.57 | 2.44E-06 |
| | | 0.3 | 0.08 | 0.0002 | 0.0005 | 0.0001 | 0.0003 | 0.02 | 0.04 | 4.5 | 3.6 | | | 2E-08 |
| 20060506-101453 | SQ | 310 | -20.3 | 248.46 | 248.29 | 31.558 | 31.703 | 108.8 | 98.1 | 67 | 68.7 | 4.7 | 107.333 | 4.48E-07 |
| | | 1 | 0.6 | 0.002 | 0.002 | 0.002 | 0.002 | 0.2 | 0.2 | 7.8 | 5.9 | | | 3E-08 |
| 20060506-101834 | SQT | 276.61 | -28.9 | 248.423 | 248.386 | 31.5947 | 31.8204 | 102.153 | 88.056 | 59 | 57.7 | 3.6 | 93.8879 | 2.29E-06 |
| | | 0.06 | 0.1 | 0.0003 | 0.0004 | 0.00006 | 0.00007 | 0.004 | 0.004 | 7.3 | 4.4 | | | 1.7E-07 |
| 20060506-102934 | TSQ | 247.53 | -22.01 | 248.45 | 248.52 | 31.5077 | 31.6387 | 98.163 | 87.927 | 24 | 23.6 | 4.5 | 93.208 | 6.15E-06 |
| | | 0.04 | 0.06 | 0.0001 | 0.0001 | 0.00009 | 0.00009 | 0.0005 | 0.004 | 2.8 | 1.5 | | | 3.3E-07 |
| 20060506-102959 | SQT | 302.8 | -19.3 | 248.499 | 248.33 | 31.5565 | 31.7569 | 115.7 | 99.46 | 69 | 62.4 | 2.6 | 106.155 | 6.48E-06 |
| | | 0.2 | 0.2 | 0.0006 | 0.0006 | 0.0005 | 0.0005 | 0.04 | 0.04 | 8.3 | 4.3 | | | 5E-07 |
| 20060506-103050 | TSQ | 310 | 8 | 248.674 | 248.516 | 31.706 | 31.7662 | 117 | 99.84 | 58 | 59.5 | 2.7 | 107.782 | 4.86E-06 |
| | | 3 | 1 | 0.009 | 0.001 | 0.005 | 0.0008 | 0.6 | 0.08 | 10 | 4.7 | | | 6E-07 |

| Date-Time | Stations | Alpha | Delta | Lambda-1 | Lambda-2 | Phi-1 | Phi-2 | Height-1 | Height-2 | Velocity-1 | Velocity-2 | Magnitude | Hmax | Mass |
|---|---|---|---|---|---|---|---|---|---|---|---|---|---|---|
| | | +/- | +/- | +/- | +/- | +/- | +/- | +/- | +/- | +/- | +/- | | | +/- |
| 20060506-103206 | ST | 284.34 | 49.5 | 248.687 | 248.638 | 31.6567 | 31.5655 | 113.018 | 82.665 | 40 | 34.4 | 1.5 | 95.867 | 5.41E-05 |
| | | 0.04 | 0.1 | 0.0005 | 0.0001 | 0.0001 | 0.00002 | 0.006 | 0.002 | 4.8 | 3 | | | 3.9E-06 |
| 20060506-103215 | SQ | 275.49 | -4.6 | 248.44 | 248.42 | 31.572 | 31.67 | 103.08 | 88.324 | 55 | 54.4 | 5.4 | 97.578 | 4.88E-07 |
| | | 0.08 | 0.1 | 0.0002 | 0.0002 | 0.0002 | 0.0002 | 0.01 | 0.009 | 6.5 | 4.7 | | | 2E-08 |
| 20060506-103248 | ST | 261.1 | -16.1 | 248.31 | 248.35 | 31.637 | 31.77 | 98.718 | 85.274 | 37 | 37 | 4.9 | 91.87 | 1.54E-06 |
| | | 0.05 | 0.1 | 0.0002 | 0.0003 | 0.00001 | 0.0002 | 0.005 | 0.009 | 4.5 | 3.1 | | | 1.1E-07 |
| 20060506-103608 | SQ | 311.3 | 4.4 | 248.58 | 248.48 | 31.571 | 31.617 | 101.39 | 90.78 | 65 | 66.3 | 0.5 | 94.35 | 1.12E-06 |
| | | 0.4 | 0.1 | 0.0005 | 0.0005 | 0.0003 | 0.0003 | 0.04 | 0.04 | 6 | 5.6 | | | 1.7E-07 |
| 20060506-103946 | SQT | 238.06 | -12.44 | 248.504 | 248.626 | 31.6104 | 31.7246 | 101.703 | 89.575 | 30 | 26.2 | 4 | 96.1771 | 7.18E-06 |
| | | 0.06 | 0.07 | 0.0001 | 0.0001 | 0.0002 | 0.0001 | 0.009 | 0.008 | 3.5 | 1.8 | | | 2E-07 |
| 20060506-104159 | TSQ | 233.04 | -15.65 | 248.444 | 248.566 | 31.6313 | 31.7308 | 100.261 | 91.432 | 28 | 26.6 | 0.5 | 96.2985 | 7.07E-06 |
| | | 0.08 | 0.07 | 0.0001 | 0.0001 | 0.0001 | 0.0001 | 0.009 | 0.009 | 2.8 | 2 | | | 7E-07 |
| 20060506-104352 | SQT | 281.8 | -3.9 | 248.46 | 248.44 | 31.523 | 31.611 | 98.88 | 85.02 | 64 | 57 | 4.7 | 96.01 | 5.14E-07 |
| | | 0.1 | 0.2 | 0.0002 | 0.0003 | 0.0002 | 0.0003 | 0.01 | 0.02 | 7.5 | 3.9 | | | 5E-08 |
| 20060506-104715 | SQT | 273.61 | 41.39 | 248.49 | 248.49 | 31.693 | 31.676 | 98.606 | 86.421 | 37 | 31.5 | 0.5 | 90.323 | 3.3E-06 |
| | | 0.09 | 0.08 | 0.0001 | 0.0001 | 0.000007 | 0.000007 | 0.001 | 0.0007 | 2.8 | 2.2 | | | 4.1E-07 |
| 20060506-105408 | SQ | 340.4 | 3.8 | 248.49 | 248.28 | 31.733 | 31.767 | 114.82 | 105.69 | 65 | 62.3 | 4 | 111.277 | 1.28E-06 |
| | | 0.5 | 0.2 | 0.0004 | 0.0004 | 0.0008 | 0.0008 | 0.09 | 0.09 | 5.8 | 5 | | | 9E-08 |
| 20060506-105841 | SQ | 297 | 13.1 | 248.3 | 248.2 | 31.73 | 31.76 | 111.3 | 101.6 | 69 | 64.9 | 3.83 | 106.15 | 8.07E-07 |
| | | 1 | 0.4 | 0.001 | 0.001 | 0.0005 | 0.0005 | 0.06 | 0.06 | 8.3 | 5.3 | | | 1.2E-07 |
| 20060506-105856 | ST | 330 | -2 | 248.673 | 248.508 | 31.608 | 31.668 | 113.8 | 104.4 | 71 | 66 | 3.3 | 108.377 | 1.21E-06 |
| | | 3 | 1 | 0.004 | 0.001 | 0.004 | 0.002 | 0.6 | 0.2 | 7 | 5.6 | | | 1.5E-07 |
| 20060506-110127 | SQ | 292.1 | -12.31 | 248.32 | 248.3 | 31.658 | 31.713 | 108.14 | 101.72 | 63 | 59.1 | 3.8 | 106.87 | 1.11E-06 |
| | | 0.9 | 0.1 | 0.0001 | 0.0001 | 0.0008 | 0.0009 | 0.05 | 0.05 | 5.3 | 5.1 | | | 1.5E-07 |

| Date-Time | Stations | Alpha | Delta | Lambda-1 | Lambda-2 | Phi-1 | Phi-2 | Height-1 | Height-2 | Velocity-1 | Velocity-2 | Magnitude | Hmax | Mass |
|---|---|---|---|---|---|---|---|---|---|---|---|---|---|---|
| | | +/- | +/- | +/- | +/- | +/- | +/- | +/- | +/- | +/- | +/- | | | +/- |
| 20060506-110304 | SQT | 248.28 | -36.07 | 248.398 | 248.52 | 31.6367 | 31.8659 | 106.912 | 98.446 | 41 | 39 | 3.6 | 102.951 | 5.98E-06 |
| | | 0.04 | 0.06 | 0.0002 | 0.0002 | 0.00009 | 0.0001 | 0.006 | 0.007 | 4 | 2.4 | | | 3E-07 |
| 20060506-110524 | SQ | 296.2 | -11.2 | 248.51 | 248.47 | 31.606 | 31.694 | 108.69 | 98.33 | 62 | 60.8 | 5 | 104.4 | 2.69E-07 |
| | | 0.2 | 0.3 | 0.0004 | 0.0004 | 0.0004 | 0.0004 | 0.02 | 0.03 | 5.8 | 5.2 | | | 2E-08 |
| 20060506-110645 | SQT | 308.9 | -10.9 | 248.523 | 248.408 | 31.5645 | 31.6929 | 113.37 | 98.47 | 75 | 67.5 | 3.1 | 106.374 | 2.4E-06 |
| | | 0.5 | 0.4 | 0.0001 | 0.0001 | 0.0001 | 0.0001 | 0.08 | 0.08 | 6 | 4.8 | | | 2.2E-07 |
| 20060506-110813 | ST | 322 | 1.8 | 248.32 | 248.21 | 31.436 | 31.49 | 113.9 | 103.2 | 72 | 70.3 | 3.1 | 107.78 | 1.47E-06 |
| | | 1 | 0.3 | 0.001 | 0.001 | 0.0009 | 0.0009 | 0.2 | 0.1 | 8 | 6.1 | | | 2.4E-07 |
| 20060506-110826 | TSQ | 303 | -8 | 248.4 | 248.32 | 31.556 | 31.668 | 99.1 | 85 | 69 | 68.3 | 3.11 | 92.254 | 2.94E-06 |
| | | 1 | 0.8 | 0.002 | 0.004 | 0.001 | 0.003 | 0.1 | 0.2 | 6 | 4.8 | | | 2E-07 |
| 20060506-110856 | ST | 327.7 | -20.3 | 248.73 | 248.5 | 31.65 | 31.837 | 103.16 | 91.3 | 69 | 65 | 3.6 | 98.3349 | 4.27E-06 |
| | | 0.3 | 0.2 | 0.0006 | 0.0006 | 0.0008 | 0.0008 | 0.07 | 0.07 | 8.5 | 5.5 | | | 3.3E-07 |
| 20060506-112238 | SQ | 305.1 | 15.5 | 248.52 | 248.48 | 31.636 | 31.659 | 110.5 | 100.92 | 65 | 56.3 | 4.3 | 109.1 | 4.96E-07 |
| | | 0.5 | 0.2 | 0.0005 | 0.0004 | 0.0002 | 0.0002 | 0.03 | 0.03 | 6.3 | 4.8 | | | 7.3E-08 |
| 20060506-085235 | ST | 213.3 | 4.6 | 248.35 | 248.39 | 31.658 | 31.685 | 83.023 | 77.097 | 14 | 12.8 | 5.3 | 80.37 | 4.77E-06 |
| | | 0.2 | 0.1 | 0.00008 | 0.00007 | 0.0001 | 0.00001 | 0.001 | 0.009 | 1.4 | 1.1 | | | 4.4E-07 |
| 20060506-085746 | ST | 245.22 | -17.19 | 248.69 | 248.69 | 31.668 | 31.8 | 95.904 | 83.038 | 22 | 18.3 | 5 | 89.8135 | 5.87E-06 |
| | | 0.04 | 0.07 | 0.0001 | 0.0001 | 0.0001 | 0.0001 | 0.007 | 0.007 | 2.8 | 1.6 | | | 3.6E-07 |
| 20060506-085910 | ST | 265.4 | 49.8 | 248.25 | 248.23 | 31.731 | 31.695 | 102.32 | 91.354 | 33 | 30.7 | 4.6 | 95.795 | 1.81E-06 |
| | | 0.4 | 0.2 | 0.0004 | 0.0003 | 0.00008 | 0.00006 | 0.01 | 0.001 | 3 | 2.6 | | | 1.4E-07 |
| 20060506-110006 | TSQ | 258.07 | -1.3 | 248.45 | 248.49 | 31.595 | 31.652 | 96.885 | 87.125 | 20 | 21 | 5.5 | 90.556 | 1.99E-06 |
| | | 0.09 | 0.1 | 0.0001 | 0.00001 | 0.0002 | 0.0001 | 0.009 | 0.006 | 2.1 | 1.6 | | | 1E-07 |
| 20060506-102020 | ST | 224.7 | 3.652 | 248.65 | 248.77 | 31.498 | 31.546 | 101.1 | 90.43 | 24 | 23.6 | 2.5 | 96.0828 | 6.89E-06 |
| | | 0.2 | 0.01 | 0.0002 | 0.0002 | 0.0002 | 0.0002 | 0.02 | 0.02 | 3 | 2 | | | 4E-07 |

| Date-Time | Stations | Alpha | Delta | Lambda-1 | Lambda-2 | Phi-1 | Phi-2 | Height-1 | Height-2 | Velocity-1 | Velocity-2 | Magnitude | Hmax | Mass |
|---|---|---|---|---|---|---|---|---|---|---|---|---|---|---|
| | | +/- | +/- | +/- | +/- | +/- | +/- | +/- | +/- | +/- | +/- | | | +/- |
| 20060506-101106 | TSQ | 239.1 | 38.4 | 248.62 | 248.64 | 31.679 | 31.671 | 79.492 | 74.063 | 19 | 12.8 | 4.38 | 78.246 | 3.73E-06 |
| | | 0.3 | 0.4 | 0.0001 | 0.0003 | 0.00008 | 0.0002 | 0.006 | 0.001 | 2.3 | 1 | | | 2E-07 |
| 20060506-101124 | SQT | 286.8 | -13.8 | 248.35 | 248.28 | 31.638 | 31.762 | 101.08 | 87.91 | 62 | 57.4 | 4.1 | 96.092 | 1.13E-06 |
| | | 0.4 | 0.4 | 0.0007 | 0.001 | 0.0004 | 0.0009 | 0.03 | 0.05 | 11 | 4.8 | | | 1E-07 |
| 20060427-104247 | SQT | 198.3 | 69.54 | 248.4 | 248.449 | 31.7612 | 31.6596 | 92.61 | 82.91 | 18 | 15.4 | 5.2 | 87.5969 | 4.51E-06 |
| | | 0.3 | 0.06 | 0.0001 | 0.00009 | 0.00009 | 0.00007 | 0.02 | 0.01 | 2.3 | 1.1 | | | 2.6E-07 |
| 20060427-112815 | SQT | 306.7 | 9.48 | 248.474 | 248.37 | 31.5815 | 31.6316 | 104.47 | 89.68 | 64 | 62.7 | 3.7 | 98.4062 | 1.19E-06 |
| | | 0.4 | 0.08 | 0.0007 | 0.0006 | 0.0003 | 0.0003 | 0.04 | 0.04 | 7.8 | 4.4 | | | 3.9E-08 |
| 20060427-112606 | SQ | 296.6 | 56.01 | 248.39 | 248.37 | 31.542 | 31.504 | 103 | 94.39 | 38 | 31.2 | 4.6 | 99.574 | 1.4E-06 |
| | | 0.4 | 0.3 | 0.0003 | 0.0004 | 0.00008 | 0.0001 | 0.009 | 0.01 | 4.5 | 2.7 | | | 1.6E-07 |
| 20060427-112351 | SQT | 310.23 | 10.96 | 248.641 | 248.499 | 31.6386 | 31.6935 | 95.72 | 77.014 | 23 | 18.5 | 3.2 | 88.0634 | 0.000008 |
| | | 0.08 | 0.02 | 0.0002 | 0.0001 | 0.00008 | 0.00008 | 0.01 | 0.001 | 2.8 | 1.4 | | | 5E-07 |
| 20060427-112239 | ST | 270.75 | -33.4 | 248.539 | 248.555 | 31.4857 | 31.7052 | 114.183 | 102.688 | 60 | 55.8 | 3.4 | 109.882 | 3.86E-06 |
| | | 0.06 | 0.2 | 0.0004 | 0.0005 | 0.00002 | 0.00002 | 0.003 | 0.003 | 7 | 4.8 | | | 3.3E-07 |
| 20060427-112124 | SQT | 298.3 | 8.8 | 248.44 | 248.36 | 31.691 | 31.745 | 106.69 | 91.87 | 74 | 64.8 | 3.6 | 102.25 | 9.54E-07 |
| | | 0.8 | 0.3 | 0.002 | 0.0009 | 0.0007 | 0.0005 | 0.07 | 0.05 | 9 | 4.6 | | | 1E-07 |
| 20060427-112110 | SQT | 307.5 | -12 | 248.73 | 248.57 | 31.485 | 31.634 | 106.3 | 90.12 | 68 | 65.2 | 2.8 | 99.521 | 4.99E-06 |
| | | 0.6 | 0.5 | 0.002 | 0.0006 | 0.002 | 0.0006 | 0.2 | 0.05 | 8.3 | 4.8 | | | 4E-07 |
| 20060427-082040 | ST | 328.2 | 54.92 | 248.733 | 248.586 | 31.8091 | 31.6452 | 104.15 | 95.43 | 39 | 36.5 | 3.7 | 100.581 | 6.13E-06 |
| | | 0.2 | 0.06 | 0.0002 | 0.0002 | 0.0001 | 0.0001 | 0.02 | 0.02 | 4.5 | 3.2 | | | 3E-07 |
| 20060427-111555 | ST | 336.2 | 7.7 | 248.428 | 248.221 | 31.788 | 31.8116 | 111.942 | 101.94 | 54 | 49.3 | 3.7 | 108.007 | 2.46E-06 |
| | | 0.5 | 0.3 | 0.0005 | 0.0004 | 0.0008 | 0.0007 | 0.01 | 0.09 | 6.8 | 4 | | | 2.5E-07 |
| 20060427-111206 | ST | 258 | 38.96 | 248.6 | 248.6 | 31.82 | 31.81 | 94.43 | 83.18 | 20 | 17.9 | 5.4 | 87.666 | 2.86E-06 |
| | | 0.1 | 0.03 | 0.0001 | 0.0001 | 0.00002 | 0.00002 | 0.002 | 0.002 | 2.2 | 1.5 | | | 1.9E-07 |

| Date-Time | Stations | Alpha | Delta | Lambda-1 | Lambda-2 | Phi-1 | Phi-2 | Height-1 | Height-2 | Velocity-1 | Velocity-2 | Magnitude | Hmax | Mass |
|---|---|---|---|---|---|---|---|---|---|---|---|---|---|---|
| | | +/- | +/- | +/- | +/- | +/- | +/- | +/- | +/- | +/- | +/- | | | +/- |
| 20060427-110834 | SQT | 222.74 | 0.8 | 248.35 | 248.535 | 31.5081 | 31.5797 | 101.263 | 87.456 | 28 | 22.5 | 3.4 | 94.8106 | 1.72E-05 |
| | | 0.05 | 0.04 | 0.00007 | 0.00007 | 0.00009 | 0.00001 | 0.008 | 0.008 | 3.3 | 1.7 | | | 5E-07 |
| 20060427-110654 | SQT | 277.29 | -30.7 | 248.34 | 248.32 | 31.654 | 31.839 | 115.13 | 104.37 | 67 | 62.5 | 3.7 | 111.775 | 1.56E-06 |
| | | 0.01 | 0.2 | 0.0005 | 0.0006 | 0.0001 | 0.0001 | 0.005 | 0.006 | 8 | 4.8 | | | 1.5E-07 |
| 20060427-110643 | SQT | 301.8 | 43.2 | 248.58 | 248.53 | 31.592 | 31.567 | 105.13 | 95.275 | 42 | 40.6 | 4.2 | 101.76 | 1.38E-06 |
| | | 0.2 | 0.2 | 0.0002 | 0.0002 | 0.00009 | 0.00009 | 0.009 | 0.009 | 5 | 2.8 | | | 1.5E-07 |
| 20060427-110559 | SQT | 325.1 | 43.27 | 248.42 | 248.32 | 31.663 | 31.611 | 104.93 | 93.64 | 44 | 37.8 | 4 | 99.2343 | 2.17E-06 |
| | | 0.3 | 0.06 | 0.0002 | 0.0002 | 0.0001 | 0.0001 | 0.02 | 0.02 | 5.3 | 2.6 | | | 1.8E-07 |
| 20060427-110453 | SQ | 280.1 | -15.9 | 248.3 | 248.27 | 31.592 | 31.695 | 114.06 | 103.45 | 65 | 62.6 | 3.9 | 107.64 | 7.72E-07 |
| | | 0.3 | 0.4 | 0.0007 | 0.0006 | 0.0003 | 0.0003 | 0.02 | 0.02 | 8 | 5.2 | | | 1E-07 |
| 20060427-110038 | SQT | 277.73 | 38.65 | 248.44 | 248.42 | 31.739 | 31.721 | 105.09 | 89.182 | 46 | 33.8 | 3.9 | 98.0506 | 2.44E-06 |
| | | 0.09 | 0.08 | 0.0002 | 0.0002 | 0.00002 | 0.00002 | 0.002 | 0.002 | 5.5 | 2.5 | | | 1.7E-07 |
| 20060427-105947 | ST | 236.64 | -14.22 | 248.61 | 248.7 | 31.747 | 31.851 | 101.92 | 91.47 | 26 | 28.3 | 0.5 | 99.5891 | 8.49E-06 |
| | | 0.08 | 0.09 | 0.0002 | 0.0001 | 0.0002 | 0.0002 | 0.01 | 0.01 | 3.3 | 2.4 | | | 9E-07 |
| 20060427-105916 | SQT | 222.3 | -5.26 | 248.51 | 248.69 | 31.524 | 31.617 | 88.467 | 75.529 | 24 | 15.4 | 5 | 85.502 | 3.59E-06 |
| | | 0.03 | 0.04 | 0.00005 | 0.00005 | 0.00007 | 0.0001 | 0.005 | 0.007 | 2.3 | 1.1 | | | 1.5E-07 |
| 20060427-105835 | SQT | 312.99 | 39.47 | 248.591 | 248.413 | 31.8109 | 31.7395 | 110.32 | 84.79 | 44 | 38.4 | 2 | 97.0828 | 2.09E-05 |
| | | 0.08 | 0.02 | 0.0002 | 0.0001 | 0.00009 | 0.00007 | 0.01 | 0.009 | 5.5 | 2.7 | | | 5E-07 |
| 20060427-105531 | QST | 309.74 | 46.53 | 248.52 | 248.42 | 31.673 | 31.602 | 107.16 | 88.935 | 41 | 38.1 | 3 | 100.708 | 6.37E-06 |
| | | 0.08 | 0.03 | 0.0001 | 0.0001 | 0.00005 | 0.00005 | 0.008 | 0.007 | 5 | 2.8 | | | 5.1E-07 |
| 20060427-113212 | SQT | 226.06 | 2.23 | 248.273 | 248.597 | 31.5917 | 31.699 | 106.405 | 83.864 | 29 | 21.9 | 1.8 | 92.9989 | 8.82E-05 |
| | | 0.02 | 0.03 | 0.00007 | 0.00006 | 0.0001 | 0.00001 | 0.008 | 0.006 | 3.5 | 1.6 | | | 4.1E-06 |
| 20060427-105416 | SQ | 314.7 | 3.1 | 248.55 | 248.39 | 31.623 | 31.682 | 116.05 | 103.02 | 64 | 61 | 3.75 | 110.6 | 2.17E-06 |
| | | 0.6 | 0.2 | 0.0001 | 0.0008 | 0.0007 | 0.0005 | 0.09 | 0.07 | 7.8 | 5.3 | | | 1.8E-07 |

| Date-Time | Stations | Alpha | Delta | Lambda-1 | Lambda-2 | Phi-1 | Phi-2 | Height-1 | Height-2 | Velocity-1 | Velocity-2 | Magnitude | Hmax | Mass |
|---|---|---|---|---|---|---|---|---|---|---|---|---|---|---|
| | | +/- | +/- | +/- | +/- | +/- | +/- | +/- | +/- | +/- | +/- | | | +/- |
| 20060427-105332 | SQT | 320.6 | 42.69 | 248.34 | 248.214 | 31.6889 | 31.6226 | 106.59 | 90.95 | 48 | 42.8 | 3.1 | 100.853 | 5.75E-06 |
| | | 0.5 | 0.07 | 0.0002 | 0.0007 | 0.0001 | 0.0004 | 0.02 | 0.07 | 5.8 | 2.9 | | | 4.3E-07 |
| 20060427-104921 | ST | 330 | 2.63 | 248.62 | 248.3 | 31.51 | 31.567 | 104.44 | 90.83 | 64 | 62.1 | 4 | 101.171 | 2.88E-06 |
| | | 0.2 | 0.06 | 0.0004 | 0.0004 | 0.0004 | 0.0004 | 0.06 | 0.06 | 7.3 | 5.4 | | | 2.3E-07 |
| 20060427-104556 | SQ | 314.1 | 16.9 | 248.48 | 248.39 | 31.585 | 31.593 | 109.48 | 101.66 | 58 | 51.7 | 4.4 | 104.61 | 6.12E-07 |
| | | 0.5 | 0.1 | 0.0005 | 0.0004 | 0.0003 | 0.0002 | 0.04 | 0.03 | 7 | 4.4 | | | 6E-08 |
| 20060427-104347 | ST | 295.9 | 1.3 | 248.73 | 248.56 | 31.479 | 31.593 | 120.5 | 98.26 | 63 | 64.5 | 2.5 | 108.481 | 9.54E-06 |
| | | 0.8 | 0.3 | 0.003 | 0.002 | 0.001 | 0.0009 | 0.1 | 0.08 | 7.8 | 5.5 | | | 9E-07 |
| 20060427-111805 | ST | 2.09 | 18.47 | 248.616 | 248.143 | 31.8069 | 31.6962 | 107.83 | 99.08 | 39 | 39 | 2.4 | 104.249 | 6.74E-06 |
| | | 0.09 | 0.06 | 0.00007 | 0.0001 | 0.0003 | 0.0004 | 0.03 | 0.04 | 4 | 3.1 | | | 3.6E-07 |
| 20060427-104155 | SQT | 230.74 | -15.8 | 248.31 | 248.37 | 31.653 | 31.724 | 100.92 | 94.336 | 28 | 29 | 5 | 99.424 | 1.93E-06 |
| | | 0.01 | 0.1 | 0.0001 | 0.00009 | 0.0002 | 0.0001 | 0.01 | 0.007 | 3.5 | 2 | | | 1.1E-07 |
| 20060427-103721 | SQ | 282.94 | 25.91 | 248.53 | 248.47 | 31.604 | 31.615 | 99.992 | 83.056 | 39 | 31.8 | 5.7 | 96.575 | 8.41E-07 |
| | | 0.08 | 0.06 | 0.0002 | 0.0002 | 0.00005 | 0.00005 | 0.004 | 0.004 | 4.8 | 2.7 | | | 7E-08 |
| 20060427-103715 | SQT | 229.8 | -17.9 | 248.361 | 248.443 | 31.6516 | 31.7447 | 102.84 | 94.86 | 34 | 31.2 | 4.9 | 98.7942 | 1.41E-06 |
| | | 0.1 | 0.1 | 0.0002 | 0.0001 | 0.0002 | 0.0002 | 0.02 | 0.01 | 3.3 | 2.2 | | | 4.7E-08 |
| 20060427-103547 | SQ | 286.4 | -37.6 | 248.34 | 248.24 | 31.585 | 31.823 | 116.49 | 107.64 | 69 | 64 | 3.8 | 111.54 | 1.58E-06 |
| | | 0.2 | 0.2 | 0.0007 | 0.0007 | 0.0002 | 0.0002 | 0.02 | 0.02 | 8.3 | 5.5 | | | 1.1E-07 |
| 20060427-103336 | ST | 315.1 | 25.8 | 248.46 | 248.34 | 31.428 | 31.415 | 109.12 | 97.89 | 59 | 51.7 | 3.4 | 104.579 | 1.89E-06 |
| | | 0.6 | 0.1 | 0.0007 | 0.0007 | 0.0004 | 0.0004 | 0.05 | 0.05 | 7.3 | 4.4 | | | 2.2E-07 |
| 20060427-103239 | SQT | 218.4 | 2.03 | 248.46 | 248.55 | 31.511 | 31.553 | 97.95 | 89.649 | 23 | 20.1 | 3.3 | 93.9345 | 3.89E-06 |
| | | 0.1 | 0.09 | 0.0001 | 0.00009 | 0.0001 | 0.0002 | 0.01 | 0.001 | 2.8 | 1.4 | | | 3E-07 |
| 20060427-101025 | ST | 229.54 | -15.85 | 248.53 | 248.61 | 31.409 | 31.515 | 104.54 | 94.24 | 34 | 30.2 | 3.8 | 100.993 | 6.12E-06 |
| | | 0.08 | 0.08 | 0.0001 | 0.0001 | 0.0002 | 0.0001 | 0.01 | 0.01 | 4 | 2.6 | | | 5.4E-07 |

| Date-Time | Stations | Alpha | Delta | Lambda-1 | Lambda-2 | Phi-1 | Phi-2 | Height-1 | Height-2 | Velocity-1 | Velocity-2 | Magnitude | Hmax | Mass |
|---|---|---|---|---|---|---|---|---|---|---|---|---|---|---|
| | | +/- | +/- | +/- | +/- | +/- | +/- | +/- | +/- | +/- | +/- | | | +/- |
| 20060427-101020 | SQT | 277.2 | -32.5 | 248.521 | 248.42 | 31.6247 | 31.8738 | 113.03 | 100.55 | 68 | 57.9 | 3.3 | 108.413 | 3.95E-06 |
| | | 0.1 | 0.2 | 0.0006 | 0.0006 | 0.0001 | 0.0001 | 0.01 | 0.01 | 8.5 | 4.6 | | | 3.7E-07 |
| 20060427-100942 | SQT | 237.2 | -16.9 | 248.391 | 248.432 | 31.4928 | 31.5752 | 103.68 | 95.72 | 33 | 34.8 | 4.7 | 100.644 | 1.56E-06 |
| | | 0.2 | 0.2 | 0.0002 | 0.0002 | 0.0003 | 0.0002 | 0.02 | 0.01 | 4 | 2.8 | | | 1.6E-07 |
| 20060427-100705 | SQ | 255.18 | -1.9 | 248.44 | 248.46 | 31.634 | 31.696 | 98.674 | 88.273 | 22 | 16.4 | 5.3 | 93.2178 | 2.44E-06 |
| | | 0.08 | 0.1 | 0.00001 | 0.00008 | 0.0002 | 0.0001 | 0.008 | 0.007 | 2.5 | 1.4 | | | 1.4E-07 |
| 20060427-100556 | SQ | 293 | -5 | 248.54 | 248.4 | 31.715 | 31.811 | 100.1 | 87.5 | 61 | 63.2 | 4.2 | 98.214 | 8.49E-07 |
| | | 3 | 2 | 0.004 | 0.006 | 0.003 | 0.005 | 0.2 | 0.3 | 7.3 | 5.4 | | | 8.6E-08 |
| 20060427-100241 | SQT | 269.01 | 32.7 | 248.39 | 248.37 | 31.606 | 31.603 | 102.64 | 93.985 | 33 | 31.1 | 4.7 | 97.266 | 1.42E-06 |
| | | 0.2 | 0.2 | 0.0002 | 0.0003 | 0.00003 | 0.00003 | 0.006 | 0.006 | 4.3 | 2.2 | | | 1.8E-07 |
| 20060427-100140 | SQT | 264.3 | 16.9 | 248.34 | 248.32 | 31.564 | 31.589 | 108.51 | 97.942 | 56 | 46.8 | 2.84 | 102.31 | 2.08E-06 |
| | | 0.2 | 0.08 | 0.0002 | 0.0002 | 0.00004 | 0.00004 | 0.006 | 0.005 | 6.8 | 3.4 | | | 2E-07 |
| 20060427-095209 | SQT | 296 | -9 | 248.72 | 248.56 | 31.478 | 31.577 | 106.4 | 94.5 | 53 | 58.8 | 3.1 | 101.04 | 3.62E-06 |
| | | 3 | 1 | 0.009 | 0.003 | 0.005 | 0.002 | 0.5 | 0.2 | 6.5 | 4.4 | | | 3.7E-07 |
| 20060427-094826 | SQT | 246.18 | -0.56 | 248.57 | 248.57 | 31.601 | 31.673 | 95.593 | 82.669 | 42 | 35.6 | 4.5 | 88.655 | 1.62E-06 |
| | | 0.07 | 0.06 | 0.00009 | 0.00009 | 0.0001 | 0.00009 | 0.006 | 0.006 | 4.3 | 2.6 | | | 1.7E-07 |
| 20060427-094623 | ST | 230.62 | -8.4 | 248.18 | 248.24 | 31.614 | 31.698 | 101.28 | 90.14 | 30 | 24 | 4.4 | 97.0938 | 4.31E-06 |
| | | 0.06 | 0.1 | 0.00009 | 0.00008 | 0.0002 | 0.0002 | 0.01 | 0.01 | 3.5 | 2 | | | 3E-07 |
| 20060427-094622 | SQT | 290.1 | 21.56 | 248.52 | 248.43 | 31.722 | 31.73 | 107.02 | 94.86 | 45 | 43.6 | 4 | 104.42 | 1.96E-06 |
| | | 0.3 | 0.05 | 0.0003 | 0.0004 | 0.00009 | 0.0001 | 0.01 | 0.02 | 5.5 | 3.1 | | | 2.6E-07 |
| 20060427-094519 | ST | 238.09 | -19.48 | 248.611 | 248.667 | 31.5 | 31.6856 | 108.26 | 91.62 | 33 | 29.4 | 2.4 | 98.7032 | 2.62E-05 |
| | | 0.06 | 0.08 | 0.0002 | 0.0002 | 0.0002 | 0.0002 | 0.01 | 0.01 | 4 | 2.5 | | | 5.9E-07 |
| 20060427-094034 | ST | 251.4 | 33.8 | 248.64 | 248.63 | 31.744 | 31.741 | 103.45 | 93.99 | 40 | 30.7 | 5.3 | 100.38 | 6.83E-07 |
| | | 0.3 | 0.2 | 0.0002 | 0.0003 | 0.00009 | 0.00008 | 0.01 | 0.01 | 4.8 | 2.7 | | | 2.9E-08 |

| Date-Time | Stations | Alpha | Delta | Lambda-1 | Lambda-2 | Phi-1 | Phi-2 | Height-1 | Height-2 | Velocity-1 | Velocity-2 | Magnitude | Hmax | Mass |
|---|---|---|---|---|---|---|---|---|---|---|---|---|---|---|
| | | +/- | +/- | +/- | +/- | +/- | +/- | +/- | +/- | +/- | +/- | | | +/- |
| 20060427-093823 | SQT | 321.7 | 47.39 | 248.556 | 248.395 | 31.7285 | 31.6153 | 98.59 | 85.23 | 44 | 40.9 | 4.2 | 90.3985 | 2.39E-06 |
| | | 0.1 | 0.03 | 0.0001 | 0.0001 | 0.00008 | 0.00008 | 0.01 | 0.01 | 5.3 | 3 | | | 1.9E-07 |
| 20060427-093557 | SQT | 318.2 | 44.33 | 248.689 | 248.459 | 31.8422 | 31.706 | 107.66 | 88.84 | 44 | 39.3 | 2.2 | 101.604 | 2.08E-05 |
| | | 0.1 | 0.03 | 0.0002 | 0.0002 | 0.0001 | 0.00001 | 0.02 | 0.01 | 4.8 | 2.8 | | | 1.3E-06 |
| 20060427-093143 | ST | 250.3 | 25 | 248.53 | 248.52 | 31.529 | 31.538 | 103.97 | 95.562 | 46 | 35.3 | 4.8 | 99.209 | 7.02E-07 |
| | | 0.2 | 0.3 | 0.0002 | 0.0002 | 0.0002 | 0.0001 | 0.01 | 0.001 | 5.5 | 3 | | | 1E-07 |
| 20060427-093007 | SQT | 239.79 | -14.67 | 248.521 | 248.548 | 31.4898 | 31.6478 | 102.575 | 85.608 | 30 | 23.9 | 3.6 | 93.6366 | 1.37E-05 |
| | | 0.03 | 0.05 | 0.00009 | 0.00008 | 0.0001 | 0.0001 | 0.007 | 0.007 | 3.8 | 1.9 | | | 6E-07 |
| 20060427-092136 | SQ | 278 | -17.4 | 248.43 | 248.34 | 31.584 | 31.68 | 108.54 | 100.2 | 55 | 50.9 | 2.1 | 106.85 | 1.04E-06 |
| | | 1 | 0.9 | 0.002 | 0.002 | 0.0007 | 0.0009 | 0.08 | 0.1 | 6.8 | 4.3 | | | 1.1E-07 |
| 20060427-091824 | ST | 281.5 | 42.97 | 248.23 | 248.18 | 31.679 | 31.65 | 107.21 | 97.47 | 41 | 36.6 | 3 | 103.22 | 3.85E-06 |
| | | 0.4 | 0.09 | 0.0004 | 0.0003 | 0.00009 | 0.00007 | 0.02 | 0.01 | 5 | 3.1 | | | 4E-07 |
| 20060427-091730 | ST | 228.34 | -14.9 | 248.32 | 248.35 | 31.571 | 31.666 | 101.75 | 91.76 | 26 | 28.1 | 4.8 | 96.936 | 2.78E-06 |
| | | 0.08 | 0.2 | 0.0001 | 0.00009 | 0.0003 | 0.0002 | 0.02 | 0.01 | 3.3 | 2.4 | | | 2.1E-07 |
| 20060427-091610 | SQT | 217.7 | 14.4 | 248.493 | 248.557 | 31.6489 | 31.6833 | 87.66 | 74.11 | 24 | 24 | 5.7 | 80.0893 | 2.02E-06 |
| | | 0.1 | 0.06 | 0.0001 | 0.0001 | 0.0001 | 0.0001 | 0.01 | 0.01 | 3 | 1.8 | | | 8E-08 |
| 20060427-091441 | SQT | 226.9 | 10.3 | 248.37 | 248.408 | 31.7407 | 31.7787 | 100.71 | 89.73 | 31 | 25 | 4.8 | 96.9094 | 2.01E-06 |
| | | 0.2 | 0.1 | 0.0002 | 0.0002 | 0.0002 | 0.0002 | 0.01 | 0.02 | 3.8 | 1.8 | | | 1.8E-07 |
| 20060427-091336 | SQT | 279 | -2 | 248.58 | 248.38 | 31.62 | 31.738 | 132 | 111.1 | 62 | 65.9 | 2.95 | 119.66 | 2.95E-06 |
| | | 6 | 4 | 0.03 | 0.009 | 0.02 | 0.006 | 1 | 0.5 | 7.5 | 4.7 | | | 2.7E-07 |
| 20060427-091326 | ST | 296 | 7.5 | 248.672 | 248.447 | 31.75 | 31.796 | 115.9 | 100.8 | 59 | 53.2 | 2.1 | 106.027 | 8.82E-06 |
| | | 2 | 0.8 | 0.006 | 0.003 | 0.003 | 0.002 | 0.4 | 0.2 | 5.5 | 4.7 | | | 8E-07 |
| 20060427-091114 | ST | 255 | 17.2 | 248.25 | 248.22 | 31.528 | 31.548 | 104.18 | 94.1 | 50 | 41.8 | 4.1 | 98.713 | 1.35E-06 |
| | | 0.5 | 0.2 | 0.0005 | 0.0004 | 0.0002 | 0.0002 | 0.03 | 0.02 | 6.3 | 3.4 | | | 1.7E-07 |

| Date-Time | Stations | Alpha | Delta | Lambda-1 | Lambda-2 | Phi-1 | Phi-2 | Height-1 | Height-2 | Velocity-1 | Velocity-2 | Magnitude | Hmax | Mass |
|---|---|---|---|---|---|---|---|---|---|---|---|---|---|---|
| | | +/- | +/- | +/- | +/- | +/- | +/- | +/- | +/- | +/- | +/- | | | +/- |
| 20060427-091018 | SQT | 247 | 45.2 | 248.46 | 248.46 | 31.547 | 31.534 | 83.158 | 77.592 | 17 | 16.7 | 4.2 | 82.877 | 5.86E-06 |
| | | 0.2 | 0.3 | 0.0001 | 0.0002 | 0.00006 | 0.00009 | 0.006 | 0.009 | 2.1 | 0.9 | | | 6.1E-07 |
| 20060427-091016 | SQ | 287.3 | 37.8 | 248.47 | 248.37 | 31.735 | 31.702 | 110.48 | 97.25 | 51 | 45.3 | 4.5 | 105.29 | 1.42E-06 |
| | | 0.3 | 0.07 | 0.0003 | 0.0003 | 0.00001 | 0.00009 | 0.02 | 0.02 | 6.3 | 3.9 | | | 4.3E-08 |
| 20060427-090837 | ST | 250.7 | -13.6 | 248.4 | 248.38 | 31.438 | 31.508 | 93.6 | 85.82 | 35 | 27.6 | 4.7 | 92.343 | 1.74E-06 |
| | | 0.4 | 0.4 | 0.0004 | 0.0005 | 0.0004 | 0.0005 | 0.03 | 0.04 | 4.3 | 2.4 | | | 1.6E-07 |
| 20060427-090730 | ST | 233.2 | -5.4 | 248.468 | 248.489 | 31.7707 | 31.8536 | 92.3 | 80.07 | 33 | 29.1 | 3.8 | 89.1962 | 3.42E-06 |
| | | 0.1 | 0.2 | 0.0001 | 0.0002 | 0.0003 | 0.0004 | 0.02 | 0.02 | 4 | 2.5 | | | 3E-07 |
| 20060427-090624 | SQT | 306.7 | -7.7 | 248.632 | 248.096 | 31.646 | 31.8077 | 123.01 | 107.986 | 72 | 72.4 | 0.9 | 112.402 | 4.22E-05 |
| | | 0.3 | 0.1 | 0.001 | 0.001 | 0.001 | 0.0009 | 0.1 | 0.01 | 8.5 | 5.1 | | | 3.1E-06 |
| 20060427-085634 | SQT | 283.3 | 17.58 | 248.45 | 248.32 | 31.72 | 31.737 | 100.42 | 86.33 | 57 | 50.7 | 4.4 | 96.004 | 1.3E-06 |
| | | 0.3 | 0.06 | 0.0005 | 0.0004 | 0.0002 | 0.0001 | 0.02 | 0.02 | 7 | 3.5 | | | 8E-08 |
| 20060427-085549 | SQT | 293.5 | 4.3 | 248.389 | 248.183 | 31.6454 | 31.6938 | 115.01 | 102.83 | 59 | 57.8 | 3.8 | 109.777 | 2.2E-06 |
| | | 0.7 | 0.2 | 0.001 | 0.001 | 0.0007 | 0.0007 | 0.08 | 0.08 | 7.5 | 4.1 | | | 2.2E-07 |
| 20060427-085523 | SQ | 248.7 | 23.4 | 248.5 | 248.5 | 31.68 | 31.7 | 104.1 | 96.07 | 44 | 40.4 | 5 | 100.1 | 4.5E-07 |
| | | 0.2 | 0.1 | 0.0001 | 0.0001 | 0.00008 | 0.00007 | 0.008 | 0.008 | 5.3 | 3.5 | | | 7E-08 |
| 20060427-085509 | SQ | 233.97 | -23.91 | 248.58 | 248.59 | 31.552 | 31.728 | 91.747 | 78.268 | 28 | 17.3 | 6.4 | 84.8774 | 1.04E-06 |
| | | 0.03 | 0.05 | 0.00001 | 0.00007 | 0.0001 | 0.00009 | 0.009 | 0.006 | 3.5 | 1.4 | | | 3E-08 |
| 20060427-085429 | ST | 229.87 | -5.8 | 248.337 | 248.362 | 31.5728 | 31.6743 | 91.4 | 76.53 | 36 | 19.5 | 3 | 87.2241 | 8.4E-06 |
| | | 0.08 | 0.1 | 0.0001 | 0.0001 | 0.0003 | 0.0002 | 0.02 | 0.01 | 4.5 | 1.8 | | | 7E-07 |
| 20060427-085252 | ST | 212.34 | 9.75 | 248.48 | 248.53 | 31.812 | 31.85 | 98.222 | 87.003 | 25 | 19.5 | 4.3 | 92.3159 | 5.99E-06 |
| | | 0.07 | 0.08 | 0.00006 | 0.00006 | 0.0001 | 0.0001 | 0.008 | 0.007 | 3 | 1.7 | | | 3E-07 |
| 20060427-085137 | SQT | 323.1 | 47.24 | 248.516 | 248.336 | 31.7438 | 31.6059 | 106.42 | 95.61 | 43 | 38.7 | 3.2 | 102.146 | 6.4E-06 |
| | | 0.1 | 0.04 | 0.0002 | 0.0002 | 0.0001 | 0.0001 | 0.02 | 0.02 | 4.8 | 2.8 | | | 2E-07 |

| Date-Time | Stations | Alpha | Delta | Lambda-1 | Lambda-2 | Phi-1 | Phi-2 | Height-1 | Height-2 | Velocity-1 | Velocity-2 | Magnitude | Hmax | Mass |
|---|---|---|---|---|---|---|---|---|---|---|---|---|---|---|
| | | +/- | +/- | +/- | +/- | +/- | +/- | +/- | +/- | +/- | +/- | | | +/- |
| 20060427-084813 | SQ | 250.1 | 9 | 248.48 | 248.44 | 31.747 | 31.798 | 96.91 | 82.8 | 45 | 35.1 | 5.5 | 92.685 | 4.65E-07 |
| | | 2 | 1 | 0.001 | 0.003 | 0.001 | 0.003 | 0.09 | 0.2 | 4.8 | 3 | | | 3E-08 |
| 20060427-084717 | SQ | 282.6 | 2.8 | 248.49 | 248.36 | 31.656 | 31.706 | 110.21 | 99.3 | 56 | 49.5 | 4.7 | 107.009 | 8.7E-07 |
| | | 0.1 | 0.4 | 0.001 | 0.001 | 0.0009 | 0.0009 | 0.01 | 0.09 | 7 | 3.7 | | | 1E-07 |
| 20060427-084643 | ST | 257.4 | 22.96 | 248.4 | 248.35 | 31.462 | 31.476 | 100.07 | 86.54 | 24 | 23.4 | 4.3 | 93.4362 | 6.78E-06 |
| | | 0.2 | 0.09 | 0.0002 | 0.0002 | 0.00001 | 0.00009 | 0.01 | 0.01 | 3 | 2.1 | | | 5.5E-07 |
| 20060427-084608 | QST | 235.468 | -20.8 | 248.616 | 248.616 | 31.4984 | 31.5873 | 97.001 | 89.29 | 25 | 19.1 | 5.3 | 91.8324 | 1.7E-06 |
| | | 0.01 | 0.2 | 0.0002 | 0.0001 | 0.0003 | 0.0002 | 0.02 | 0.01 | 2.2 | 0.93 | | | 1.4E-07 |
| 20060427-084157 | SQT | 294.4 | -3.3 | 248.72 | 248.43 | 31.589 | 31.6768 | 111.5 | 98.86 | 66 | 64.9 | 3.2 | 103.971 | 4.18E-06 |
| | | 0.7 | 0.2 | 0.002 | 0.001 | 0.001 | 0.0007 | 0.2 | 0.08 | 7.8 | 4.6 | | | 3E-07 |
| 20060427-084133 | SQT | 288.7 | 12.17 | 248.53 | 248.37 | 31.65 | 31.671 | 101.96 | 89.8 | 59 | 56.6 | 4.3 | 97.6279 | 1.3E-06 |
| | | 0.3 | 0.07 | 0.0005 | 0.0005 | 0.0002 | 0.0002 | 0.04 | 0.03 | 7 | 4 | | | 1.4E-07 |
| 20060427-084016 | ST | 263.6 | 25.8 | 248.6 | 248.57 | 31.49 | 31.493 | 101.59 | 94.01 | 33 | 31.9 | 4.5 | 97.536 | 1.7E-06 |
| | | 0.3 | 0.2 | 0.0002 | 0.0002 | 0.00008 | 0.00008 | 0.01 | 0.01 | 4 | 2.8 | | | 1.9E-07 |
| 20060427-084012 | ST | 280.7 | 32 | 248.45 | 248.33 | 31.772 | 31.749 | 104.64 | 91.5 | 44 | 39.3 | 4 | 101.85 | 2.03E-06 |
| | | 0.4 | 2 | 0.0005 | 0.0005 | 0.0002 | 0.0002 | 0.03 | 0.03 | 5.3 | 3.1 | | | 2.2E-07 |
| 20060427-083509 | ST | 267.2 | 38.1 | 248.6 | 248.56 | 31.568 | 31.554 | 101.57 | 94.54 | 32 | 30.4 | 4.7 | 97.75 | 1.02E-06 |
| | | 0.4 | 0.3 | 0.0003 | 0.0003 | 0.00001 | 0.00009 | 0.02 | 0.02 | 3.8 | 2.6 | | | 1.5E-07 |
| 20060427-083445 | SQ | 204.98 | -6.17 | 248.37 | 248.43 | 31.585 | 31.643 | 95.676 | 87.14 | 23 | 16.6 | 5.3 | 89.514 | 2.48E-06 |
| | | 0.06 | 0.07 | 0.00005 | 0.00005 | 0.00009 | 0.00001 | 0.006 | 0.006 | 2.8 | 1.4 | | | 8.2E-08 |
| 20060427-083057 | SQT | 242.25 | -14.4 | 248.496 | 248.47 | 31.5368 | 31.629 | 95.57 | 85.64 | 21 | 18.4 | 5.3 | 92.6722 | 3.82E-06 |
| | | 0.09 | 0.1 | 0.0001 | 0.0001 | 0.0002 | 0.0002 | 0.01 | 0.01 | 2.8 | 1.4 | | | 2.5E-07 |
| 20060427-082919 | SQT | 211.63 | -10.99 | 248.445 | 248.499 | 31.631 | 31.7224 | 95.494 | 84.585 | 22 | 18.1 | 4.7 | 92.0181 | 8.84E-06 |
| | | 0.05 | 0.08 | 0.00006 | 0.00006 | 0.0001 | 0.0001 | 0.008 | 0.006 | 2.8 | 1.3 | | | 3E-07 |

| Date-Time | Stations | Alpha | Delta | Lambda-1 | Lambda-2 | Phi-1 | Phi-2 | Height-1 | Height-2 | Velocity-1 | Velocity-2 | Magnitude | Hmax | Mass |
|---|---|---|---|---|---|---|---|---|---|---|---|---|---|---|
| | | +/- | +/- | +/- | +/- | +/- | +/- | +/- | +/- | +/- | +/- | | | +/- |
| 20060427-082456 | SQ | 293.4 | 6 | 248.493 | 248.253 | 31.5494 | 31.5821 | 112.9 | 101.68 | 59 | 59.1 | 4 | 109.247 | 1.8E-06 |
| | | 0.4 | 0.1 | 0.0008 | 0.00009 | 0.0004 | 0.0005 | 0.06 | 0.07 | 7.3 | 5 | | | 7E-08 |
| 20060427-082127 | ST | 259.3 | 66.01 | 248.6 | 248.58 | 31.528 | 31.482 | 99.72 | 93.02 | 25 | 22.5 | 4.5 | 94.9837 | 2.58E-06 |
| | | 0.7 | 0.3 | 0.0003 | 0.0003 | 0.0001 | 0.00001 | 0.02 | 0.02 | 3 | 2 | | | 2.7E-07 |
| 20060427-081427 | SQT | 207.3 | 57.6 | 248.601 | 248.628 | 31.6484 | 31.594 | 88.868 | 77.134 | 19 | 11.5 | 4 | 81.3392 | 1.01E-05 |
| | | 0.1 | 0.1 | 0.0001 | 0.00001 | 0.00001 | 0.00009 | 0.001 | 0.009 | 2.3 | 0.89 | | | 6E-07 |
| 20060427-080326 | SQT | 231.14 | -44.7 | 248.424 | 248.395 | 31.4406 | 31.7281 | 100.13 | 92.33 | 38 | 37.2 | 5 | 97.5197 | 2.52E-06 |
| | | 0.07 | 0.1 | 0.0002 | 0.0002 | 0.0002 | 0.0002 | 0.02 | 0.02 | 4 | 2.6 | | | 1.7E-07 |
| 20060427-075810 | ST | 305.7 | 46.14 | 248.524 | 248.356 | 31.8607 | 31.7429 | 106.91 | 96.19 | 42 | 39.4 | 3.1 | 99.1221 | 4.9E-06 |
| | | 0.2 | 0.09 | 0.0003 | 0.0003 | 0.0002 | 0.0002 | 0.03 | 0.03 | 5 | 3.3 | | | 4E-07 |
| 20060427-072846 | ST | 227.17 | 43.01 | 248.67 | 248.66 | 31.759 | 31.729 | 98.703 | 82.821 | 24 | 18.6 | 2.7 | 90.5011 | 5.78E-06 |
| | | 0.07 | 0.05 | 0.00007 | 0.00007 | 0.00007 | 0.00006 | 0.007 | 0.007 | 3 | 1.6 | | | 4.9E-07 |
| 20060427-072632 | SQT | 233.2 | -18.4 | 248.465 | 248.417 | 31.5716 | 31.6823 | 104.85 | 94.7 | 42 | 34 | 3.1 | 96.5649 | 3.66E-06 |
| | | 0.2 | 0.2 | 0.0003 | 0.0002 | 0.0004 | 0.0004 | 0.03 | 0.03 | 3.5 | 2.5 | | | 2.3E-07 |
| 20060427-071908 | ST | 232.9 | -9.3 | 248.64 | 248.57 | 31.67 | 31.753 | 99.76 | 89.42 | 29 | 28 | 5.1 | 95.655 | 1.58E-06 |
| | | 0.2 | 0.3 | 0.0001 | 0.0002 | 0.0004 | 0.0005 | 0.02 | 0.03 | 3.3 | 2.5 | | | 1.2E-07 |
| 20060427-071237 | ST | 242 | 2.4 | 248.68 | 248.63 | 31.556 | 31.592 | 102.24 | 94.63 | 24 | 28.7 | 5 | 98.756 | 1.85E-06 |
| | | 1 | 0.5 | 0.0009 | 0.0008 | 0.0008 | 0.0007 | 0.01 | 0.08 | 3 | 2.5 | | | 2E-07 |
| 20060427-070744 | ST | 251.8 | 33.91 | 248.592 | 248.49 | 31.5297 | 31.5058 | 97.21 | 82.4 | 30 | 32.1 | 5 | 89.4847 | 2.15E-06 |
| | | 0.2 | 0.08 | 0.0002 | 0.0002 | 0.0001 | 0.0001 | 0.02 | 0.02 | 3.8 | 2.9 | | | 1.7E-07 |
| 20060427-070359 | ST | 214.6 | 26.5 | 248.63 | 248.63 | 31.737 | 31.747 | 99.21 | 86.95 | 32 | 21.5 | 2.6 | 91.6957 | 3.55E-06 |
| | | 0.3 | 0.2 | 0.0003 | 0.0002 | 0.0002 | 0.0002 | 0.02 | 0.02 | 4 | 1.8 | | | 3.7E-07 |
| 20060427-065955 | SQT | 232.4 | -19.3 | 248.625 | 248.491 | 31.4526 | 31.6749 | 102.85 | 83.69 | 36 | 34.7 | 2.5 | 94.3993 | 1.62E-05 |
| | | 0.1 | 0.1 | 0.0003 | 0.0003 | 0.0005 | 0.0004 | 0.04 | 0.03 | 4 | 2.5 | | | 5E-07 |

| Date-Time | Stations | Alpha | Delta | Lambda-1 | Lambda-2 | Phi-1 | Phi-2 | Height-1 | Height-2 | Velocity-1 | Velocity-2 | Magnitude | Hmax | Mass |
|---|---|---|---|---|---|---|---|---|---|---|---|---|---|---|
| | | +/- | +/- | +/- | +/- | +/- | +/- | +/- | +/- | +/- | +/- | | | +/- |
| 20060427-065540 | SQT | 275.7 | 35.94 | 248.455 | 248.262 | 31.6943 | 31.6186 | 100.52 | 86.55 | 29 | 24.8 | 4 | 97.036 | 3.14E-06 |
| | | 0.1 | 0.05 | 0.0001 | 0.0002 | 0.0001 | 0.0001 | 0.02 | 0.02 | 3.5 | 1.8 | | | 1.5E-07 |
| 20060427-065439 | SQT | 235.1 | -19.6 | 248.371 | 248.285 | 31.7344 | 31.856 | 101.24 | 91.33 | 37 | 34.7 | 4 | 97.6667 | 2.6E-06 |
| | | 0.5 | 0.5 | 0.0005 | 0.0007 | 0.0007 | 0.001 | 0.06 | 0.09 | 4.5 | 2.5 | | | 2.5E-07 |
| 20060427-065335 | SQT | 220.51 | -13.41 | 248.592 | 248.544 | 31.4861 | 31.6169 | 89.11 | 74.573 | 38 | 14.3 | 2.4 | 86.9791 | 5.35E-06 |
| | | 0.05 | 0.07 | 0.00001 | 0.00007 | 0.0002 | 0.0001 | 0.01 | 0.008 | 4.8 | 1.1 | | | 2E-07 |
| 20060427-065127 | SQ | 265.1 | 30.4 | 248.5 | 248.4 | 31.64 | 31.618 | 106.59 | 98.27 | 35 | 33.3 | 5 | 102.947 | 1.25E-06 |
| | | 0.5 | 0.2 | 0.0003 | 0.0002 | 0.0003 | 0.0002 | 0.05 | 0.04 | 4.3 | 2.9 | | | 1E-07 |
| 20060427-064653 | SQT | 225.1 | -20.5 | 248.417 | 248.338 | 31.5856 | 31.7396 | 102.98 | 90.12 | 27 | 26.2 | 4.5 | 95.9329 | 4.31E-06 |
| | | 0.2 | 0.3 | 0.0003 | 0.0004 | 0.0006 | 0.0006 | 0.04 | 0.04 | 3.3 | 1.9 | | | 2.9E-07 |
| 20060427-064356 | SQ | 216.7 | -7.7 | 248.5 | 248.48 | 31.687 | 31.763 | 100.92 | 90.67 | 25 | 21.9 | 5.5 | 97.546 | 1.91E-06 |
| | | 0.1 | 0.2 | 0.0001 | 0.0001 | 0.0003 | 0.0003 | 0.02 | 0.02 | 3.3 | 1.8 | | | 9.2E-08 |
| 20060427-062414 | ST | 212 | -12.4 | 248.344 | 248.311 | 31.5139 | 31.6049 | 99.16 | 88.62 | 22 | 19.3 | 4 | 95.0944 | 0.000006 |
| | | 0.6 | 0.5 | 0.0006 | 0.0008 | 0.0006 | 0.0001 | 0.05 | 0.07 | 2.8 | 1.7 | | | 5E-07 |
| 20060427-055422 | ST | 193.26 | -20.6 | 248.699 | 248.695 | 31.7356 | 31.8795 | 99.83 | 87.36 | 23 | 20.7 | 0.5 | 90.8408 | 9.28E-06 |
| | | 0.07 | 0.2 | 0.0001 | 0.0001 | 0.0003 | 0.0003 | 0.02 | 0.02 | 2.8 | 1.8 | | | 9E-07 |
| 20060427-054815 | ST | 228.2 | 30.25 | 248.65 | 248.61 | 31.616 | 31.611 | 82.863 | 75.587 | 17 | 9.35 | 5.8 | 79.1556 | 2.41E-06 |
| | | 0.2 | 0.08 | 0.00001 | 0.00008 | 0.00008 | 0.00007 | 0.001 | 0.008 | 2.1 | 0.83 | | | 8E-08 |
| 20060427-110158 | ST | 278.37 | 20.94 | 248.34 | 248.3 | 31.51 | 31.541 | 98.657 | 79.5 | 36 | 27.6 | 3.1 | 92.243 | 6.64E-06 |
| | | 0.07 | 0.05 | 0.0002 | 0.0002 | 0.00004 | 0.00003 | 0.003 | 0.002 | 4.3 | 2.4 | | | 5.8E-07 |
| 20060427-110046 | ST | 300.1 | -4.7 | 248.468 | 248.348 | 31.33 | 31.4295 | 113.1 | 98.3 | 75 | 66.6 | 2.2 | 107.088 | 4.5E-06 |
| | | 1 | 0.3 | 0.002 | 0.002 | 0.0009 | 0.0008 | 0.1 | 0.1 | 9 | 5.6 | | | 4.7E-07 |
| 20060427-094932 | ST | 217.64 | -15.7 | 248.646 | 248.761 | 31.5905 | 31.7107 | 103.47 | 92.22 | 28 | 25.7 | 3.6 | 100.534 | 8.24E-06 |
| | | 0.09 | 0.1 | 0.0002 | 0.0001 | 0.0003 | 0.0002 | 0.02 | 0.02 | 3.5 | 2.2 | | | 5.9E-07 |